What can we infer about the atmospheric composition within the South Coast Air Basin from remote sensing?

Thesis by

Jacob K. Hedelius

In Partial Fulfillment of the Requirements for the

degree of

Doctor of Philosophy

CALIFORNIA INSTITUTE OF TECHNOLOGY

Pasadena, California

2017

Defended May 4, 2017

2017

Jacob K. Hedelius
ORCID: 0000-0003-2025-7519

ACKNOWLEDGEMENTS

I would first like to thank my advisor, Paul Wennberg, for all of his support these past 5 years. It has been an extraordinary experience to learn from a world renowned scientist and to be mentored on how to distill key results from complex projects. Thanks for giving me flexibility and advice in pursuing interesting projects. I would also like to thank the rest of my thesis committee, John Seinfeld, Jack Beauchamp, and Mitchio Okumura, for their support and advice. I appreciate their time and commitment into helping me become a better scientist.

The entire Wennberg group has been supportive, from helping me find parts in the lab to getting out of Linde+Robinson for social events. In particular, Debra Wunch invested much time into helping me succeed and grow as a scientist, from scripting to writing and presenting results. It was great to work with Camille Viatte 'in the field' and learn from her experience. Coleen Roehl has been a tremendous support at helping with all things TCCON related. Kat Saad and Matt Kiel have explained minute details of their projects to help me with mine. Harrison Parker was great to keep up enthusiasm for campaigns with many days of travel.

It has been engaging to work with collaborators off campus. At JPL Geoff Toon, Annmarie Eldering, Greg Osterman, and Kristal Verhulst have been very supportive. Sha Feng and Thomas Lauvaux at Penn State ran models for me and helped me interpret the results. I have enjoyed working and conversing with Manvendra Dubey at LANL, Steven Wofsy at Harvard, and Jia Chen at TUM along with their students and postdocs. It has been a privilege to work with Akihiko Kuze-san and his team from JAXA. I have had many fruitful discussions with the KIT team and TCCON partners all over the world. It has been a nice experience to work with a global community of scientists.

In addition to academic support, the Linde+Robinson staff have been invaluable. Nora Oshima and Kathy Young have helped with all things administrative from overseas shipments to finding office space for guests. It has been my pleasure to work with them and give tours of our beautiful building.

Many others from Caltech and the area have been great friends. It's been fun carpooling, conversing, going on adventures, and grabbing food with the Caltech LDSSA. Peter Hung, Claus Spenninger, and the Caltech Science Olympiad club have been good for laughs and volunteer opportunities. Carson Hansen, Travis

Schlappi and my Perseids meteor shower camping friends have engaged me in many interesting conversations.

I have had many other supportive influences in my life all the way from elementary school through college. If I were to name them all the list would be very long. However, I would like to especially thank Professors David Dearden, Jeffrey Macedone, and Steven Goates at BYU for encouraging me to apply to graduate school and advising me on research, being a better mentor, and coursework.

Finally I would like to thank my ever loving family. My grandparents and extended family have given encouragement. My siblings (and siblings-in-law) Mark & Alyssa, Kirk & Cassandra, Bryce, Breanna, and Marissa & Greg have maintained interest in my work despite much of it being technical. My brothers have even read some of it! Above all my parents, Eric and Merilyn, have been supportive of my work and education my entire life. I couldn't have done it without you.

ABSTRACT

To observe a change in a gas (e.g., CO_2) flux from an area, the change must exceed the error of the flux estimate. Changing bias could be misinterpreted as a change in flux, and should be avoided. Errors can arise in column CO_2 (X_{CO_2}) retrievals, in mis-interpreting X_{CO_2} variations, or in the models to estimate fluxes. My thesis work has focused on recognizing and quantifying these errors and biases.

The most widely-used ground-based observations of X_{CO_2} are from the Total Carbon Column Observing Network (TCCON), which uses observations from similar spectrometers at high ($0.02\,\text{cm}^{-1}$) resolution. Within the past 5 years there has been increased use of portable, lower resolution ($0.5\,\text{cm}^{-1}$) spectrometers for focused, short-term campaigns. This thesis discusses sources of errors and biases in retrievals from these lower resolution spectrometers.

Previous error estimates for the TCCON were made by propagating various perturbations through the retrieval. These uncertainty estimates were about $0.2\,\%$ for CO_2 and $0.4\,\%$ for CH_4. A pair of portable $0.5\,\text{cm}^{-1}$ resolution spectrometers were used to empirically diagnose the magnitude of bias among TCCON sites. Median estimates were about $0.1\,\%$.

Column measurements have increased in popularity within the last 15 years because of their reduced sensitivity to the dry mole fractions (DMF) of gases near the surface. However, in the presence of a sharp gradient between the atmospheric mixed layer (ML) and free troposphere rapid changes in terrain may cause the ML height above ground level and X_{CO_2} to vary significantly over a small area. This explains ~20–36\,% of the difference in X_{CO_2} between 2 sites (Caltech and JPL) within $10\,\text{km}$ of each other in the South Coast Air Basin (SoCAB).

Dynamical models may have biases (e.g., in wind speed) compared to true atmospheric behavior. This may cause biases in flux estimates. An estimate of the SoCAB CO_2 flux using readily available model data is higher than those reported by bottom-up methods, perhaps due to a high wind speed bias. The flux is also sensitive to sub-sampling, which highlights the need to filter out biased data and the benefits additional observations could provide.

Carbon dioxide is not the only radiative forcer—aerosols are the largest source of uncertainty on the global radiative forcing budget, and additional measurements may better constrain their impacts. Estimate of changes in aerosol optical depth

(AOD) can be made using portable spectrometers. While these estimates are not highly accurate, they are a value-added product and may increase the understanding of atmospheric behavior.

PUBLISHED CONTENT

Chapter 2 is published in:

Hedelius, J. K., Viatte, C., Wunch, D., Roehl, C., Toon, G. C., Chen, J., Jones, T., Wofsy, S. C., Franklin, J. E., Parker, H., Dubey, M. K. and Wennberg, P. O.: Assessment of errors and biases in retrievals of X_{CO_2}, X_{CH_4}, X_{CO}, and X_{N_2O} from a 0.5 cm^{-1} resolution solar viewing spectrometer, Atmos. Meas. Tech., 9, 3527–3546, doi:10.5194/amt-9-3527-2016, 2016. J.K.H. led this study and participated in design, conception, data acquisition, data analysis, software development, figure creation, writing, and revising of this manuscript.

Chapter 3 is published in:

Hedelius, J. K., Parker, H., Wunch, D., Roehl, C., Viatte, C., Newman, S., Toon, G. C., Poldolske, J. R., Hillyard, P. W., Iraci, L. T., Dubey, M. K. and Wennberg, P. O.: Intercomparability of X_{CO_2} and X_{CH_4} from the United States TCCON sites, Atmos. Meas. Tech., 10, 1481-1493, doi:10.5194/amt-10-1481-2017, 2017. J.K.H. led this study and participated in design, conception, data acquisition, data analysis, software development, figure creation, writing, and revising of this manuscript.

Chapter 4 is under review in:

Hedelius, J. K., Feng, S., Roehl, C., Wunch, D., Hillyard, P. W., Poldolske, J. R., Iraci, L. T., Patarasuk, R., Rao, P., O'Keeffe, D., Gurney, K. R., Lauvaux, T. and Wennberg, P. O.: Emissions and topographic effects on column CO_2 (X_{CO_2}) variations, with a focus on the Southern California Megacity, J. Geophys. Res.-Atmos., 2017. J.K.H. led this study and participated in design, conception, model development, data analysis, software development, figure creation, writing, and revising of this manuscript.

TABLE OF CONTENTS

LIST OF ILLUSTRATIONS

LIST OF TABLES

NOMENCLATURE

Acronyms

ACOS   Atmospheric CO_2 Observations from Space - algorithm used to retrieve X_{CO_2} from space-based radiance observations.

AFRC   Armstrong Flight Research Center, on Edwards Air Force Base (CA), formerly known as Dryden.

AK   Averaging kernel.

AR   Assessment Report published by the IPCC. The fifth is the most recent one, published in 2013.

AU   Arbitrary units.

CARB   California Air Resources Board.

CI   Confidence interval.

DMF   Dry-air mole fraction.

EGI   EM27/SUN GGG and interferogram processing suite.

FF   Fossil fuel.

FOV   Field of view.

FS   Frequency shifts.

FTS   Fourier transform spectrometer.

GCM   General Circulation Model.

GHG   Greenhouse gas.

GOSAT   Greenhouse Gases Observing Satellite.

ILS   Instrument line shape.

InGaAs   Indium Gallium Arsenide.

IPCC   Intergovernmental Panel on Climate Change.

IR   Infrared.

JPL   Jet Propulsion Laboratory.

KIT   Karlsruhe Institute of Technology.

LA   Los Angeles, California.

LANL   Los Alamos National Laboratory.

LES   Large-Eddy Simulations - a mode used with WRF.

LPDM   Lagrangian particle dispersion models.

LSE   Laser sampling error.

ME   Modulation efficiency - used in describing the ILS.

mFTS   mobile Fourier transform spectrometer - an acronym used to describe EM27/SUN spectrometers.

MOPD   Maximum optical path difference.

OCO-2   Orbiting Carbon Observatory-2.

OSDS   Observer-Sun Doppler Stretch.

PE   Phase error - used in describing the ILS.

pTz   atmospheric pressure, temperature, altitude.

QCF   Quality control filter.

RF   Radiative forcing.

rms   Root mean square.

SNR   Signal-to-noise ratio.

SoCAB   South Coast Air Basin.

SZA   Solar zenith angle.

TCCON   Total Carbon Column Observing Network.

WMGHG   well-mixed greenhouse gas.

WMO   World Meteorological Organization.

WRF   Weather Research and Forecast - atmospheric transport model.

ZPD   Zero path difference point.

Abbreviations

ifg   Interferograms.

Md   Median.

Chapter 1

INTRODUCTION

1.1 Motivation: Carbon dioxide, the greenhouse effect, and the carbon cycle

Carbon dioxide is the fifth most abundant gas in Earth's atmosphere (after N_2, O_2, Ar, and water). Its concentration has risen from 278 ppm (part per million, by volume) since pre-industrial times (1750) (Etheridge et al., 1996) by 45% to over 400 ppm today. The Industrial Era radiative forcing (RF) for CO_2 is 64% ($1.82\pm0.19\,\mathrm{W\,m^{-2}}$) of the total due to all well-mixed greenhouse gases (WMGHGs) (Myhre et al., 2013). Between Intergovernmental Panel on Climate Change (IPCC) Assessment Reports (AR) 4 and 5 (years 2005 and 2013 respectively), 85% of the increase in RF from WMGHGs was attributed to the increase in CO_2.

These changes in RF have been directly observed (Feldman et al., 2015). A change in RF of $4.8\,\mathrm{W\,m^{-2}}$ in the Coupled Model Intercomparison Project Phase 5 (CMIP5) is expected to lead to a 1.4–3.1 °C increase in surface temperature during the 21st century (Collins et al., 2013). Increases in RF also cause changes in ocean circulation, the water cycle, and the cryosphere. Global temperature increases are projected to threaten human health and mortality, and decrease biodiversity. An increase of ~2.5°C above pre-industrial (1750) levels is estimated to cause average global economic losses between 0.2 and 2.0% of income annually, (Pachauri et al., 2014).

It is uncertain what the change in RF will be in the future, so the CMIP5 uses four different Representative Concentration Pathways (RCP) corresponding to different RF levels. Though the RF from WMGHGs is well known, it is uncertain what their future mixing ratios will be. In particular, only about 45% of anthropogenic fossil fuel (FF), cement, and land use change CO_2 emissions remain in the atmosphere each year with the rest being taken up by the ocean or land. It is unclear how this uptake may change in the future, and it is unclear exactly which regions are taking up the carbon (especially for land). Further, it is unclear how FF CO_2 fluxes may change in the future due to mitigation efforts or lack thereof.

Mitigation goals have been set for national, state, and city levels (Fig. 1.1). Typically progress towards these goals has been evaluated using bottom-up inventory methods. These methods require accurate reporting of carbon emissions from various sectors.
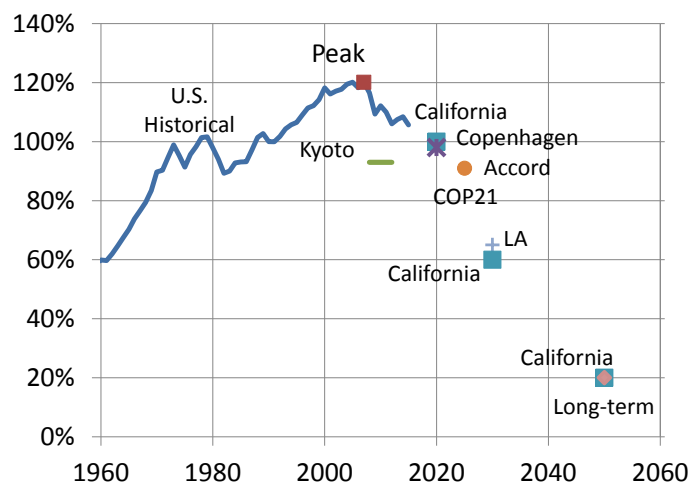
Figure 1.1: Historical United States (U.S.) fossil fuel and cement production CO_2 emissions and goals compared to 1990 levels. Historical emissions from `http://cdiac.ornl.gov/GCP/`. Los Angeles (LA) goal from Villaraigosa (2007). Much of the decline since the 2007 peak of 1.58 GtC yr^{-1} was a result of switching from coal to natural gas.

Accurate reports are not available for all areas. Further, the overall accuracy of bottom-up methods is not always well known. This suggests additional monitoring methods, especially top-down methods, are warranted to constrain our understanding of CO_2 fluxes.

1.2 Rationale: Existing data, work, and methods

Regular, accurate measurements of atmospheric CO_2 began in the 1950s using in situ and flask techniques (Keeling, 1998). Originally these data were limited to ground based observations, though later observations were collected from aircraft. In the 2000s, the Total Carbon Column Observing Network (TCCON) was started to make column measurements of CO_2 and to aid in future satellite measurements. Column measurements were also started after recognizing vertical mixing is difficult to parameterize in transport models, which can bias results (Yang et al., 2007); column measurements are less sensitive to vertical mixing. Only recently were accurate (better than 0.3%) satellite measurements over small ($<100\,km^2$) areas added to the mix of observation systems with the Greenhouse Gases Observing Satellite (GOSAT) launched in 2009 (Kuze et al., 2009), and the Observing Carbon Observatory-2 (OCO-2) launched in 2014 (Eldering et al., 2017).

These global observations have historically been implemented in General Circulation Models (GCMs), which are only modeled at resolutions on order of 1–5° (Baker et al., 2006). These Eulerian chemical transport models require considerable computational effort (Lin and Wen, 2015) and may be too coarse to distinguish urban areas, which cover only about 0.5% of ice-free land (Schneider et al., 2009). Lagrangian methods, including Lagrangian particle dispersion models, (LPDM) have been gaining popularity because of their computational efficiency for modeling select small areas and the information they provide on air parcel transport history. Lagrangian methods were applied to column measurements made around Berlin (Hase et al., 2015).

To recognize reductions in emissions from sources on the scale of cities across the globe requires implementation of a spatially and temporally dense observation dataset. Satellites are likely the only platform that can provide this data, and this type of data has only been available for the past few years. Even though space-based observations are currently limited (and would significantly benefit from additional platforms, such as the OCO-3 mission) they provide a basis for estimating emissions in conjunction with models. More importantly, they provide measurements which can be used to estimate changes in emissions with time. Errors and sources of bias need to be characterized to determine minimum detectable changes in emissions. Larger errors correspond to larger changes in emissions required to detect changes. Biases could be misinterpreted as a change in flux.

Much of the work in this thesis involves quantifying errors and biases from different observing and model systems. This information can aid in determining minimum observable flux changes. It can also be used to make improvements to the observation system or retrievals to reduce bias. For example, detectors with nonlinearity effects (Hedelius et al., 2016) were replaced with sufficiently linear dual detectors (Hase et al., 2016). Errors are estimated using a variety of observed and model data, and by examining effects of perturbations. There has been limited use of OCO-2 and TCCON observations with Lagrangian methods, and this thesis provides a method for their implementation.

1.3 Central questions

My work has centered around understanding CO_2 activity at the city level, in particular the South Coast Air Basin (SoCAB) containing the greater Los Angeles, California area. A central question to my work is "How much CO_2 is emitted from

the SoCAB?" or more specifically "On average much CO_2 was emitted in recent (past 4) years from the SoCAB as inferred from remote sensing measurements?" The null hypothesis is the amount is equal to what is reported by the California Air Resources Board (CARB). There are also several ancillary questions associated with this, some of which are:

- What is the error on this estimate?

- What are the largest sources of measurement error and/or bias?

- How could the behavior of the atmosphere in cities affect a flux estimate?

- Do ground and space-based observation platforms give similar estimates?

- Is on-the-ground infrastructure needed for city estimates of CO_2 fluxes, or can satellite observations be used? How scalable is this method to other cities?

- What additional information can be gleaned from measurements (e.g. temporal behavior)?

- How does the behavior of CO_2 relate with other gases and aerosol?

These questions are answered using a incremental approach, where errors from various sources are evaluated along the way.

1.4 Objectives

My incremental approach to answer the central question can be described by working backwards. Various sensitivity tests can be performed on the inversion model by perturbing meteorological parameters, prior estimates, and optimization methods. Central to inversions are CO_2 measurements, made here by TCCON or OCO-2. Accuracy and bias in OCO-2 measurements have been described by Wunch et al. (2016b). Here I estimate accuracy in TCCON measurements using an empirical approach. For this approach I needed a transportable comparison product—a portable FTS. An error budget for this portable FTS needed to be derived to determine its potential uses and limitations.

Going forward, these main objectives included:

1. Develop an semiautomated system to determine X_{gas} from the portable FTS.

2. Find and reduce the largest error sources from the portable FTS measurements.

3. Estimate TCCON site-to-site bias due to various instrumental and retrieval errors.

4. Empirically estimate site-to-site TCCON bias using co-located measurements with the portable FTSs.

5. Quantify the X_{CO_2} enhancement of the SoCAB compared to 'background.'

6. Estimate influences of differences in mixed-layer (ML) height on X_{gas} in areas with a sharp contrast between the ML and the free troposphere.

7. Develop and test an inversion scheme to quantify fluxes of CO_2 from the SoCAB using the observed enhancements.

8. Perform sensitivity studies on the inversion using different priors, subsets of data, and model schemes.

This strategy was developed to determine not only an estimate of flux, but just as important the errors on these estimates. My work has also focused on using scalable products that could be applied to many (100+) other locations.

1.5   Structure of Thesis

The reminder of this thesis is structured as follows. Chapter 2 addresses objectives 1 and 2. In it I describe the portable FTS instrument, how it compares long-term with TCCON, and various sources of error in the retrievals. In Chapter 3 I discuss results from a campaign where a pair of portable FTS instruments were taken to each of the 4 U.S. TCCON sites. I include empirical estimates and sources of bias and address objectives 3 and 4. In Chapter 4, I examined intracity variations in X_{CO_2}, including variations due to different weightings of the ML from changes in topography. I quantify the enhancements of X_{CO_2} attributed to local anthropogenic activity and focus on objectives 5 and 6. Chapter **??** discusses a Lagrangian-based inversion to quantify fluxes of different gases. It also includes results from sensitivity studies to meet objectives 7 and 8.

Chapters **??** and 5 focus on expansions of this work, including other past and future analyses. The focus of Chapter **??** is estimating relative aerosol optical depth properties from the portable FTS. It also includes applications of these estimates. Finally, in Chapter 5 I give brief descriptions of other projects I have worked on during my studies at Caltech. It also includes a discussion of areas where further

research is needed to better understand the atmospheric composition of not only the SoCAB, but also other locations.

Chapter 2

ASSESSMENT OF ERRORS AND BIASES IN RETRIEVALS OF X_{CO_2}, X_{CH_4}, X_{CO}, AND X_{N_2O} FROM A $0.5\,\mathrm{CM}^{-1}$ RESOLUTION SOLAR-VIEWING SPECTROMETER

Abstract

Bruker™ EM27/SUN instruments are commercial mobile solar-viewing near-IR spectrometers. They show promise for expanding the global density of atmospheric column measurements of greenhouse gases and are being marketed for such applications. They have been shown to measure the same variations of atmospheric gases within a day as the high-resolution spectrometers of the Total Carbon Column Observing Network (TCCON). However, there is little known about the long-term precision and uncertainty budgets of EM27/SUN measurements. In this study, which includes a comparison of 186 measurement days spanning 11 months, we note that atmospheric variations of X_{gas} within a single day are well captured by these low-resolution instruments, but over several months, the measurements drift noticeably. We present comparisons between EM27/SUN instruments and the TCCON using GGG as the retrieval algorithm. In addition, we perform several tests to evaluate the robustness of the performance and determine the largest sources of errors from these spectrometers. We include comparisons of X_{CO_2}, X_{CH_4}, X_{CO}, and X_{N_2O}. Specifically we note EM27/SUN biases for January 2015 of 0.03, 0.75, −0.12, and 2.43 % for X_{CO_2}, X_{CH_4}, X_{CO}, and X_{N_2O} respectively, with 1σ running precisions of 0.08 and 0.06 % for X_{CO_2} and X_{CH_4} from measurements in Pasadena. We also identify significant error caused by nonlinear sensitivity when using an extended spectral range detector used to measure CO and N_2O.

2.1 Introduction

Measurements of atmospheric mixing ratios of greenhouse gases (GHGs), including CO_2 and CH_4, are needed to aid in estimating fluxes and flux changes, and to ensure international treaties to reduce emissions are fulfilled. The Total Carbon Column Observing Network (TCCON) makes daytime column measurements of these gases. The Orbiting Carbon Observatory-2 (OCO-2) and Greenhouse Gases Observing Satellite (GOSAT) missions enable column GHG measurements with global coverage. These GHG monitoring satellites make measurements at one time of day and, therefore, lack the temporal resolution that a dedicated ground site provides.

Due to cost, lack of infrastructure, and stringent network requirements, there are limited ground sites on a global scale; e.g., there are no TCCON sites currently in operation in continental Africa, South America, or central Asia (Wunch et al., 2015), and there currently is no urban area with more than one TCCON site. Cheaper, portable, solar-viewing Fourier transform spectrometers (FTSs) can make contributions in these settings provided they have long-term precision. The Bruker Optics™ EM27/SUN, with the "SUN" indicating a built-in solar tracker, is a transportable FTS that may supplement global GHG measurements made by current networks (Gisi et al., 2012). This unit is small and stable enough to easily be transported for field campaign measurements, including measurements at multiple locations in 1 day. Column-averaged dry-air mole fractions (DMFs) of gases (X_{gas}) are retrieved from the EM27/SUN measurement, like the TCCON. X_{gas} is calculated from (Wunch et al., 2010):

$$X_{gas} = \frac{column_{gas}}{column_{dry\,air}} = 0.2095 \frac{column_{gas}}{column_{O_2}}, \tag{2.1}$$

where the 0.2095 factor is the fraction of dry air that is oxygen.

Retrieved X_{gas} has been compared with a co-located TCCON site in Karlsruhe, Germany, in past work for 26 days of X_{CO_2} retrievals from one EM27/SUN instrument (Gisi et al., 2012), and 6 days of both X_{CO_2} and X_{CH_4} retrievals from five EM27/SUN instruments (Frey et al., 2015).

Operators of these instruments have different end goals to better understand the carbon cycle. X_{CO_2} and X_{CH_4} retrievals from these instruments have been compared with satellite measurements in areas without a TCCON site (Klappenbach et al., 2015) as well as with satellite measurements in highly polluted areas (Shiomi et al., 2015). Emission flux estimates from the Berlin area ($< 30 \times 30\,km^2$) were made

by combining upwind/downwind measurements from five spectrometers and were compared with a simulation (Hase et al., 2015). Chen et al. (2016) have assessed gradient strengths around a large dairy farm ($\sim 100\,000$ cows) in Chino, California ($< 12 \times 12\,\text{km}^2$), using measurements from upwind/downwind spectrometers. Weather Research and Forecast Large-Eddy Simulations (WRF-LES, 4 km resolution) were used in combination with four simultaneous measurements to estimate fluxes from specific grid boxes in a subregion of the Chino dairy farm area, which is within a larger urban area (Viatte et al., 2016).

The column measurements used in these studies provide some advantages over in situ measurements, including less sensitivity to vertical exchange, surface dynamics, and small-scale emissions (McKain et al., 2012), which are difficult to model. Though column measurements can depend on mixed layer height in highly polluted areas, generally, column measurements depend primarily on regional-scale meteorology, and regional fluxes (McKain et al., 2012; Wunch et al., 2011a). For example, Lindenmaier et al. (2014) used observations from a single TCCON site to verify 1 day of emissions from coal power plants of about 2000 MW each at ~ 4 and 12 km away. Because of their large spatial sensitivity, column measurements are well suited for estimation of net emissions, model comparison, and satellite validation. A single site has been used to estimate Los Angeles, California (L.A.), emissions based on a sufficiently accurate emissions inventory and the observation that X_{gas} anomalies within L.A. are highly correlated (Wunch et al., 2009, 2016a). Generally though, a single column measurement site is insufficient to estimate emissions from an entire urban region (Kort et al., 2013). However, multiple column measurements can be combined to characterize part or all of an urban area (Hase et al., 2015; Chen et al., 2016; Viatte et al., 2016).

The main goal of this work is to quantitatively evaluate the robustness of EM27/SUN retrievals over a long period of time. This is accomplished by comparing retrievals from the EM27/SUN with a co-located standard (TCCON site) at Caltech, in Pasadena, California, United States. TCCON spectrometers make the same type of measurements (direct solar near-infrared) at high spectral resolution. Here we report X_{CO_2}, X_{CH_4}, X_{CO}, and $X_{\text{N}_2\text{O}}$ comparison measurements from an EM27/SUN. The X_{CO} and $X_{\text{N}_2\text{O}}$ measurements were made possible by a detector with an extended spectral range provided by Bruker™. The EM27/SUN X_{CO_2} and X_{CH_4} to TCCON comparison is the longest to date, 186 measurement days spanning 11 months. In part of January 2015, an additional three EM27/SUN instruments were at Caltech for

9 to 12 days of X_{CO_2} and X_{CH_4} comparisons to assess their relative biases. In Sect. 2.2 we briefly describe differences in instruments and the data acquisition process. In Sect. 2.3 we describe the retrieval software. In Sect. 2.4 we describe the inherent properties of EM27/SUNs such as instrument line shapes (ILSs), frequency shifts, ghosts, detector linearity, and external mirror degradation. Section 2.5 focuses on biases and sounding precision of different gases compared with the TCCON. Section 2.6 describes sources of instrumental error. We conclude with general recommendations of tests to perform on any new type of direct solar near-infrared (IR) instrument used to retrieve abundances of atmospheric constituents.

2.2 Instrumentation

2.2.1 TCCON IFS 125HR

All TCCON sites employ the high-resolution Bruker Optics™ IR FT spectrometer (IFS) 125HR that has been described in detail elsewhere (Washenfelder et al., 2006; Wunch et al., 2011a). For the Caltech TCCON site (34.1362° N, 118.1269° W, 237 m a.s.l.), the IFS 125HR uses an extended InGaAs (indium gallium arsenide) detector, covering 3800–11 000 cm^{-1} for detection and retrieval of all gases relevant to this study (O_2, CO_2, CH_4, CO, and N_2O). Figure 2.1 has example spectra from IFS 125HR and EM27/SUN instruments, with the spectral regions where individual gases are retrieved highlighted. Oxygen (O_2) abundance is useful in calculating the DMF because it represents the column of dry air and is combined with the column of the gas of interest to yield the DMF (Wunch et al., 2010).

The Caltech IFS 125HR uses a resolution of approximately 0.02 cm^{-1} (with a maximum optical path difference (MOPD) of 45 cm). It takes about 170 s to complete one forward/backward scan pair. TCCON sites have single sounding 2σ uncertainties of 0.8 ppm (X_{CO_2}), 7 ppb (X_{CH_4}), 4 ppb (X_{CO}), and 3 ppb (X_{N_2O}) (Wunch et al., 2010). TCCON data are tied to the World Meteorological Organization (WMO) in situ trace gas measurement scale through extensive comparisons with in situ profiles obtained from aircraft and balloon flights. We use the TCCON as a standard against which to compare the EM27/SUN instruments. TCCON data from this study are publicly available from the Carbon Dioxide Information Analysis Center (Wennberg et al., 2014c).

2.2.2 Caltech EM27/SUN

EM27/SUN spectrometers have been described elsewhere (Gisi et al., 2012; Frey et al., 2015; Klappenbach et al., 2015) so we focus on differences in setup and
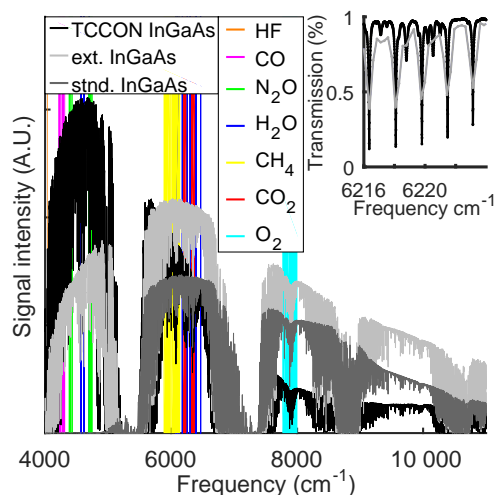
Figure 2.1: Example of scaled spectra from three different detector types, with retrieval windows highlighted. The spectrum from the EM27/SUN extended InGaAs detector was scaled 10 times more than the spectrum from the standard InGaAs detector.

acquisition here. The standard EM27/SUN configuration uses an InGaAs detector sensitive to the spectral range spanning $5500–12\,000\,\text{cm}^{-1}$, which permits detection of O_2, CO_2, CH_4, and H_2O (Frey et al., 2015). For this study, the Caltech EM27/SUN was delivered with an extended-band InGaAs detector sensitive to $4000–12\,000\,\text{cm}^{-1}$, which allowed for additional measurements of CO and N_2O (Fig. 2.1). All EM27/SUN spectrometers used in this study (Sects. 2.2.2, 2.2.3) used the typical MOPD of 1.8 cm, corresponding to a spectral resolution of $0.5\,\text{cm}^{-1}$. Interferograms (ifgs) were acquired in direct-current-coupled mode to allow post-acquisition low-pass filtering of brightness fluctuations to reduce the impact of variable aerosol and cloud cover effects (Keppel-Aleks et al., 2007). Ghosts were reduced as data were acquired by employing the interpolated sampling option provided by Bruker™ (see also Sect. 2.4.3). A 10 KHz laser fringe rate is used to reduce scanner velocity deviations, and each forward/backward scan took 11.6 s, or 5.8 s per individual measurement.

To be more consistent with the TCCON measurements, no spectrum averaging or interferogram apodization was applied before retrieving DMFs. We recommend averaging only after retrievals if disc storage and processor speeds are sufficient, so spurious data can be filtered. To test the pre- vs. post-averaging effect we used 9 retrieval days with 26 000 forward/backward measurements and used Bruker™ OPUS software to create spectra from ifgs. We compared retrievals from using five

Table 2.1: Pre-averaging and apodization effects on EM27/SUN retrievals.

% error	X_{CO_2}		X_{CH_4}		X_{H_2O}		X_{CO}		X_{N_2O}	
	Md.	σ	Md.	σ	Md.	σ	Md.	σ	Md.	σ
5 fwd/bwd pre-avgd.[a,b]	< 0.01	0.01	−0.02	0.01	0.36	0.13	< 0.01	0.15	0.30	0.12
NB med. apodz.[a,c]	0.29	0.09	−0.07	0.10	0.35	0.23	−1.01	0.58	−1.36	0.55

Measurement compared over 1–10 July 2014. Md denotes the median. NB denotes the medium Norton–Beer apodization. [a] As compared to retrievals from 1 fwd/bwd averaged non-apodized measurement averaged over same time post-retrieval. [b] Same apodization as standard. [c] Same pre-averaging as standard.

combined backward/forward measurements averaged pre-retrieval with those averaged post-retrieval. We also compared combined forward/backward measurements using a medium Norton–Beer apodization with those using no special apodization. Results are in Table 2.1 and suggest that different averaging methods cause only small inconsistencies, under ∼ 0.02 % for X_{CO_2} and X_{CH_4}.

The EM27/SUN was placed within 5 m of the Caltech TCCON solar tracker mirrors on the roof of the Linde+Robinson building (Hale, 1935). Measurements started on 2 June 2014 and, for this study, we include 186 measurement days that end on 4 May 2015. About 800 000 individual EM27/SUN measurements and 40 000 individual TCCON measurements were acquired over this period. Of these, about 580 000 and 15 000 were considered coincident and were not screened out by our quality control filters (QCFs). Our QCFs were conservative, and they required signal > 30 (Sect. 2.4.4), solar zenith angle (SZA) < 82°, 370 ppm < X_{CO_2} < 430 ppm, $X_{CO_2,error}$ < 5 ppm, $X_{CO,error}$ < 20 ppb, and $X_{CH_4,error}$ < 0.1 ppm. Other users may consider stricter QCFs. After averaging data into 10 min bins, there were about 6500 binned comparison points.

2.2.3 LANL and Harvard EM27/SUN instruments

Three additional EM27/SUN instruments were compared with the Caltech TCCON site in January 2015 – one owned by Los Alamos National Laboratory (LANL) and two owned by Harvard University (HU). To be consistent, all the acquisition and retrieval settings were the same as for the Caltech EM27/SUN. As opposed to the Caltech EM27/SUN (also abbr. cn), the LANL (abbr. pl) and HU instruments (abbr. ha and hb) used the original InGaAs detector type sensitive over 5500–12 000 cm^{-1} (Frey et al., 2015). The LANL instrument, however, has a different high-pass filter, allowing it to measure up to 14 500 cm^{-1}. This different filter is neither beneficial

nor disadvantageous to this instrument as no gas column amounts are retrieved in that region. The LANL instrument was first used in January 2014 and has been compared with multiple TCCON sites in the United States, including sites at Four Corners, LANL, NASA Armstrong, Lamont, Park Falls, and multiple Caltech comparisons (Parker et al., 2015). The HU instruments have been operational since May 2014 and were compared against each other at Harvard before traveling over 4100 km to Caltech. As noted by Gisi et al. (2012) and Chen et al. (2016), the ILS of these instruments is remarkably stable considering the long distances they traveled.

2.3 Retrieval software

SFIT (Pougatchev et al., 1995), PROFFIT ("PROFile fit", (Hase et al., 2004), and GGG (Wunch et al., 2015) are the three widely used retrieval algorithms to fit direct solar spectra and obtain column abundances of atmospheric gases. PROFFIT is maintained by the Karlsruhe Institute of Technology (KIT) and has been used to obtain DMFs from EM27/SUN instruments as well as NDACC-IRWG sites (Gisi et al., 2012; Frey et al., 2015; Hase et al., 2015). GGG is maintained by the Jet Propulsion Laboratory (JPL) and has been used to obtain DMFs from other low-resolution instrument measurements (e.g., an IFS 66, see Petri et al. (2012)), in addition to being used to retrieve DMFs from the MkIV spectrometer in balloon-borne measurements (Toon, 1991) and for the Atmospheric Trace Molecule Spectroscopy Experiment (ATMOS) flown on the space shuttle (Irion et al., 2002). GGG is the retrieval algorithm used by the TCCON (Wunch et al., 2011a). We chose to use GGG for our analysis because (1) we want to be consistent with the TCCON for comparison and (2) the GGG software suite containing GFIT is open-source allowing us to adapt routines if needed. We used the GGG2014 version for retrievals (Wunch et al., 2015).

All retrievals used the same pTz and H_2O modeled profiles as well as the same a priori profiles (Wunch et al., 2015). We also used the same meteorological surface data for retrievals from all five instruments. All retrievals also used the same 0.2 hPa surface pressure offset. This offset was determined by comparing measurements from the standard barometer with a calibrated Paroscientific Inc. 765–16B Barometric Pressure Standard that has a stated accuracy of better than 0.1 hPa.

2.3.1 Interferogram-to-spectrum – double-sided

TCCON uses an interferogram-to-spectrum subroutine part of GGG to perform fast Fourier transforms (FFTs) to create spectra from ifgs (Wunch et al., 2015). Though the Bruker™ OPUS software used to operate the spectrometer can also perform FFTs, we again chose to use GGG to maintain consistency. A developmental version of GGG was used, which was adapted to also allow FFT processing on EM27/SUN interferograms. GGG splits a raw forward/backward ifg into two different double-sided ifgs which are then FFTed to yield two spectra. GGG also corrects source brightness fluctuations (Keppel-Aleks et al., 2007).

2.3.2 EM27/SUN GGG and interferogram processing suite (EGI)

To make GGG retrievals simpler for new EM27/SUN users, an add-in software suite (EGI) was developed at Caltech to create correctly formatted input files. This suite is open-source and can be obtained through correspondence to the email address listed. EGI can be run using MATLAB or Python. EGI runs in UNIX, Mac OS, and Linux environments and runs GGG on multiple processors. EGI centralizes settings for paths to read and write files, it coordinates separately acquired ground weather station and GPS data with EM27/SUN ifgs, and it optimizes processing order. It also provides some ancillary calculations such as a spectral signal-to-noise ratio (SNR) calculation. EGI provides a simple way to turn on and off saving of ancillary retrieval files (i.e., spectral fits and averaging kernels). EGI can run for instruments employing one or two detectors, such as the type described by Hase et al. (2016). Like the GGG software suite, EGI also includes benchmark spectra acquired under different conditions to run simple tests on. EGI is automated, reducing the learning time as well as the amount of user time needed to retrieve DMFs. After an initial setup, EGI will run from ifgs to retrieved X_{gas} with two commands. On a computer with 1400 MHz processors the code takes ~ 30 s per CPU to process each interferogram from the EM27/SUN extended InGaAs detector.

2.4 Instrument characterizations and performance

2.4.1 Instrument line shape

Knowledge of the instrument line shape (ILS), or the observed shape of a spectral line from a monochromatic input, is crucial in assessing instrument performance and avoiding unknown biases in retrievals. Two parameters in the the LINEFIT algorithm (Hase et al., 1999) are used to characterize the ILS in relation to an ideal instrument, namely the modulation efficiency (ME) and phase error. ME and PE

Table 2.2: ILS of EM27/SUN instruments.

Instrument	9 January 2015		28 January 2015	
num – ID	ME[a]	PE (mrad)	ME	PE (mrad)
Caltech (42 – cn)	0.986	4.88	0.979[b]	3.58
LANL (34 – pl)	0.999	−1.34		
Harvard 1 (45 – ha)	0.973[c]	−1.99		
Harvard 2 (46 – hb)	0.991[c]	4.18	0.991	4.00

Missing values indicate ILS not characterized on that day. [a] Values are reported at MOPD. [b] After realigning this instrument the ME was as high as 0.994. [c] As reported by Chen et al. (2016).

both describe the interferogram and vary with OPD (Hase et al., 1999; Frey et al., 2015). PE is the angle between the real and imaginary parts of the FT of the ILS (Wunch et al., 2007). PE has an ideal value of 0 radians, and indicates the degree of asymmetry in spectral lines. ME is a measure of the normalized observed interferogram signal compared with that of a nominal instrument with an ideal value of 1 (unitless) (Hase, 2012). At maximum OPD (MOPD), an $ME < 1$ causes a broadening of the measured spectral lines, while an $ME > 1$ at MOPD causes a narrowing. The ILS can be calculated by analyzing absorption lines measured through a low-pressure gas cell, and varies with OPD (Hase et al., 1999). Here, we use only single ME and PE values at the MOPD (Frey et al., 2015) to describe the ILS. We characterized the ILS for the EM27/SUN instruments using the method described elsewhere (Frey et al., 2015; Klappenbach et al., 2015). This method is able to characterize ME to within 0.15 % using the LINEFIT algorithm (Hase et al., 1999), with supplemental MATLAB scripts for automation purposes (Chen et al., 2016). ILS can affect retrieved column values. We note that the ME at MOPD of the cn and ha instruments in Table 2.2 are significantly lower than those reported by KIT on campus of ∼ 0.997 (Frey et al., 2015), and post-campaign of ∼ 0.996 (Klappenbach et al., 2015).

For this study, the ILS is used to help explain biases, to demonstrate the stability of the instruments, and gives insight into how well the EM27/SUN instruments are aligned and their optical aberrations. Though GGG2014 retrievals do not account for non-ideal ILS, future versions of GGG will. For the current study, we assume that ILS impacts using PROFFIT will be similar to impacts using GGG. This assumption will need to be tested when GGG also can account for a non-ideal ILS. Because future GGG retrievals will be revised using historical ILS measurements, a need remains
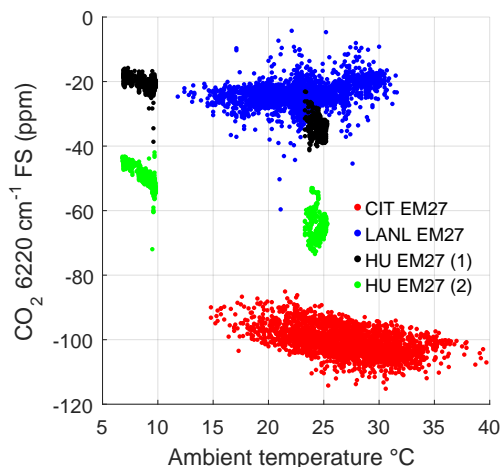
Figure 2.2: Frequency shifts (FS) of all four instruments vary with temperature because the lasers are not frequency-stabilized. FS for the CO_2 $6220\,cm^{-1}$ window are shown. FS of the Caltech (CIT) instrument are far from zero, so an empirical correction is made to correct the sample spacing number. Only every 300th CIT point and every 20th LANL point is plotted for clarity. HU EM27 1 and 2 are also referred to as ha and hb, respectively, by Chen et al. (2016).

to monitor the ILS both for future retrievals and as an indicator if realignment is necessary.

2.4.2 Frequency shifts

EM27/SUN units contain a HeNe 633 nm ($15\,798\,cm^{-1}$) metrology laser to sample the IR signal accurately as a function of the OPD. The laser is not frequency-stabilized (Gisi et al., 2012). This causes apparent spectral frequency to change with temperature as is shown in Fig. 2.2. Frequency shifts are affected by changes in the input laser wavenumber, laser alignment, and IR beam alignment. The input laser wavenumber will affect the spacing between spectral points. Since the frequency shift is furthest from zero for the Caltech EM27/SUN (on order of $-100\,ppm$, in red Fig. 2.2), the spectral spacing is empirically corrected in the EGI suite based on the CO_2 $6220\,cm^{-1}$ window frequency shifts. This made little difference for the primary gases of interest affecting X_{CO_2} by $0.015\,\%$ and X_{CH_4} by $-0.005\,\%$, though it did affect X_{H_2O} by $4\,\%$.

2.4.3 Ghosts

Ghosts are artificial spectral features linked to the aliasing of true spectral lines that arise in FTS spectra (Learner et al., 1996). The InGaAs detectors are optically sensitive at wavenumbers greater than half the HeNe metrology laser frequency

($7899 \, \text{cm}^{-1}$). To fulfill the Nyquist criterion and prevent aliasing, the IR interferogram is sampled twice each laser interferogram cycle, on the rising and falling edge. However, if the laser sampling is asymmetric — for example from a faulty electronics board — aliasing can still occur, folded across the half laser frequency (Messerschmidt et al., 2010). Because the asymmetry is typically small, the aliased signal, or ghost spectrum, is small compared with the true spectrum (Dohe et al., 2013; Wunch et al., 2015).

In EM27/SUN instruments the laser sampling error (LSE) can be minimized as data are collected by employing the interpolated sampling option provided by Bruker™. This resampling mode uses only the rising edge of the laser interferogram and assumes constant velocity in between the rising edges to interpolate the sampling (Gisi, 2014). We use a narrow band-pass filter (3 dB band width 5820–$6150 \, \text{cm}^{-1}$) in the Caltech EM27/SUN to test for LSE ghosts at $9800 \, \text{cm}^{-1}$. The ghost to parent ratio is 1.73×10^{-4} at a $10 \, \text{kHz}$ acquisition rate without the interpolated sampling activated. This ghost is eliminated with the interpolated sampling turned on. In actual solar tests, turning the interpolated sampling on and off had no noticeable effect on the DMF retrievals for the Caltech EM27/SUN; however this may not hold true for all instruments. The LSE ghost also disappeared at an acquisition frequency of $20 \, \text{kHz}$, and returned at higher acquisition frequencies. We opted for the recommended $10 \, \text{kHz}$ acquisition rate with the interpolated sampling on for all EM27/SUNs in this analysis because other instruments may be more significantly affected by LSE ghosts. A double-frequency ghost remains at $\sim 11\,900 \, \text{cm}^{-1}$ from radiation passing through the interferometer twice that is much larger than the LSE ghost, but is not in a region that will affect retrievals.

2.4.4 Mirror degradation and detector linearity

Solar tracking mirrors provided with the EM27/SUN instruments are gold with a protective coating. Gold is used because of its excellent reflectance in the near-IR and low reflectance in the visible region (Bennett and Ashley, 1965), which allows a high signal while reducing excess heating of the field stop and other optics. Through extended tests, we noted the first two mirrors (gold on plated aluminum, with a coating) degrade over time, with an e-folding degradation time of ~ 90 days as is shown in Fig. 2.3. Arbitrary units (AUs) for signal are the maximum ordinate values of the unmodified interferograms multiplied by 6450. The AUs of signal happen to be close to the spectral SNR — a scaling factor of 1.3 applied to the arbitrary signal has an R^2 of 0.63 relative to the SNR. Cleaning helped restore some

signal, but never to the original values. The mirror change may not have restored full signal because the rest of the optics were not cleaned at the time of the mirror change. Below the blue 150 AU line in Fig. 2.3 the fitted O_2 root mean square (rms) as a percentage of the continuum level dropped 26 times faster with signal intensity than above it. The instrument did come with an extra set of mirrors, but because mirrors are consumable parts, it adds recurring cost and effort to maintain these instruments long-term. After 1 year of use, the third mirror (gold coated glass) still remains completely intact. Feist et al. (2016) had success using steel mirrors under the very harsh conditions at the Ascension Island TCCON site, though at a cost of 35 % reflectivity per mirror. The JPL TCCON sites near Caltech noted no degradation on the external gold mirrors over more than 1 year of measurements. The lack of degradation on the third external mirror and the JPL TCCON mirrors is likely due to differences in how the mirrors were manufactured, including how the gold is applied to the substrate and the coatings used. Mirror degradation has likely not been a widely reported problem for most of the EM27/SUN community, perhaps because these instruments typically are stored indoors and only used for a few days for campaigns (for example, Frey et al. (2015)). However, this problem may affect mirrors on other EM27/SUN instruments when mirrors are exposed outside for extended periods of time.

With signal loss, we would anticipate that gas measurements would become noisier but remain unbiased. However, with time, the Caltech EM27/SUN X_{CO_2} and X_{CH_4} DMFs decreased relative to the TCCON DMFs as mirror reflectance decreased, and X_{CO_2} and X_{CH_4} increased when the mirrors were replaced. The TCCON IFS 125HR InGaAs detectors are already known to be sufficiently linear that no correction is required (Wunch et al., 2011a). We also performed a simple test repeatedly adding mesh screens in front of the entrance window to filter some of the light. In these tests X_{CO_2} and X_{CH_4} changed on order of 3 and 0.01 ppm, respectively, when using the extended InGaAs detector in the presence of filters transmitting ~ 25 % of the light. Figure 2.4 shows results from this test on X_{CO_2}; results from X_{CH_4} are similar. This provides strong evidence that the extended InGaAs detector is nonlinear. We repeated the test using the standard InGaAs detector, and changes in X_{CH_4} and X_{CO_2} biases were of the order of 10 times smaller and could be attributed to scattering off the mesh screen placed in front of the entrance window. Figure 2.5 shows the difference between the EM27/SUN and TCCON X_{CO_2} and X_{CH_4} as the total signal changed. After the mirrors were changed, the relative difference actually went up with some signal loss before decreasing again, for reasons we do not understand.
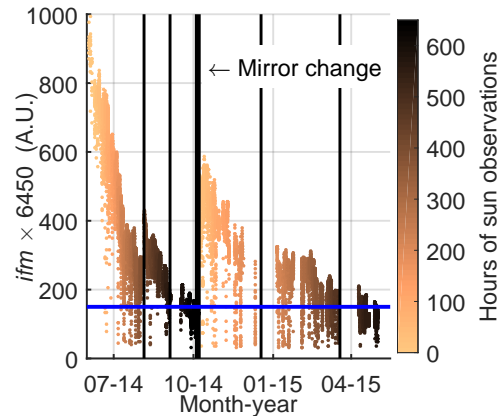
Figure 2.3: Interferograms from EM27/SUN instruments are negative, with the most negative ordinate values at ZPD and saturation occurring at -1. Here the interferogram maximums (ifm) refer to the maximum (least negative) ordinate values of the raw interferograms. They were normalized so the maximum is 1000 and are plotted with time showing the loss of signal. These values are affected by clouds, which are the cause for much of the scatter. They are also affected by SZA which explains some apparent intermediate increases. Only every 50th point is plotted for clarity. Mirror cleaning (thin black lines) helped restore some signal, but never to original values. The 150 AU line is in blue.

Detector nonlinearity in FTS instruments can be corrected in the ifgs post-acquisition in two ways. The first option deals with artifacts around the ZPD (zero path difference point) and is already included in GGG (Keppel-Aleks et al., 2007). When the ifg is smoothed, a nonlinear detector exhibits a dip around the ZPD which can be used to diagnose and reduce detector nonlinearity effects. EM27/SUN measurements are too noisy to properly characterize or detect this dip and so this correction is insufficient. The other option is to compare detector response with radiance from a controlled external light source, such as a blackbody, with very accurate radiation flux measurements (on order of 0.01%) (Thompson and Chen, 1994). By characterizing the response to the true flux as it is varied, the detector can be characterized and ifgs can be appropriately scaled and corrected. However, this requires extremely controlled precise measurements, as all nonlinearity is likely less than 1%, so measurements must be more precise than 1%.

An option to prevent nonlinearity from interfering with measurements is to only use the detector over its linear range by sufficiently attenuating the incoming sunlight. However, the SNR is already low so we opted against this method. Ultimately, we purchased the non-extended InGaAs detector at the loss of CO, and N_2O for future measurements for the Caltech instrument. For the historical field measurements we
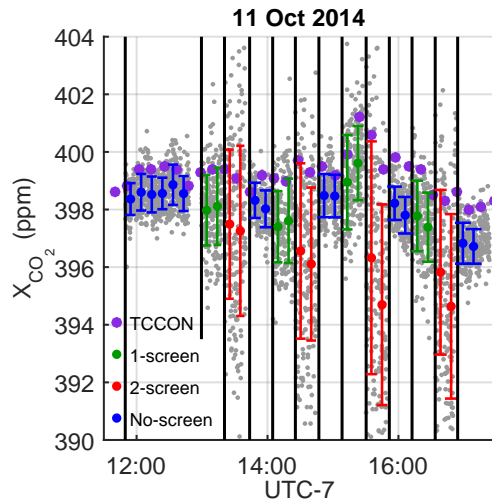
Figure 2.4: X_{CO_2} retrievals on 11 October 2014 when mesh screens were repeatedly moved in front of and away from the EM27/SUN (with extended InGaAs detector) entrance window. Gray points are all EM27/SUN measurements. Large points are 10 min averages. Error bars are 1σ. This test was performed a few days after the mirrors were replaced.

use a bias correction to match the TCCON for the nearest comparison days. The nonlinearity has nearly an equal effect for short times, but has a larger variation on multi-monthly scales as the mirrors degrade. In future measurements we recommend against using these extended InGaAs detectors. Addition of band-pass filters or use of different detectors will be necessary to provide high-quality measurements of CO, CO_2, and CH_4 (Hase et al., 2016).

The data shown in Fig. 2.5 were divided into bins based on the signal intensity and were separated before and after the mirror change. Within each bin the relationship was treated as approximately linear. Fits using fewer than 10 points or with correlation coefficients less than 0.1 were discarded. The change with half signal was calculated. The analysis was repeated for 10 bins and again for 20 bins. The weighted mean change in X_{CO_2} for halving the signal is -1.43 ppm in agreement with the mesh tests or

$$\Delta X_{CO_2}\left(\text{ppm}^{-1}\right) = 2.06\ln\left(S/S_0\right), \tag{2.2}$$

where S and S_0 are the final and initial signals respectively. This relationship holds for S and S_0 in the middle 80 %. For a similar methane analysis the mean change for half signal is -7.25 ppb or

$$\Delta X_{CH_4}\left(\text{ppb}^{-1}\right) = 10.5\ln\left(S/S_0\right). \tag{2.3}$$
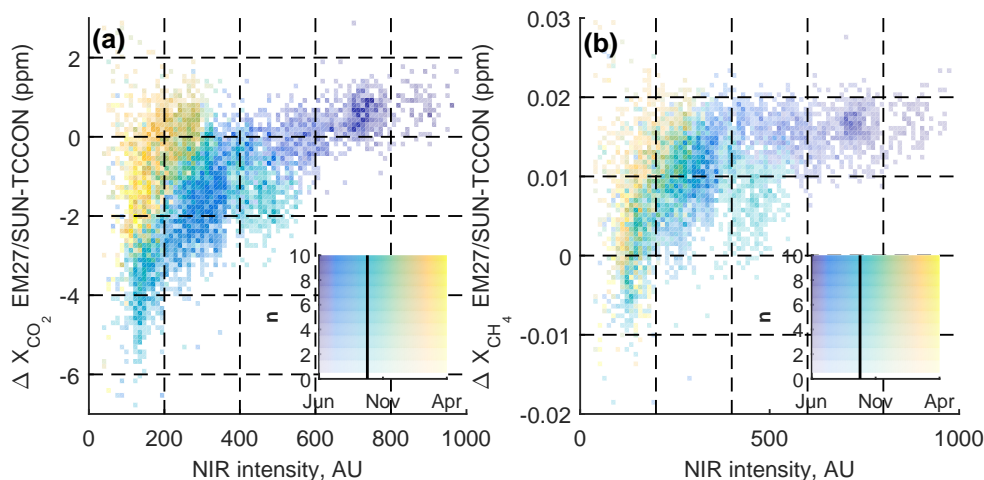
Figure 2.5: **(a)** The X_{CO_2} retrieved from the EM27/SUN compared to TCCON decreased with signal intensity for the first set of mirrors. In October the mirrors were changed, which caused the retrieved X_{CO_2} to increase. The inset is the legend for the average date and number of points in the histogram bins. **(b)** X_{CH_4} retrieved from the EM27/SUN compared with TCCON.

2.5 Comparisons with X_{gas}

GGG2014 includes an air-mass-dependent correction factor derived for TCCON X_{gas} measurements. The air mass correction factor for each gas is calculated using data obtained at a variety of relatively clean sites as described by Wunch et al. (2011a). We expect that the air mass dependence, which is due primarily to spectroscopic uncertainties, should be common for the same type of measurement. Parker et al. (2015) noted that the average EM27/SUN factors are similar compared to the TCCON for X_{CO_2} at three clean sites in the United States. The X_{CH_4} β factor was different (-0.0077 EM27/SUN, 0.0053 TCCON) but when applied here it worsened the R^2 and standard deviation of the comparisons. This could be because the air mass dependence of X_{CH_4} may not be solely from spectroscopic issues. Thus, we used the same air-mass-dependent correction factors as the TCCON.

To compare measurements between the TCCON and the EM27/SUN instruments, data were first averaged into 10 min bins to reduce the variance of binned differences (Chen et al., 2016). The median of the X_{CO_2} differences between sequential time bins is smallest (around 0.26 ppm) for 10 min bins over the entire ~ 11 month time period. Less averaging is more affected by noise, and more averaging starts to include instrument drift and true atmospheric variations. Averages were weighted using
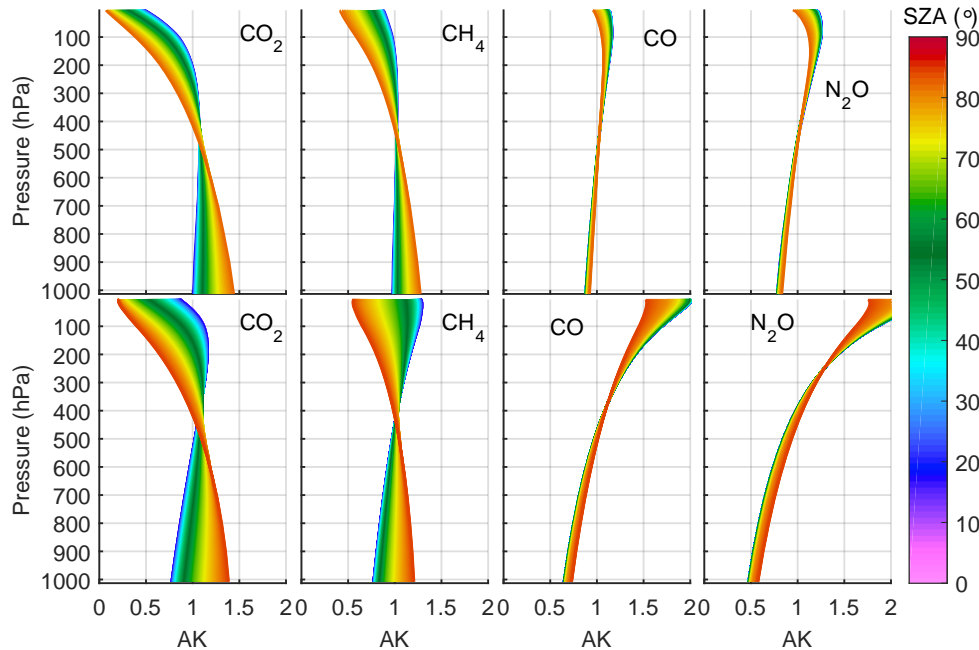
Figure 2.6: Top row: averaging kernels from the Caltech EM27/SUN instrument. Bottom row: averaging kernels from the TCCON.

retrieval errors $\hat{x}_{\text{err}}$ as in Eq. (4):

$$\bar{\hat{x}} = \frac{\sum_i \hat{x}_i \hat{x}_{i,\text{err}}^{-2}}{\sum_i \hat{x}_{i,\text{err}}^{-2}}, \tag{2.4}$$

where $\hat{x}_i$ is the retrieved value from the ith measurement in a bin, and $\bar{\hat{x}}$ is the bin average.

2.5.1 Averaging kernels

When comparing retrieved X_{gas} measurements (also denoted $\hat{c}$) from different remote sensing instruments, differences in their averaging kernels (AKs or $\vec{a}_i$, where i represents an instrument indicator number) and a priori profiles must be taken into account, using for example, the methods described by Rodgers and Connor (2003). Wunch et al. (2011b) compared GOSAT and TCCON total column DMFs using this method. Because GGG scales a priori profiles rather than retrieving the full profile, these AKs are vectors (i.e., column averaging kernels) rather than matrices.

Averaging kernels depend on several factors including how strong the lines are in the retrieval windows, and viewing geometry (e.g., SZA for solar-viewing instruments). Because the TCCON IFS 125HR and EM27/SUN instruments have different spectral resolutions, the apparent absorption strengths are different and so are the averaging

Figure 2.7: Example spectral fits and residuals ($\times 20$) from several of the retrieval windows from 28 June 2014, 10:55:16 (UTC$-$8), SZA = 17.1°. The primary species of interest and root mean square (rms) of the residuals are listed on the left. Other species fit in the window are listed on the right.

kernels. Averaging kernels for a gas differ for each microwindow. We combined AKs of a given gas from different microwindows using an unweighted average. Averaging kernels for the Caltech EM27/SUN for the GGG retrieval windows are shown in Fig. 2.6. Averaging kernels from the other EM27/SUN instruments are similar. TCCON averaging kernels have been discussed by Wunch et al. (2011a) and are shown on the bottom row in Fig. 2.6. As a numerical example, for X_{CO_2} measured at 50° SZA and 900 hPa using GGG, the AK is 1.10 for EM27/SUN instruments and 0.93 for TCCON instruments. This means EM27/SUN instruments are slightly more sensitive to a change in CO_2 near the surface relative to TCCON instruments. More importantly, they have the opposite sensitivity to an error in the a priori volume mixing ratio (VMR) profile at 900 hPa.

In our particular case, reducing the smoothing error using Eq. (A13) from Wunch et al. (2011b) and using the a priori as the comparison ensemble changes little as the effect of the differences in averaging kernels from the top of the atmosphere tends to cancel out the effect of differences at the bottom. TCCON and EM27/SUN a priori

profiles were the same in this comparison. However, we need to consider that the a priori profiles used in the retrieval are not representative of a highly polluted place, such as Pasadena, which is located in the same air basin as Los Angeles. Because differences in column measurements compared to background or a priori profiles occur primarily because of differences at the surface we can adjust retrievals for one instrument taking into account this knowledge using

$$\hat{c}_1 = \frac{a_{1,\mathrm{s}}}{a_{2,\mathrm{s}}} \left[\hat{c}_2 - c_\mathrm{a} \right] + c_\mathrm{a}. \tag{2.5}$$

Definitions of the terms in, as well as a discussion of assumptions needed to obtain Eq. (2.5) are in Appendix 2.A. We applied Eq. (2.5) to the X_{CO_2} and X_{CH_4} retrievals.

In summary, to compare biases between two instruments, we account for diurnal dependences, then average data into comparable time bins, and take into account our prior knowledge of the atmospheric profile and differences in averaging kernels.

2.5.2 Full comparisons of X_{gas} from extended-band InGaAs detector with a TCCON site

Gisi et al. (2012) noted that measurements taken within the first 30 min of moving the instrument to the roof and turning it on needed to be filtered out because of high scatter while waiting for the instrument to operate stably. We did not observe a similar requirement for our data. This could be because our instruments were not subjected to such fast temperature changes. It could also be because the laser frequency shift, which changes with temperature, does not seem to significantly impact our retrievals.

Examples of spectral fits from several of the retrieval windows are shown in Fig. 2.7 for a single spectrum. These are not necessarily representative of all the conditions under which the 800 000 spectra were acquired. The residuals are larger than those reported by Gisi et al. (2012) and Frey et al. (2015) because of the lower SNR from spectra recorded using the extended InGaAs detector.

The full time series (186 days) of the difference between the Caltech EM27/SUN and TCCON measurements is shown in Fig. 2.8. From this figure we see that X_{CO_2} and X_{CH_4} are the gases most affected by the mirror change in October 2014 (by about 3 ppm and 12 ppb respectively). For all gases, scatter of retrieved X_{gas} increases as signal decreases. Figure 2.9 shows the retrieved X_{CO_2} and X_{CH_4} from all four EM27/SUN instruments for 9–12 days in January 2015 plotted against those from TCCON. We report biases for January 2015 as scaling factors to approximate to the

Table 2.3: EM27/SUN to Caltech TCCON biases.

	Caltech, January	LANL, January	Harvard 1	Harvard 2	weighted % bias
n	285	241	187	164	
n days	12	12	9	9	
X_{CO_2}	0.9999 (*0.16*)	1.0006 (*0.14*)	1.0009 (*0.15*)	0.9998 (*0.15*)	0.03
X_{CH_4}	1.0069 (*0.19*)	1.0066 (*0.20*)	1.0103 (*0.14*)	1.0066 (*0.14*)	0.75
X_{H_2O}	0.9840 (*1.27*)	0.9791 (*1.44*)	0.9886 (*1.12*)	0.9791 (*1.01*)	−1.73
X_{CO}	0.9988 (*2.30*)				−0.12
X_{N_2O}	1.0243 (*0.42*)				2.43

Italicized values in parentheses are percent standard deviations as compared to the TCCON over the dataset for January 2015.
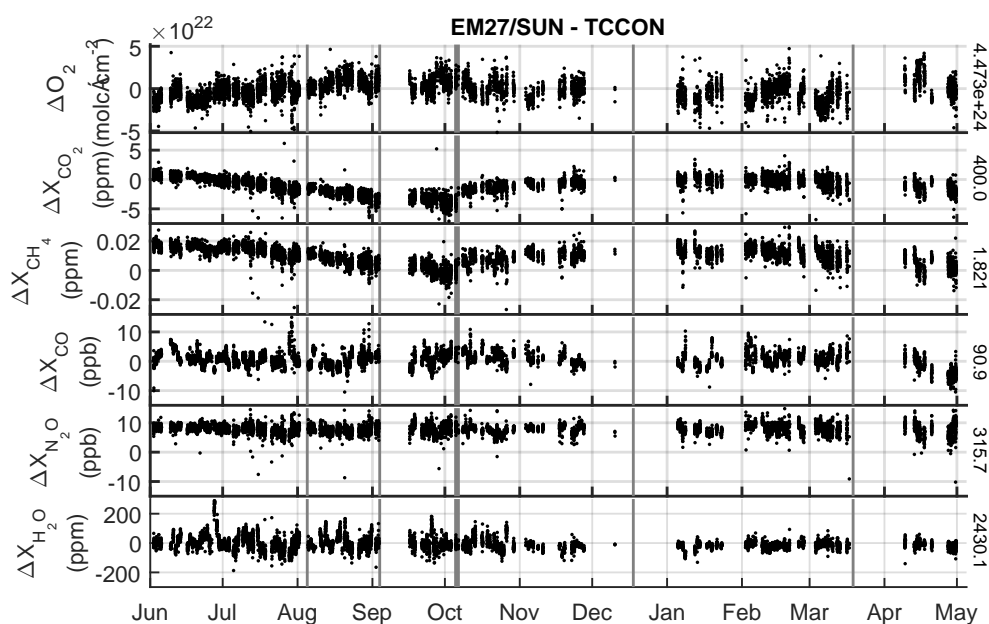
Figure 2.8: Full time series of EM27/SUN measurements as compared to TCCON from June 2014 to May 2015. Thin vertical gray lines represent mirror cleaning. The thick line represents the mirror change. To the right are TCCON means over time to get a sense of percent deviations.

TCCON, or scaling factors compared to 1. Biases were calculated using a linear least squares fit forced through the origin. A summary of the biases for all gases as compared to the TCCON is provided in Table 2.3.
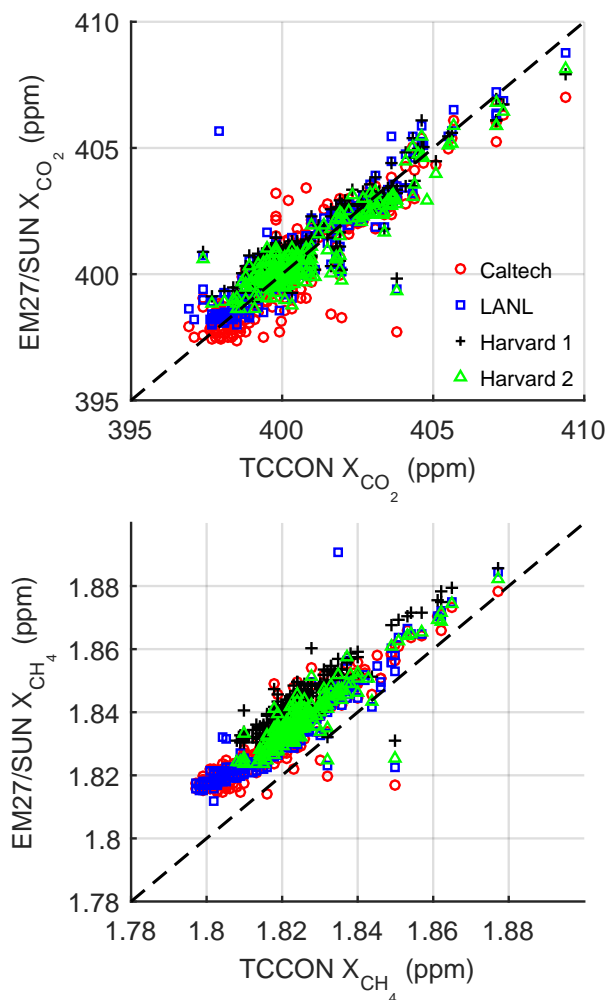
Figure 2.9: Retrieved EM27/SUN measurements (10 min averaging) as compared to the TCCON from January 2015. This provides a visual representation of the data – offset and scatter of data between X_{gas} from different instrument types – in Table 2.3. The black dashed line is the 1 : 1 line.

2.5.3 X_{CO_2}

We note a smaller bias in X_{CO_2} with respect to the TCCON (+0.03 %, see Table 2.3) compared to previous EM27/SUN studies (Gisi et al., 2012; Frey et al., 2015; Klappenbach et al., 2015). These previous studies retrieved X_{gas} from EM27/SUN spectra using PROFFIT. When compared with the TCCON X_{CO_2} retrievals, Gisi et al. (2012) noted a +0.12 % bias, Frey et al. (2015) noted a +0.49 % bias, and Klappenbach et al. (2015) noted a +0.43 % bias. Reasons for these differences could be from (1) spectroscopy differences between PROFFIT and GGG2014 used for EM27/SUN X_{gas} retrievals, (2) because Gisi et al. (2012) used an earlier version of GGG for TCCON retrievals, and (3) because Frey et al. (2015) and Klappenbach

et al. (2015) applied empirical corrections before comparing with the TCCON. In this section, we investigate two possible causes of bias: spectral resolution and instrument line shape.

Following Gisi et al. (2012), we attempted to determine whether the cause of the bias is due to the difference in spectral resolution between the EM27/SUN and TCCON instruments. Petri et al. (2012) also considered resolution bias in their study using a $0.11\,\mathrm{cm}^{-1}$ resolution instrument and an older version of GGG. They did not report a bias in X_{CO_2} retrievals, but noted that X_{CO_2} decreased by $\sim 0.12\,\%$ as interferograms were truncated to obtain spectra with resolutions of 0.02 to $0.5\,\mathrm{cm}^{-1}$. Most of the change occurred as the resolution changed from 0.1 to $0.5\,\mathrm{cm}^{-1}$ (see Fig. 11 therein). In contrast, Gisi et al. (2012) noted a $0.13\,\%$ increase in X_{CO_2} as the resolution changed from 0.02 to $0.5\,\mathrm{cm}^{-1}$ in PROFFIT. Here we find a $0.08\,\% \pm 0.16\,\%$ (1σ) decrease in X_{CO_2} when the resolution is decreased from 0.02 to $0.49\,\mathrm{cm}^{-1}$ in GGG, though part of this change would be offset by considering the differences in averaging kernels.

Previous studies noted an increase in X_{CO_2} of $0.15\,\%$ for a $1\,\%$ increase in modulation efficiency at max OPD (Gisi et al., 2012; Frey et al., 2015). Using PROFFIT we performed a similar test for spectra taken under various conditions at various times of day and obtained a similar result of a $0.10\,\% \pm 0.02\,\%$ (1σ) increase in X_{CO_2} for a $1\,\%$ increase in ME at the MOPD. For this study we assume that impacts of the ILS on retrievals will be similar in GGG and PROFFIT. Though we report a single value, there is an air mass dependence of $\sim 0.05\,\%$ increase in EM27/SUN PROFFIT retrievals for a $1\,\%$ increase in ME and air mass change of 1.

For instruments using the standard InGaAs detectors, the X_{CO_2} 10 min running 1σ precision is $0.075\,\%$ [0.034 to $0.18\,\%$, $95\,\%$ CI]. The wide confidence interval (CI) is from a combination of atmospheric variability being aliased into the running standard deviation as well as different SNRs among instruments. The spectral SNRs for measurements using this detector were in the range 1000–5000 and their precision for X_{CO_2} retrievals was only weakly correlated with $1/\sqrt{\mathrm{SNR}}$. Chen et al. (2016) found that the 1σ X_{CO_2} precision among 10 min binned EM27/SUN$_a$-EM27/SUN$_b$ differences is $0.01\,\%$. These data were acquired in a way that about 67 spectra were acquired every 10 min, and because two instruments were used, the single sounding precision is $\sim 0.01\,\% \times \sqrt{67/2} \approx 0.058\,\%$, which falls in our measured running 1σ precision range. Comparing to the TCCON, Gisi et al. (2012) reported that the 1σ daily precision is $0.08\,\%$. The extended InGaAs detector naturally has a lower

spectral SNR, in the range 100–1000, with a median of 400 over the full time series. Most of the variation in the SNR is due to loss of mirror reflectivity, but even with non-degraded gold mirrors, it is ~ 5 times lower because of the different detector. The median running 1σ precision over the full time series is 0.26 % for the X_{CO_2} product from the extended InGaAs detector. Because the SNR changed with time due to loss of mirror reflectivity, so did the precision. The correlation between $1/\sqrt{SNR}$ and running 1σ X_{CO_2} precision was strong ($R^2 = 0.75$) for retrievals from this detector and followed

$$\sigma_{XCO_2} = 0.17 + \frac{8.4}{\sqrt{SNR - 57}}. \tag{2.6}$$

An additional study we have not performed that could help in reducing bias would be to omit all or part of a CO_2 window with strong water lines. Because of the low resolution of these spectrometers (see inset Fig. 2.1), water lines and CO_2 lines often overlap. This can lead to inaccurate retrievals despite a good overall fit because H_2O and CO_2 can both be wrong, but in compensating ways. Reducing the size of a window would reduce precision but would decrease water and temperature sensitivity. This adjustment could also be performed for CH_4, which is retrieved over three windows in GGG.

2.5.4 X_{CH_4}

The EM27/SUN X_{CH_4} retrievals are 0.75 % higher than those of TCCON (see Table 2.3). In previous work, high biases of 0.47 % for a $0.11\,cm^{-1}$ instrument (Petri et al., 2012), and 0.49 % (Frey et al., 2015) and 1.87 % (Klappenbach et al., 2015) for EM27/SUNs, were noted. Petri et al. (2012) attributed most (0.26 %) of their bias to differences in resolution and noted for a single day that the bias increased as resolution decreased. In our simulations we find a 0.28 % $\pm$ 0.20 % (1σ) increase in X_{CH_4} when the resolution is reduced from 0.02 to $0.49\,cm^{-1}$. Using PROFFIT the impact of a 1 % decrease in ME is a 0.15 % $\pm$ 0.01 % (1σ) increase in X_{CH_4}. Again, although we report a single value there is an air mass dependence of about a 0.12 % decrease in X_{CH_4} using PROFFIT retrievals for an air mass change of 1, and a 1 % decrease in ME. Resolution and ME combined account for only half of the observed methane bias. Petri et al. (2012) suggested improper dry air mixing ratio and pT profiles, or spectroscopy as sources of error. Improper surface pressure, error in the calculated Observer-Sun Doppler Stretch (OSDS) due to pointing errors coupled with solar rotation, or error in the assumed field of view (FOV) may also contribute to the bias (see Sect. 2.6).

Chen et al. (2016) found that the 1σ X_{CH_4} precision among 10 min binned EM27/SUN$_a$-EM27/SUN$_b$ differences is 0.01 %, which is equivalent to a single sounding 1σ precision of ~ 0.058 %. Using the same method as for X_{CO_2}, the X_{CH_4} running 1σ precision from instruments using the standard InGaAs detectors is 0.057 % [0.037 to 0.25 %, 95 % CI], in agreement with Chen et al. (2016). The median running 1σ precision for X_{CH_4} from instruments using the extended InGaAs detector is 0.33 %. X_{CH_4} precision from the extended InGaAs measurements is also correlated with $1/\sqrt{SNR}$.

2.5.5 X_{CO} and X_{N_2O}

X_{N_2O} and X_{CO} were also measured using an EM27/SUN spectrometer in this study. Hase et al. (2016) have also reported on X_{CO} measurements using an EM27/SUN modified to include a second InGaAs detector with optical filters. Column CO measurements are desirable because CO is a tracer of combustion. Here these measurements were made possible because the extended detector is sensitive to the region 4200–4800 cm^{-1}, which contains useful windows where N$_2$O and CO molecules absorb IR radiation. Both the X_{CO} and X_{N_2O} retrievals are highly sensitive to changes in the modeled temperature profile. The nonlinearity of the detector had a less pronounced effect on X_{CO} and X_{N_2O} retrievals than it had on X_{CO_2} and X_{CH_4} retrievals (Fig. 2.8). X_{CO} and X_{N_2O} also have poorer precision than X_{CO_2} and X_{CH_4}, so any nonlinearity effect could be less than the noise. The 4200–4800 cm^{-1} spectral region is also affected differently from the nonlinearity than the 5000–7000 cm^{-1} region where column CH$_4$ and CO$_2$ are retrieved; the continuum levels changed more for the latter region. This may also explain in part why there is no noticeable change in X_{CO} and X_{N_2O} with signal. For X_{CO} the median 1σ precision is 3.7 %. In our simulations reducing the spectral resolution from the TCCON (0.02 cm^{-1}) to near the EM27/SUN (~ 0.5 cm^{-1}), X_{CO} decreases 2.5 % $\pm$ 4.2 % (1σ) in low-resolution spectra, and at Caltech this change varies with time.

In general, as is seen in Fig. 2.8, X_{N_2O} retrievals were highly scattered and had a large offset from TCCON. In our simulations, reducing the resolution from TCCON (0.02 cm^{-1}) to EM27/SUN (0.5 cm^{-1}) decreased X_{N_2O} by 1.5 % $\pm$ 0.6 % (1σ). Retrievals from the 4430 cm^{-1} window were low (~ 6 %), while the 4719 and 4395 cm^{-1} regions were biased slightly high (~ 1 %). The retrievals from the 4719 cm^{-1} region additionally had some long-term trends for reasons we do not understand. For X_{N_2O} the median 1σ precision is 1.9 %.
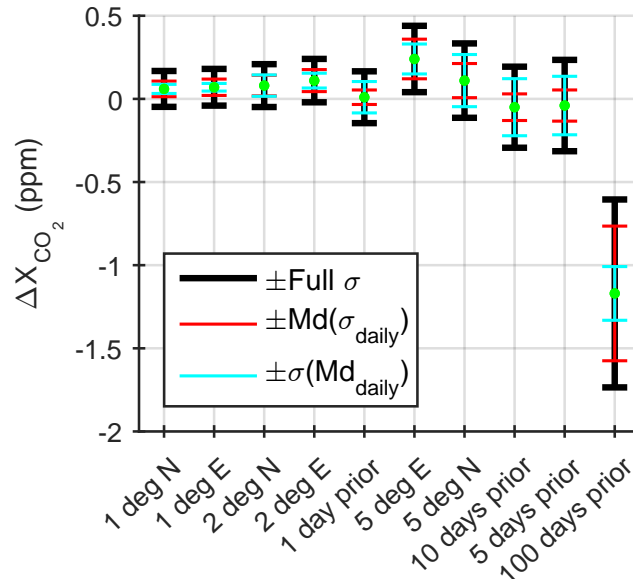
Figure 2.10: Standard deviations and biases from using wrong model pTz and H_2O profiles as compared to using the standard option for time and location. Tests are in order of increasing full σ. Red represents intraday variability. Cyan represents interday variability.

2.5.6 X_{H_2O}

Because of the significantly lower spectral resolution of the EM27/SUN spectrometers, the spectral band widths for the H_2O retrievals were increased as compared to the standard TCCON approach (Wunch et al., 2010). For lower resolution spectra, the H_2O lines appear much broader and the observed transmittance is much lower at the edges of standard TCCON spectral window. Thus, the spectral ranges of the low-resolution windows were expanded. Some of the standard TCCON windows used to retrieve H_2O had too few spectral points from the low-resolution instrument for good fits and were omitted. When expanding the windows, we ensured that no lines were admitted that made the effective ground-state energy E'' greater than $\sim 400\,cm^{-1}$. This reduces the temperature sensitivity to the modeled temperature profiles. As with the TCCON windows, we tried to keep a wide range of H_2O line strengths to accommodate large seasonal and site-to-site variations of the H_2O column. Windows were kept as wide as possible without encountering large spectral fitting residuals.

For X_{H_2O}, we find a median 1σ precision of 1.9 % from the instrument using the extended InGaAs detector. For instruments using the standard-InGaAs detectors, the X_{H_2O} 1σ precision is 0.81 % [0.36 to 2.12 %, 95 % CI].

Table 2.4: Meteorological sensitivity tests on EM27/SUN retrievals.

Error	X_{CO_2} Offset	Daily	X_{CH_4} Offset	Daily	X_{CO} Offset	Daily	X_{N_2O} Offset	Daily
+1 hPa surf	0.032	0.004	0.036	0.010	0.10	0.14	0.06	0.18
+10 K (surf – 700 hPa)	0.257	0.076	−0.006	0.036	10.1	1.2	0.53	0.23

Errors expressed as percentages. Daily is the median of the daily standard deviations, $Md(\sigma_{daily})$.

2.6 Sensitivity tests on retrievals

As with the TCCON, EM27/SUN retrievals require modeled atmospheric pressure, temperature, altitude (pTz), and water profiles (Wunch et al., 2015). Here atmospheric profiles are generated from the NCEP/NCAR 2.5° reanalysis product (Kalnay et al., 1996) by interpolating to the correct location at local noon of the desired day. These profiles also include the tropopause height which is used to vertically shift a priori profiles, as tropopause height can significantly affect column DMFs such as X_{CH_4} and X_{HF} (Saad et al., 2014). Selecting a profile for an incorrect location or day could lead to errors.

We ran test retrievals for the July 2014 period with incorrect profile information derived separately at latitudes north (1, 2, and 5°) and longitudes west (1, 2, and 5°) of our observation site, and well as from profiles derived 1, 5, 10, and 100 days prior to the measurement dates. In general, the profiles generated from a more distant location in space and time caused larger retrieval errors. For X_{CH_4} and X_{CO}, the main variability from the standard retrievals was in daily offsets (standard deviation of daily medians $\sigma(Md_{daily})$) which had values of 3 and 4 ppb respectively for the 100 day prior model. The medians of daily standard deviations $Md(\sigma_{daily})$ were 0.5 ppb for both X_{CH_4} and X_{CO} for the 100 day prior model. X_{N_2O} and X_{H_2O} also had more errors from $\sigma(Md_{daily})$, except for profiles within 2°, which more strongly affected diurnal variability $Md(\sigma_{daily})$. For these two species, the 100 day prior model $\sigma(Md_{daily})$ were 2 ppb and 50 ppm and $Md(\sigma_{daily})$ were 1 ppb and 20 ppm respectively. These values are shown for X_{CO_2} in Fig. 2.10 for all tested models. The 100 day prior model had $\sigma(Md_{daily})$ = 0.16 ppm and $Md(\sigma_{daily})$ =0.4 ppm, as well as a 1.2 ppm bias when using these models for X_{CO_2}.

Various user, instrumental, and measurement errors can reduce the accuracy and precision of retrievals. GGG uses retrieved O_2 column amount with the average DMF of O_2 (0.2095) to calculate the dry pressure column of air. However, to cal-

Table 2.5: Perturbations used in uncertainty budget.

Perturbation	Magnitude
ap[a] volume mixing ratio (VMR)	downshift by 1 km[b]
ap temperature	+1 K all altitudes
ap pressure	+1 hPa all altitudes
Pointing offset (po)	increased by 0.05°
Surface pressure	+1 hPa
Calculated OSDS[c]	+2 ppm
Field of view (FOV)	+7 %

See also Fig. 11. [a] ap denotes a priori. [b] ap VMRs were shifted independently. For X_{H_2O} and X_{HDO}, concentrations were decreased by 50 % at all levels. [c] OSDS = observer sun Doppler stretch.

culate the O_2 absorption coefficients, GGG takes into account the surface pressure, which can lead to measurement inaccuracies if the wrong surface pressure is used. Wunch et al. (2011a) reported a 0.04 % X_{CO_2} bias for a +1 hPa surface pressure offset in the TCCON. Similarly, we find a 0.032 % X_{CO_2} bias per +1 hPa surface pressure offset, with a 0.004 % σ variation on average throughout a day. Because the pressure offset affects O_2 retrievals, the other species are also affected (Table 2.4). X_{CO} may be particularly affected by a pressure bias because such a large fraction of the column CO is near the surface.

Using the same July 2014 dataset used to test the sensitivity of the retrievals to error in the pTz profile and surface pressure, we further estimated the sensitivity to error in the temperature in the lower atmosphere (surface – 700 hPa). GGG uses a single temperature profile per day that represents the local-noon temperatures, and the surface temperature is extracted from that profile. Such temperature error can arise in particular at the beginning and end of the day when the temperature is typically cooler than at noon. Here we derived the sensitivity of the retrievals to a +10 K error in the lower atmosphere (Table 2.4). X_{CO} has a significantly larger bias than the other species, likely because water absorption lines are the strongest spectral features in the CO retrieval window and water absorption lines are highly sensitive to changes in temperature. Water lines are also much stronger than N_2O lines in the N_2O windows. These tests suggest that offsets under 1 hPa and 1 K would cause small (~ 0.1 ppm) biases on X_{CO_2}, but a 4 K difference in near-surface (ground – 700 hPa) temperature could cause ~ 0.4 ppm bias in X_{CO_2}, which is larger than our reported 1σ precision. For other studies using multiple spectrometers and multiple
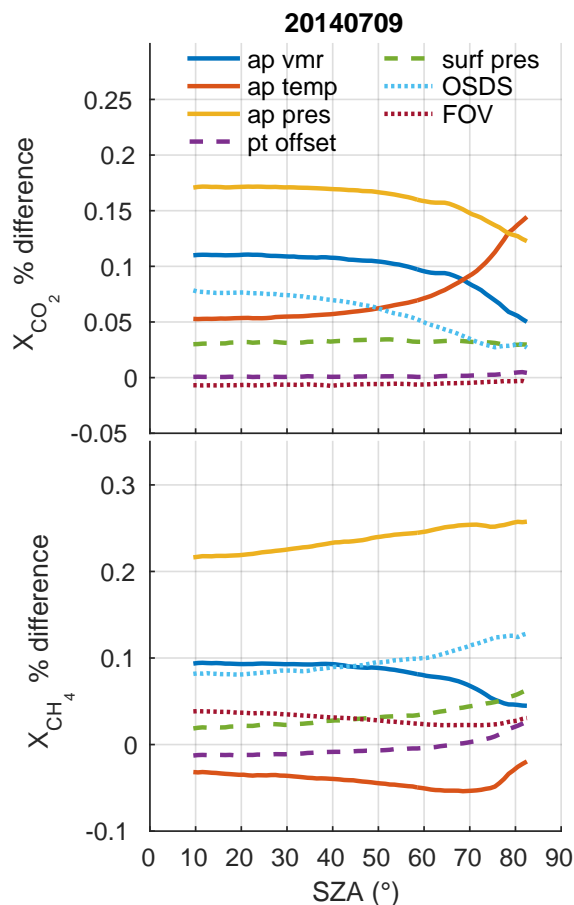
Figure 2.11: Uncertainty budget for EM27/SUN instruments using GGG2014. See Table 2.5 for magnitudes of perturbations.

meteorological measurements for X_{gas} retrievals, we recommend cross-comparing meteorological measurements to eliminate bias – preferably to a standard.

Finally, we perform a sensitivity study following the methodology of Wunch et al. (2015). The magnitudes of the applied perturbations are in Table 2.5. The results of this uncertainty budget study are presented for a day for X_{CO_2} and X_{CH_4} in Fig. 2.11. We do not include a sum in quadrature because we do not have an exhaustive list of sources of uncertainty. This uncertainty budget indicates that the low-resolution instruments are especially sensitive to biases in a priori pressures and a priori volume mixing ratio (VMR) profiles. Some of these errors may partially account for the unexplained long-term drifts we noted compared to TCCON that are unrelated to signal (e.g., Fig. 2.8, October–November 2014). For example, surface pressure and calculated Observer-Sun Doppler Stretch (OSDS) were correlated with EM27/SUN to TCCON X_{CO_2} differences in the long-term measurement. However, there was no apparent trend in the spectral residuals from fitting solar lines as the OSDS changed

Figure 2.12: Time series comparison of EM27/SUN retrievals to retrievals from the 0.5 cm^{-1} resolution IFS 125HR spectra.
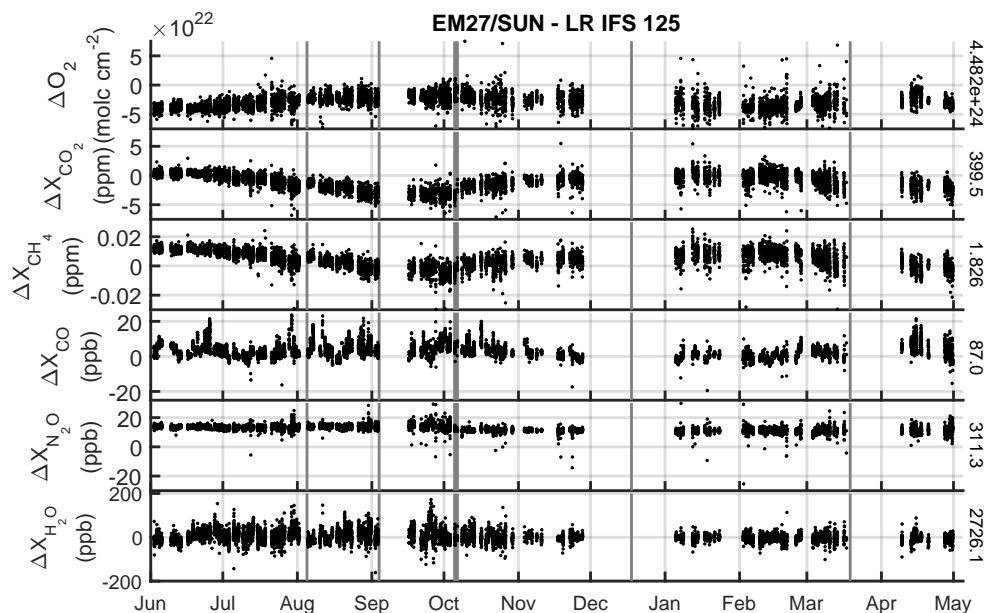
so these correlations may not indicate cause.

Differences in X_{gas} between different instruments are due to a combination of differences in resolution, and real instrumental imperfections and instabilities. To attempt to distinguish between resolution causing differences (e.g., by limitations in the forward model) or instrumental issues, we repeat the test performed by Gisi et al. (2012, Fig. 11 therein) of truncating IFS 125HR interferograms for the full time series. Results are shown in Fig. 2.12. Mean values for X_{CO_2} are slightly lower because of differences from retrievals on spectra of different resolutions, as described in Sect. 2.5.3. When comparing 10 min averaged TCCON data with lower resolution IFS 125HR retrievals we note monthly standard deviations on order of 0.15 % for X_{CO_2} and X_{CH_4}. This suggests the standard deviations of comparing retrievals from the EM27/SUN with the TCCON (Table 2.5) on these timescales are close to the current precision limits for directly comparing X_{CO_2} and X_{CH_4} retrieved from spectra of these different resolutions. Results in Fig. 2.12 are slightly more scattered than in Fig. 2.8 and have different offsets. The data still show an increase in X_{CO_2} and X_{CH_4} in October–November 2014 for reasons we do not understand, and unfortunately we have no ILS characterizations over this period.

Long-term drifts may or may not affect instruments employing the standard InGaAs detector and may be eliminated by future retrieval updates. They may also arise in

part from how the comparison was made, e.g., the assumptions to derive Eq. (2A.4) may not be valid for CH_4 and N_2O. As a follow-up study, brief 5–6 day comparisons using a standard InGaAs detector were made for the months of August, September, and November 2015. Scaling factors varied from 0.99905 to 1.00001 for X_{CO_2} and from 1.01228 to 1.00893 for X_{CH_4}, with larger day-to-day variability. Long-term (1 year or more) comparisons of these instruments employing the standard-InGaAs detector are needed before claims of long-term accuracy can be made or the full magnitude of drift can be quantized. Errors that could lead to drifts likely would be correlated amongst all EM27/SUN instruments, so the comparison would need to be against a standard such as the TCCON. Future studies may also benefit from comparing results using different retrieval algorithms, as the magnitude of errors that may lead to drifts in X_{gas} may vary among algorithms. Meanwhile, operators have already found many purposeful ways to use these instruments that require only short-term (about 1 month) precision without any assumptions about precision for longer time periods (for example Hase et al. (2015); Chen et al. (2016); Viatte et al. (2016)). Studies using these spectrometers independently longer term can also be performed depending on the degree of precision required. Limits on precision described herein are likely to only improve in future work.

2.7 Conclusions

Despite the challenge associated with the extended InGaAs detector and mirror degradation, the EM27/SUN instruments perform well on short timescales with 1σ running 10 min precisions of 0.075 % for X_{CO_2} and 0.057 % for X_{CH_4} retrieved from measurements using the standard InGaAs detectors. These instruments perform well in terms of mobility and stability, maintaining alignment despite frequent movement and jostling – an ideal characteristic of mobile FTS instruments. Measurements from the standard detector are precise enough to be used for campaigns of up to a few months and to provide useful supplementary X_{gas} measurements to established networks like TCCON. However, we recommend regular – 6 months to 1 year depending on use – comparison with established measurements (e.g., a TCCON site) to account for long-term drift. The frequency of comparison with established measurements may need to be reevaluated when more long-term comparison data become available. Simultaneous use of several EM27/SUN instruments may also help characterize drift. We also recommend regular – about monthly depending on use – ILS characterization. Our experience also suggests that use of the extended InGaAs detector without limiting the spectral band-pass in the EM27/SUN

Table 2.6: Tests for assessing biases and sensitivities of solar-viewing, remote sensing instruments.

Assessment	Test/observation	Type	Accepted correction[a]	Root cause	Similar instr. effect	EM27/SUN test
Incoming radiation attenuation effect	Gray filter after solar tracker & before interferometer	M	Recom'd replace detector. Alt. empirical	Detector non-linearity	Consistent for same detectors	Sect. 2.4.4
ILS	Measure with low-p gas cell (preferred), stable laser, or ambient air (least recom'd)	M	Retrievals with non-ideal ILS	Instrument misalignment; in-built	Potentially large differences	Gisi et al. (2012); Chen et al. (2014); Frey et al. (2015); Sects. 2.4.1 (measured), 2.5.3, 2.5.4 (impacts)
	Adjust FOV (if ILS is measured but not accounted for in retrieval)	RIA	Not recom'd			
Ghost to parent ratio	Use blackbody source & narrow band filter post-interferometer	M		Laser mis-sampling	Likely similar, potentially large diffs	Gisi et al. (2012); Frey et al. (2015); Sect. 2.4.3
Ghost effects	Measurements with & without ghost correction (e.g., XSM, or ifg resampling before FFT)[b]	M or RIA	Recom'd interpol. during acq or post-resampling	Laser mis-sampling	Likely similar, potentially large diffs	Sect. 2.4.3
Frequency shifts	Changes or large 0 offset	O & RIA	Input spectral spacing	Improper laser wavenumber, misalignment of laser or NIR beam	Shifts differ, effect similar	Sect. 2.4.2
Solar gas stretch	Changes or large 0 offset	O & RIA	OSDS	Poor spectral fits of solar lines; SE or res.	Similar for same detector & res.	Sect. 2.6
Spectral fitting windows	Width, locations	RIA		Instrument resolution requires adaptation	Same for similar res. (widths) & detector (locations)	Gisi et al. (2012); Sect. 2.5.6 (H_2O) Sect. 2.5.3 (discussion)
Averaging kernels	Used when comparing with a different instrument type	O	Rodgers and Connor (2003) and prior info.	Diff. sensitivity at atmos. layers from differing resolutions[b] & VG	Same for similar res., microwindows & VG	Sect. 2.5.1
SZA artifacts	Multi-day measurements in clean location	O	Empirical[a] (Wunch et al., 2011a)	ILS, or SE	See ILS entry	Frey et al. (2015); Parker et al. (2015)

Table 2.6 (cont.):

Assessment	Test/observation	Type	Accepted correction[a]	Root cause	Similar instr. effect	EM27/SUN test
Long-term artifacts	Preferred co-location with accepted measurements (e.g., TCCON)	O		Various (e.g., instrument settling, changing alignment, other)	May widely differ	Herein – for extended InGaAs only
Region/zone dependence	Co-location with spatially distributed accepted measurements	O/M		A priori insufficiencies	Likely similar	Parker et al. (2015)
Surface pressure effects	Manually adjust pressure inputs.	RIA	Accurate barometer pres. calibr.	Poor calculation of O_2 column, directly or by poor fitting	Similar effects for similar resolutions	Sect. 2.6
pTz & H_2O model profile sensitivity	Adjust modeled meteorological profiles	RIA	Improve met. profiles	Non-representative pTz+H_2O profile	Similar effects for similar resolutions	Sect. 2.6
A prori VMR surface sensitivity	Adjust a priori VMR near surface	RIA	Improve a priori profiles; reduce effect with AKs	Non-representative VMR profile (e.g., polluted mixed layer)	Similar effects for similar res. & true VMR profile	Parker et al. (2015)
Opt. avg. time	Allan type plot; e.g., Chen et al. (2016)	O	Empirical	SNR & true atmospheric variation	Depends on SNR & location	Chen et al. (2016) Sect. 2.5
Resolution effects	Truncate high-resolution ifg	RIA	Apply offset	Inst. res.	Similar for all solar-viewing insts.	Gisi et al. (2012); Petri et al. (2012) Sects. 2.5.3–2.5.6
Uncertainty budget for current fitting algorithm	Various, test on each new algorithm (Wunch et al. 2015)	RIA	Informative	Various	Similar effects for similar resolutions	Sect. 2.6

M denotes measurement (setups/adjustments required before acquisition), RIA denotes retrieval input adjustment (post-data acquisition, pre-retrieval), O denotes observation post-retrieval (may require prior planning of locations of measurements or longer term measurements), SE denotes spectroscopy errors, VG denotes viewing geometry, res denotes resolution.

[a] Though empirical corrections are occasionally accepted, it is always recommended to correct the underlying problem(s) if possible.

[b] XSM is Bruker™ code for interpolation during acquisition.

[c] GGG can provide ifg resampling if two detectors are on instrument. Note that the preferred correction is always of the root cause.

is incompatible with X_{CO_2} and X_{CH_4} retrievals that are precise long-term.

In general, we recommend all new ground-based, solar-viewing, remote sensing FTS instruments to undergo some or all tests listed in Table 2.6 to evaluate their performance. We also recommend comparisons of retrieval outputs to those of existing instrumentation (e.g., TCCON or NDACC-IRWG). These tests assume that one of the three widely used and accepted retrieval algorithms (GGG, PROFFIT, and SFIT), known to provide accurate spectral fitting, is used. New retrieval algorithms should be subjected to additional comparisons with currently accepted algorithms. Some of the results of these tests will be similar across all instruments of a given type, and so do not need to be repeated if they have been performed on another instrument elsewhere.

2.A   Assumptions and limitations in the AK correction

To derive Eq. (2.5), we begin with Eq. (22) in Rodgers and Connor (2003):

$$\hat{c}_i = c_a + \sum_k h_k a_{i,k} \cdot \left(x_{t,k} - x_{a,k} \right) + \epsilon_i. \tag{2A.1}$$

To include the pressure-weighting function $\vec{h}$ (Connor et al., 2008), we have used summation notation. The "hat" represents a retrieved value, c represents a column (scalar) value, and ϵ is the error. Subscript i is for a particular instrument, subscript a represents the a priori, subscript k is for a particular atmospheric layer, and subscript t represents the true atmosphere. The vectors $\vec{a}$ and $\vec{x}$ represent the column averaging kernel and atmospheric VMR profile respectively. This equation is derived from Eq. (1) in Rodgers and Connor (2003) using a Taylor series expansion about the a priori profile, and assuming linearity about it.

To compare retrievals from remote sounding instruments, a comparison profile (also called the comparison ensemble mean, denoted x_c) is used. Here, we have used the daily a priori profiles, which were the same for all instruments, as the comparison profiles. We note, however, that the comparison profiles should describe the real atmosphere as far as possible (Rodgers, 2000). Though the a priori profile has a drawdown in CO_2 from the biosphere near the surface, the real atmosphere in Pasadena is polluted near the surface. Thus this choice of comparison profiles is not ideal in our situation.

If we ignore retrieval error in Eq. (2A.1), and further assume that $\vec{x}_t = \vec{x}_a$ except at

the surface, it can be rewritten as

$$\frac{1}{a_{i,s}} \left(\hat{c}_i - c_a\right) = h_s \left(x_{t,s} - x_{a,s}\right),$$ (2A.2)

where the subscript s represents a surface value. If we are comparing measurements from two different instruments, $i = 1$ and $i = 2$, in the same location, $x_{t,s}$ and h_s are the same. Because the a priori profiles are also the same,

$$\frac{1}{a_{1,s}} \left(\hat{c}_1 - c_a\right) = \frac{1}{a_{2,s}} \left(\hat{c}_2 - c_a\right),$$ (2A.3)

which can be rewritten as

$$\hat{c}_1 = \frac{a_{1,s}}{a_{2,s}} \left(\hat{c}_2 - c_a\right) + c_a.$$ (2A.4)

Even in the absence of error, retrievals from instruments with different averaging kernels will still differ.

We adjust the EM27/SUN X_{CO_2} and X_{CH_4} retrievals using Eq. (2A.4) before comparison with the TCCON, which adjusts X_{CO_2} by up to ~ 1.2 ppm and X_{CH_4} by up to ~ 8 ppb. Future work could improve on this methodology using a better comparison ensemble or more representative a priori profiles for retrievals from measurements in Pasadena. This correction is not applied to X_{H_2O} because the AKs vary more among spectra because of larger variations in absorption strengths. It is also not applied to X_{CO} and X_{N_2O} because using $\vec{x}_t = \vec{x}_a$ is too poor of an assumption and makes the comparison worse between the TCCON and EM27/SUN retrievals in terms of R^2.

Competing interests
The authors declare that they have no conflict of interest.

Acknowledgements

Edited by: F. Hase

Reviewed by: M. K. Sha and one anonymous referee

Chapter 3

INTERCOMPARABILITY OF X_{CO_2} AND X_{CH_4} FROM THE UNITED STATES TCCON SITES

Abstract

The Total Carbon Column Observing Network (TCCON) has become the standard for long-term column-averaged measurements of CO_2 and CH_4. Here, we use a pair of portable spectrometers to test for intra-network bias among the four currently operating TCCON sites in the United States (US). A previous analytical error analysis has suggested that the maximum 2σ site-to-site relative (absolute) bias of TCCON should be less than 0.2 % (0.8 ppm) in X_{CO_2} and 0.4 % (7 ppb) in X_{CH_4}. We find here experimentally that the 95 % confidence intervals for maximum pairwise site-to-site bias among the four US TCCON sites are 0.05–0.14 % for X_{CO_2} and 0.08–0.24 % for X_{CH_4}. This is close to the limit of the bias we can detect using this methodology.

3.1 Introduction

The Total Carbon Column Observing Network (TCCON) is a network of ground-based spectrometers that record near infrared (IR) direct solar spectra from which column abundances of greenhouse gases are retrieved (Wunch et al., 2011a, 2015). Column average dry-air mole fractions (DMFs, or X_{gas} where "gas" is the species of interest) measured by multiple TCCON sites are used to evaluate X_{gas} retrievals from satellite measurements (for example, Dils et al. (2014); Kulawik et al. (2016); Nguyen et al. (2014); Wunch et al. (2011b). TCCON measurements are tied to the World Meteorological Organization (WMO) in situ trace gas measurement scales through extensive comparisons with in situ DMF profiles obtained by balloon and aircraft measurements (Deutscher et al., 2010; Geibel et al., 2012; Messerschmidt et al., 2011; Washenfelder et al., 2006; Wunch et al., 2010).

Table 3.1: Number of measurements prior to any filtering.

Site	Dates	No. TCCON	No. CIT mFTS	No. LANL mFTS	No. Co.*
Caltech-1	10 Aug–15 Aug	708	22 338	18 119	145
AFRC	17 Aug–21 Aug	1831	31 980	22 402	283
Caltech-2	22 Aug–28 Aug	740	26 406	22 382	269
Lamont	31 Aug–4 Sep	1146	31 814	32 454	250
Park Falls-1	7 Sep–11 Sep	369	14 820	13 746	79
Park Falls-2	12 Sep	187	6018	6130	44

* Co. indicates 10 min averaged two-way coincident mFTS and TCCON data points.

For the TCCON to meet the goals of satellite validation and carbon cycle flux estimates, measurements need be precise and accurate. Currently, the 2σ single sounding uncertainties of the TCCON are estimated to be 0.8 ppm (0.2 %) X_{CO_2} and 7 ppb (0.4 %) X_{CH_4} (Wunch et al., 2010). Systematic errors such as spectral ghosts (Messerschmidt et al., 2010), pressure offsets, instrument misalignment, or improper fitting of the continuum curvature (Kiel et al., 2016) can, however, produce systematic biases between sites that will remain even after averaging many single sounding measurements. An error analysis by Wunch et al. (2015) suggests that biases of 0.2 % for X_{CO_2} and 0.4 % for X_{CH_4} could exist in the network even though the retrieval algorithm (GGG) has undergone continual improvements designed to reduce such biases.

In this study we quantify bias in X_{CO_2} and X_{CH_4} among the four operational TCCON sites in the United States (US) in 2015. These sites were at (1) the California Institute of Technology (Caltech), Pasadena, California (CA); (2) Armstrong Flight Research Center (AFRC), Edwards, CA; (3) Lamont, Oklahoma (OK); and (4) Park Falls, Wisconsin (WI). Bias quantification was accomplished by comparisons with two mobile EM27/SUN spectrometers (Gisi et al., 2012). A map of the US 2015 TCCON sites is shown in Fig. 3.1. The campaign is described in Sect. 3.2; the data processing and some sensitivity tests are described in Sect. 3.3. Comparisons between the sites are made in Sect. 3.4.

3.2 US TCCON 2015 intercomparability campaign

This campaign involved a comparison of simultaneous side-by-side measurements from two EM27/SUN instruments with TCCON measurements. One EM27/SUN
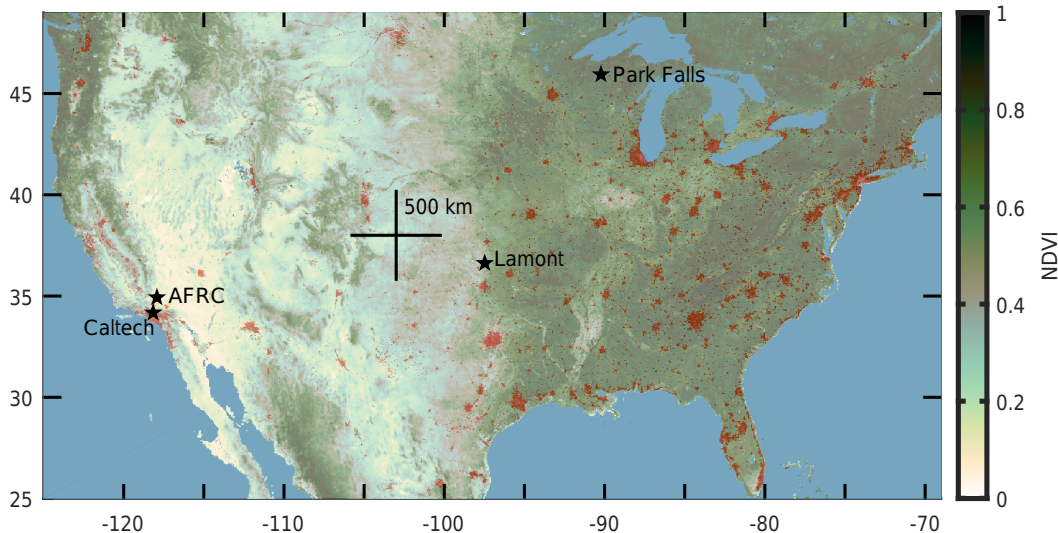
Figure 3.1: Map of the United States with TCCON sites that were active in 2015 labeled. Normalized difference vegetation index (NDVI) from Terra MODIS (Moderate Resolution Imaging Spectrometer; Didan (2015)) and nightlights from VIIS (Visible Infrared Imaging Radiometer Suite) in red are shown for September 2015.

instrument is operated by Caltech and one by Los Alamos National Laboratory (LANL). These instruments have been described in detail elsewhere (Gisi et al., 2012). Briefly, similar to the TCCON spectrometers, they measure direct solar near IR spectra, albeit at a lower resolution ($0.5\,\text{cm}^{-1}$ versus $0.02\,\text{cm}^{-1}$). They include an in-built solar tracker and are small and stable enough to be easily transported. We also designate them as mFTSs for mobile Fourier transform spectrometers (mFTSs) herein. For this study, both mFTSs employed the standard InGaAs (indium gallium arsenide) detector. To reduce the potential for drift between the mFTSs, the campaign was completed within a 5-week period. Based on the lack of drift between the two mFTSs, we conclude that the retrievals from their observations are internally precise over this period so their X_{gas} measurements can be used as transferable comparison products.

The general strategy of the campaign was to visit each of the four TCCON sites shown in Fig. 3.1 and attempt at least 5 days of measurements. Two mFTSs were used so any drift in their measurements would be noticed. In addition to the spectrometers, a traveling Coastal Environment Weather Station with a ZENO® data logger and Setra barometer was used for regular meteorological surface measurements at the AFRC, Lamont, OK, and Park Falls, WI, sites. At Caltech the on-site ZENO® data logger and Setra barometer were used. This type of barometer is used at each of the four US TCCON sites. The Setra sensor has a resolution of $0.1\,\text{hPa}$

and a stated accuracy of 0.3 hPa. A Paroscientific 765-16B Portable Barometric Digiquartz® pressure standard with a stated accuracy of $\pm\,0.08$ hPa or better was used as a traveling pressure standard. The Digiquartz® was compared with each of the on-site barometers. Surface pressure is important to the X_{gas} retrievals because it is used to derive the pressure altitude for the site.

In Table 3.1 we present the dates of the campaign as well as the number of co-incident averaged measurements. Occasionally one mFTS recorded significantly fewer spectra due to unexpected halts during acquisition. This issue was mostly resolved by updating to the latest firmware provided by Bruker™ while at AFRC, but it shows an advantage of having multiple mFTS instruments. Our quality control filters were set after a preliminary look at the data. For this study our filters included 392 ppm $< X_{CO_2} <$ 404, 1.79 ppm $< X_{CH_4} <$ 1.865 ppm, and solar variation < 0.5 % within an interferogram. Prior to the campaign several of the TCCON sites used a mercury manometer as an absolute pressure reference. In the comparisons shown here, the current version of the public TCCON data (R0 for Park Falls, R1 for all others) are used where the surface pressure measurements at all sites are tied to the Digiquartz® (Iraci et al., 2014; Wennberg et al., 2014c,d,b). The mFTSs used the meteorological data from the Caltech on-site station or from the traveling Setra barometer with offsets applied to match the Digiquartz®.

3.2.1 Site characteristics – Caltech

The Caltech site is located in Pasadena, CA (34.136° N, 118.127° W; 240 m a.s.l.), in the California South Coast Air Basin (SoCAB). Pasadena is in an urban environment where there are large diurnal variations of X_{gas} pollutants because of emissions and advection (Wunch et al., 2009, 2016a). Emissions from the basin are estimated to be 167 Tg CO_2 yr^{-1} and 448 ± 91 Gg CH_4 yr^{-1} (Wunch et al., 2016a). Pasadena is located towards the northern end of the basin, which is bounded by mountains. Two additional sides of the basin are also bounded by mountains, and the other side is bounded by the Pacific Ocean. General conditions during the August 2015 campaign were mostly clear skies with some cirrus clouds. We treat two different weeks at Caltech separately to estimate the limits of our methodology. The mean measured daytime X_{H_2O} for both weeks was 3540 ± 840 ppm (1σ).

3.2.2 Site characteristics – AFRC

The AFRC (also called Dryden or Edwards) is located in the Mojave desert at 34.960° N, 117.881° W (700 m a.s.l). It is approximately 100 km north of Caltech

and 100 km east of Bakersfield, CA. AFRC is on a military base, but the surrounding area is much less densely populated than the SoCAB. The area is mostly flat and devoid of vegetation. General conditions here during the campaign were cloud free with daytime surface temperatures of $36.4^{+4.0}_{-13.2}$ °C (95 % confidence intervals, or CI) and a mean measured daytime X_{H_2O} of 2640 ± 250 ppm (1σ).

3.2.3 Site characteristics – Lamont

The Lamont, OK, site is located in an agricultural region that is mostly flat with some rolling hills (36.604° N, 97.486° W; 320 m a.s.l.). It is situated on the Atmospheric Radiation Measurement (ARM) Southern Great Plains (SGP) site. The surrounding area is sparsely populated. During the campaign cumulus clouds were present covering from less than 5 % to approximately 40 % of the sky. The mean measured daytime X_{H_2O} for the campaign week was 5080 ± 890 ppm (1σ).

3.2.4 Site characteristics – Park Falls

The Park Falls, WI, TCCON site has been described in more detail elsewhere (Washenfelder et al., 2006). Briefly, the site is in a sparsely populated but heavily forested region with low topographic relief (45.945° N, 90.273° W; 473 m a.s.l.). Conditions were highly variable, ranging from nearly cloud free to full coverage by stratocumulus clouds. Despite planning more days at this site, the often cloudy conditions contributed to collecting the least amount of data. On 11 September 2015, the TCCON IFS 125HR instrument was realigned as part of routine maintenance. We treat the days before and the day after alignment separately. The mean measured daytime X_{H_2O} was 2480 ± 750 ppm (1σ) for this period.

3.3 Data processing and sensitivity tests

Parker et al. (2015) reported on the comparability of the mFTSs X_{gas} products during the campaign and did not report any drift between them. The modulation efficiency (ME) at maximum optical path difference (MOPD) was reported to be 0.997–0.999 for the LANL mFTS throughout the campaign. The reported ME at MOPD for the Caltech mFTS was lower and more variable, though it is unclear whether or not this variation was due to error in the characterization. A combined mFTS comparison product was created using an unweighted average of the measurements from the two spectrometers based on the recommendations of Parker et al. (2015). This reduces the drift (if any) by one of the instruments. The observed biases of 0.05 ppm X_{CO_2} and -1 ppb X_{CH_4} between the mFTSs were added to the Caltech mFTS products

Table 3.2: Percent changes for T sensitivities at an airmass of 1.5 and a temperature change of $+10\,\mathrm{K}$.

% change	X_{CO_2}			X_{CH_4}		
	TCCON	mFTS	Δ	TCCON	mFTS	Δ
Surf only	−0.004	−0.008	0.005	0.005	−0.043	0.048
Surf-925 hPa	0.026	0.014	0.012	0.039	−0.074	0.113
Surf-850 hPa	0.084	0.066	0.018	0.110	−0.093	0.203
Surf-700 hPa	0.141	0.128	0.013	0.171	−0.177	0.347
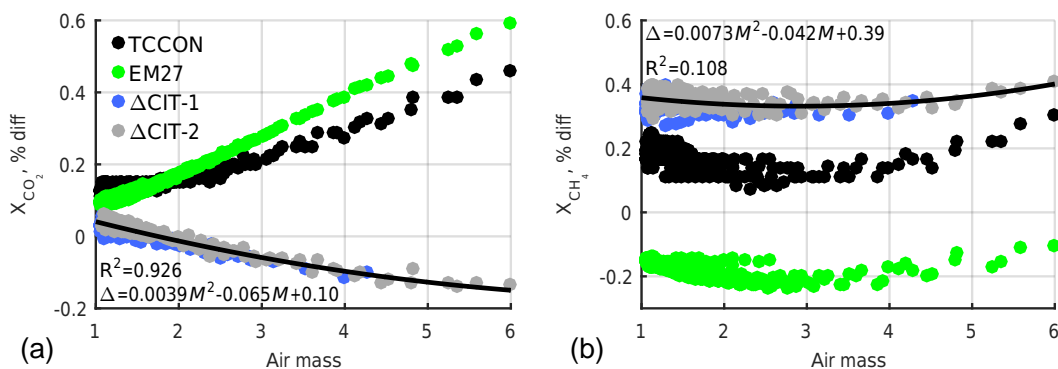
Figure 3.2: Sensitivity of TCCON- and mFTS-retrieved X_{CO_2} **(a)** and X_{CH_4} **(b)** to a $+10\,\mathrm{K}$ change in the planetary boundary layer (surface–$700\,\mathrm{hPa}$) a priori temperature. Green and black points are raw sensitivities, and blue and grey points are their differences during the two times at Caltech. Points are 10 min averages, $n = 397$. For X_{CO_2} the TCCON–EM27 differences are small ($< 0.15\,\%$) but airmass dependent. For X_{CH_4} the TCCON–EM27 differences are larger (0.3–$0.4\,\%$) but with little airmass dependence. The strong airmass dependence for X_{CO_2} suggests that airmass needs to be taken into account for X_{CO_2} surface temperature error adjustments.

before combining with the LANL products.

As a first comparison to the mFTS data, no adjustments to TCCON data are made. These retrievals use the operational GGG2014 algorithm (Wunch et al., 2015). Retrievals with the mFTSs are also performed using GGG2014 with the EGI (EM27/SUN GGG Interferogram processing) suite for automation purposes (Hedelius et al., 2016). Both the high- and low-resolution retrievals used the same model pressure, temperature, altitude, and water profiles (pTz+H_2O) generated from the NCEP/NCAR 2.5° reanalysis product (Kalnay et al., 1996). One profile interpolated to local solar noon is used per day in GGG2014.

Several sensitivity tests have already been performed for TCCON retrievals using GGG2014 (Wunch et al., 2015) as well as for the mFTS retrievals using GGG2014
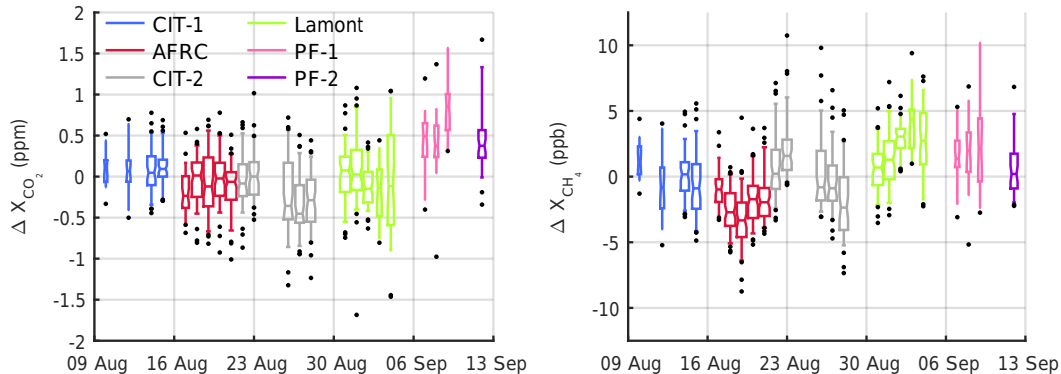
Figure 3.3: Differences between the TCCON and the mFTS products that are unadjusted except overall scale factors have been applied to the mFTS data (X_{CO_2}: 0.9987; X_{CH_4}: 1.0073). Box plots width represents number of comparison points. They are drawn with the center line as median; the center box is the middle 50 % range of data and the whiskers are the 90 % range.

(Hedelius et al., 2016). We repeat some tests for data collected at the Caltech site. To test the sensitivity to the lower tropospheric temperature, a +10 K change is applied for all levels at or below 700 hPa. The results are shown in Fig. 3.2 as a function of airmass (AM). We do not expect the temperature sensitivity to be the same for changes over fewer levels. In Table 3.2 we list changes in X_{CO_2} and X_{CH_4} at an airmass of 1.5 for temperature changes over different levels. Though the temperature bias at the surface is significant, comparison with sonde measurements suggest it decreases rapidly with altitude, making a bias of +10 K all the way to 700 hPa highly unlikely (David Pollard, personal communications, 2016).

3.4 Comparisons

Because of different spectral resolutions between the TCCON instruments ($0.02 \, cm^{-1}$) and the traveling spectrometers ($0.5 \, cm^{-1}$), we anticipate systematic differences in their X_{gas} retrievals (Gisi et al., 2012; Petri et al., 2012). Even in the absence of instrumental problems, spectroscopic inadequacies can cause systematic differences that correlate with T (temperature) errors, surface pressure errors, and solar zenith angle (SZA; Wunch et al. (2011a)). In addition, the instruments have different averaging kernels (AKs) due to differences in spectral resolution. Thus, even though we use the same a priori gas volume mixing ratio and temperature profiles, errors therein will produce differences in the retrieved X_{gas} products (e.g., compare Wunch et al. (2015), and Hedelius et al. (2016)). In this section we consider five reasons why the X_{gas} products between the two instrument types (mFTSs and TCCON) may differ.

First, we consider AM-dependent artifacts that arise due to the effect of spectroscopic errors being resolution dependent. Second, we consider how surface pressure bias could affect retrievals, noting that surface pressure bias should be minimal amongst the current US TCCON data because of standardization to the common traveling Digiquartz® standard. Third, we consider effects of errors in the a priori temperature profile on retrievals from higher- versus lower-resolution spectra. Fourth, we consider the effects of differences in sensitivity from the AKs. Finally, we mention how a non-ideal ILS (instrument line shape) may affect retrievals.

3.4.1 Unadjusted comparisons and AM dependence

The comparisons prior to accounting for differences in temperature sensitivities and AKs are shown as box plots in Fig. 3.3 (Δ = TCCON − mFTS). The mFTS data were scaled to match the TCCON product and center the difference about zero, by dividing by scaling factors of 0.9987 for X_{CO_2} and 1.0073 for X_{CH_4}. These factors were based on the TCCON and mFTS data at all sites and were used in combination with the TCCON to in situ profiles bias correction (Wunch et al., 2015). An additional scaling factor is used because retrievals from lower-resolution spectra are biased compared to higher-resolution spectra due to errors in a priori profiles and spectroscopy (Gisi et al., 2012; Hedelius et al., 2016; Petri et al., 2012). For the box plots, we use the convention that the whiskers are 90 % CI.

AM- or SZA-dependent differences may arise due to spectroscopic errors (Frey et al., 2015). At higher SZAs sunlight passes through a longer atmospheric path, which increases the depth of the measured transmission lines. Spectroscopic errors can lead to bias that varies with SZA, even in clean air sites (Wunch et al., 2011b). Though adding in an AM-dependent correction did not improve the long-term mFTS to TCCON comparison in previous studies (Hedelius et al., 2016), here we noted significant AM dependencies. Air-mass-dependent corrections are accounted for in TCCON data, but these are developed for the high-resolution observations (Wunch et al., 2011a). When we attempted to correct the X_{gas} from the mFTS measurements as a function of SZA, we noted significant influences from local sources and sinks, even at the non-Caltech sites. This complicated the separation of the spurious effects with AM from true atmospheric variation. Additional measurements in areas with little atmospheric variation could aid in accounting for AM artifacts (Klappenbach et al., 2015). In this study, we apply a symmetric basis function to the mFTS products following Eq. (A12) in Wunch et al. (2011a), with coefficients determined empirically to reduce the overall diurnally varying difference data between the mFTS
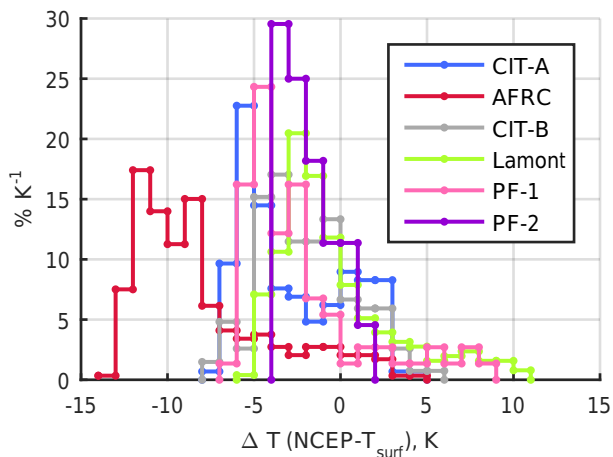
Figure 3.4: Histograms of differences in temperature from those used in the retrievals at the surface (NCEP model) as opposed to the temperature measured at the TCCON sites.

and TCCON retrievals. Further, for estimates of bias we only use data within $\pm 2\,\mathrm{h}$ of local noon so that comparisons are over similar SZAs at all sites. This constrains comparison data to have an AM between 1.05 and 1.85 (site means between 1.10 and 1.46). Recent work has shown residual dependencies on AM that could cause a high bias of $\sim 1\,\mathrm{ppb}\ X_{CH_4}$ between AM 1.10 and 1.46 (Matthaeus Kiel, personal communications, 2017).

3.4.2 Surface pressure and temperature considerations

Surface pressure is used in the calculation of the dry-air column in GGG. It is an input to the retrievals to set the pressure altitudes of each site. A +1 hPa bias in surface pressure leads to average biases of approximately +0.036 % X_{CO_2} and +0.039 % X_{CH_4}, respectively, for $10° < \mathrm{SZA} < 20°$ and +0.034 % X_{CO_2} and +0.049 % X_{CH_4}, respectively, for $70° < \mathrm{SZA} < 80°$ (Wunch et al., 2015). Because pressure measurements are tied to the same Digiquartz® sensor (accuracy of $\pm 0.08\,\mathrm{hPa}$), surface pressure errors are expected to contribute less than 0.01 % to the X_{CO_2} and X_{CH_4} retrievals.

At different temperatures, the distribution of the molecular J states differs, which can affect the relative strengths of overlapping lines from different species. In GGG bands are chosen to be reasonably temperature insensitive by including both high and low J lines to average out temperature sensitivity. In the lower-resolution spectra, lines are less well resolved. When the algorithm attempts to fit the lines, the overall fit may still be good even if fits for individual species are incorrect, but

in compensating ways.

We define a temperature error as the a priori surface interpolated temperature minus the measured site temperature. Histograms of the temperature errors at the different sites are shown in Fig. 3.4. In general, NCEP temperatures are typically cooler than those measured on site. At AFRC the difference is particularly large: the NCEP reanalysis product underestimates the surface temperatures by $\sim 10\,\mathrm{K}$ at times in this desert region for this particular week. We also compared interpolated surface temperatures from the European Centre for Medium-Range Weather Forecasts (ECMWF; $0.125° \times 0.125°$), MERRA-2 (Modern Era Retrospective-Analysis for Research and Applications), GEOS-5 (Goddard Earth Observing System Model), and NAM12 (North American Mesoscale Forecast System, 12 km). Model surface temperature is lower than the AFRC TCCON temperature in all cases, and three of the five models have noon differences of $\sim 10\,\mathrm{K}$. Differences are $\sim 7\,\mathrm{K}$ for GEOS-5 and $\sim 5\,\mathrm{K}$ for NAM12. Though error in the measurement may contribute to part of the T difference, the lower-resolution dynamical models may have a difficult time reproducing surface T at AFRC.

To account for error in the a priori temperature profiles near the surface, we apply two different tests separately. First, we define the temperature error from the surface to $700\,\mathrm{hPa}$ as equal and apply the results described in Sect. 3.3. Second, we apply corrections defining the temperature error separately at each level. The error at each level k was defined as the difference from the NCEP profile potential temperature $\theta_{\mathrm{NCEP,k}} - \theta_{\mathrm{measured,s}}$ (where "s" stands for surface) when $\theta_{\mathrm{measured,s}} > \theta_{\mathrm{NCEP,k}}$. Thus potential temperatures aloft are always greater than or equal to $\theta_{\mathrm{measured,s}}$. Both corrections reduce the diurnal trend of the $\Delta X_{\mathrm{CH_4}}$ and $\Delta X_{\mathrm{CO_2}}$ during the middle hours of the day but do not significantly alter the comparisons in the late afternoon. True temperature profiles are likely different from the NCEP noon profiles. Future releases of GGG will apply a post facto temperature correction for the lowest 3 km based on temperature-dependent water lines (Toon et al., 2016b). For future studies, we recommend adding dedicated sondes as part of the instrument suite for these field campaigns.

3.4.3 Averaging kernel differences

AKs (Fig. 3.5) are different for the 0.02 and $0.5\,\mathrm{cm}^{-1}$ instruments. We apply Eq. (A13) from Wunch et al. (2011b) to the TCCON X_{gas} (c) product to reduce the smoothing error (the contribution of different AKs). We denote the mFTS by
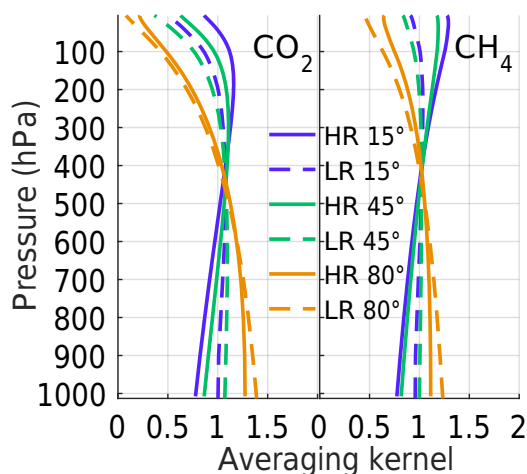
Figure 3.5: A comparison of the averaging kernels at three different SZAs for the higher-resolution (HR) and lower-resolution (LR) instruments. The LR instruments are more sensitive to changes at the surface but less sensitive to changes in the stratosphere.

subscript 1, the TCCON by subscript 2, and the TCCON product adjusted to reduce the smoothing error of the mFTS AKs (AKs) as $1\leftarrow2$.

$$\hat{c}_{1\leftarrow2} = c_{\mathrm{a}} + (\gamma_2 - 1) \sum_j h_j a_{1j} x_{\mathrm{a}j} \tag{3.1}$$

Aˆrepresents a retrieved quantity, the subscript "a" denotes the prior, $\vec{h}$ is the pressure weighting function described by Connor et al. (2008), $\vec{a}$ is the column AK, $\vec{x}$ is the DMF a priori profile, and γ is the overall scaling factor applied to the TCCON a priori profile to obtain the retrieved X_{gas}. Both the TCCON and the mFTS use the same a priori profiles. In Eq. (1), the TCCON profile $\gamma\vec{x}_{\mathrm{a}}$ is treated as an approximation to the true atmospheric DMF profile (compare Eq. 3 from Rodgers and Connor, 2003). This is a better approximation in a sparsely populated location such as Lamont than at Caltech where local anthropogenic emissions strongly influence the atmosphere. However, overall the application of Eq. (1) only makes differences of $0.00^{+0.04}_{-0.04}$ ppm and $0.01^{+0.17}_{-0.07}$ ppb (95 % CI) for $X_{\mathrm{CO_2}}$ and $X_{\mathrm{CH_4}}$ in this dataset.

GGG2014 a priori profiles do not take into account local anthropogenic emissions at the surface. In Fig. 3.6 we plot the in situ DMFs of CO_2 and CH_4 measured near the surface throughout the day as well as those from the a priori profiles used in the GGG2014 retrievals at the Caltech site. The in situ measurements were recorded using a Picarro cavity ring down spectrometer, with standardization by comparison

to three NOAA (National Oceanic and Atmospheric Administration) standards every 23 h. Given the intense local emissions, the measured in situ DMFs are significantly larger than the a priori near the surface. Using the same assumptions as Hedelius et al. (2016), the X_{gas} retrievals for two instruments in a polluted environment where the true and a priori profiles differ only at the surface are related by

$$\hat{c}_1 = \frac{a_{1,s}}{a_{2,s}} [\hat{c}_2 - c_a] + c_a. \tag{3.2}$$

Note the error term has been omitted. The subscript s represents the surface. These assumptions are better for X_{CO_2} than for X_{CH_4} as changes in tropopause height can also make the a priori methane profile significantly different from the true profile (Saad et al., 2014). Over this time at Caltech, X_{HF} averaged ~ 50 ppt and γ^{HF} averaged ~ 0.87, suggesting an a priori tropopause height that is too low. Using the β value from Saad et al. (2014) we estimate a 13 % difference in γ^{HF} due to tropopause height would cause about a 0.24 % change in γ^{CH_4} (~ 4 ppb), which is large enough that Eq. (3.2) is not valid for X_{CH_4}. We apply Eq. (3.2) to the X_{CO_2} TCCON retrievals at the Caltech TCCON site, which leads to an adjustment of $0.22^{+0.54}_{-0.35}$ ppm (95% CI).

3.4.4 Effects of a non-ideal ILS

Imperfections in the ILS due to misalignment of the TCCON FTSs can also cause site biases. At the sites described in this study, weekly internal lamp measurements of the internal, calibrated HCl cells (Hase et al., 2013) are collected from the 125HR instruments. We use LINEFIT 14.5 (Hase et al., 1999) software on HCl lines from monthly-averaged spectra to characterize the ILS. For Park Falls spectra were averaged before and after realignment. In Fig. 3.7 are the ME and phase error (PE) with OPD. An ME not equal to 1 can indicate instrument misalignment, which may be from shear, angular, or defocus misalignment.

Effects of different types of misalignment on ME are not independent (Toon et al., 2016a). However, parameterizing changes in ME with OPD can be used to assess effects on X_{gas} retrievals (Griffith and Macatangay, 2010; Velazco et al., 2016; Wunch et al., 2011a, 2015). These previous studies have found that each 1 % increase in ME at MOPD leads to a decrease on the order of 0.04 % in X_{CO_2}, though the change does vary with SZA. For X_{CH_4}, there is a decrease on the order of 0.03–0.05 % for a 1 % increase in ME at MOPD. The cause of the change in ME
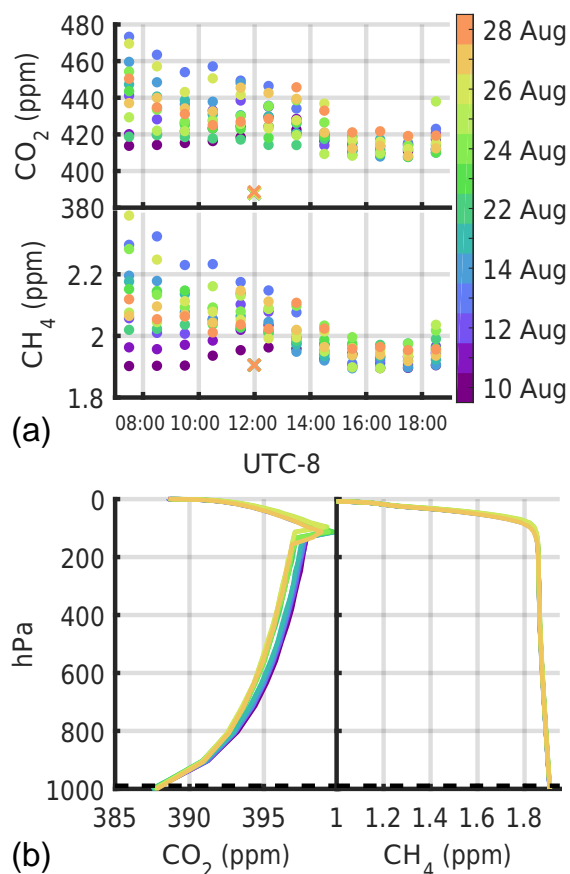
Figure 3.6: **(a)** Diurnal variation of in situ DMFs measured near the surface at Caltech on the days of TCCON to mFTS comparisons. A priori surface values are marked by an "x" at noon. **(b)** GGG2014 a priori profiles used in the retrievals, with lower CO_2 and CH_4 than was measured near the surface. Surface pressure is indicated by the dashed line.

with OPD can, however, also significantly influence results. For example, Wunch et al. (2015) noted significantly different results for the same change in ME when the cause is shear versus angular misalignment.

We estimate biases based on ME at MOPD values alone, compared with AFRC. Based on the LINEFIT analysis of the lamp spectra, we would expect a low X_{CO_2} bias of 0.02 % for Caltech, a high bias of 0.05 % for Lamont, and a high bias of 0.09 % for Park Falls (prior to realignment). The results of our study are not consistent with this expectation. Only Park Falls is consistently in the right direction with a bias of ∼ 0.18 % before realignment. After realignment, Park Falls X_{CO_2} was more in line with the other spectrometers, although based on the ME at MOPD results alone there should have been a change in the opposite direction. The Park Falls ILS was much more symmetrical after realignment, as seen by the PE curve in the lower
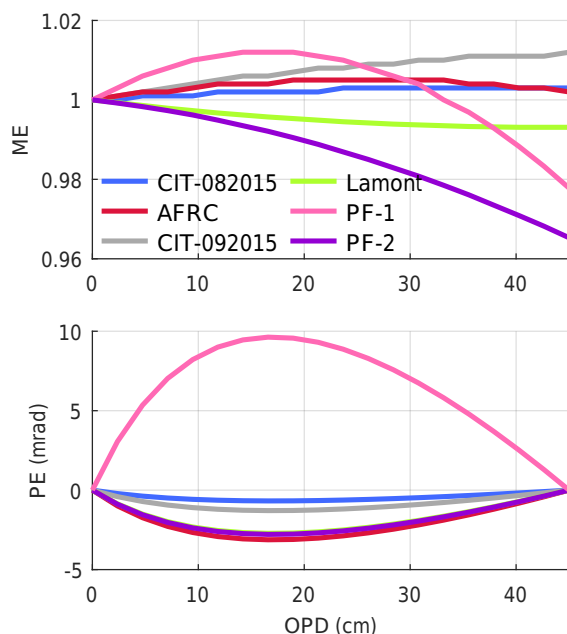
Figure 3.7: Modulation efficiency and phase error for each of the 125HR instruments describe the ILS. Results are calculated from HCl lines using LINEFIT 14.5 on monthly averages of internal lamp spectra. For Caltech, two different months are shown and Park Falls-1 corresponds to August 2015 and Park Falls-2 corresponds to October 2015.

panel of Fig. 3.7 being much closer to zero. For X_{CH_4}, both Park Falls and Lamont are biased in the expected direction from Armstrong, and the Park Falls-1 bias is $\sim 0.25\,\%$. However, the Lamont bias is greater than expected from the single value parameterization. A more complex parameterization of the ILS effect on X_{gas} (e.g., using the full function of ME with OPD, accounting for SZA dependence) might reduce the expected versus observed mismatch.

The X_{air} parameter from GGG can be used as a diagnostic for large misalignments, timing, and surface pressure errors. X_{air} is calculated by dividing the sum of all non-water molecules based on the surface pressure by the retrieved column of dry air based on column O_2. X_{air} should be close to 1.0 and not vary, though empirically it is approximately 2% lower due to spectroscopic errors for oxygen (Washenfelder et al., 2006). Wunch et al. (2015) showed an increase of about 0.3 % in X_{air} for a 1% increase in ME at MOPD due to shear misalignment, and the change due to angular misalignment was $< 0.03\%$. In Fig. 3.8 X_{air} is shown for all the sites. At Park Falls X_{air} was approximately 0.979 before and 0.983 after alignment, which could correspond to an ME increase of about 0.013 at MOPD from shear realignment. LINEFIT results actually show a decrease in ME at MOPD after September 11
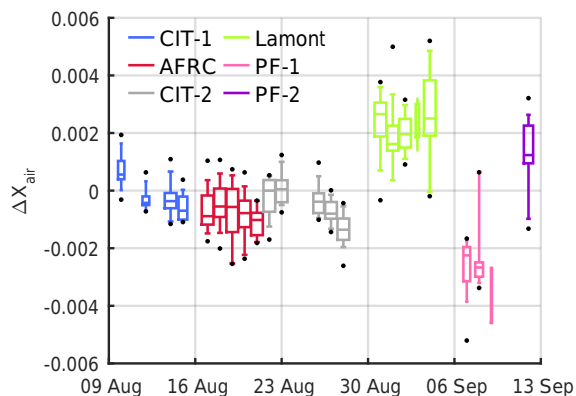
Figure 3.8: TCCON X_{air} compared with mFTS X_{air} within ±2 h of local noon. The differences are scaled by 1.001 to be centered about zero. X_{air} can be used as a diagnostic for misalignments, timing, or surface pressure errors.

2015, but X_{CO_2} and X_{CH_4} decreased. Based on X_{air}, X_{CO_2} was expected to change by ~ 0.2 ppm (compared with ~ 0.08 ppm) and X_{CH_4} was expected to change by 0.7–1.2 ppb (compared with ~ 1.5 ppb). Residual differences may indicate measurement uncertainties.

3.4.5 Truncated 125HR interferograms comparisons

Retrievals from the 125HR and mFTS instruments are inherently different due to the differences in resolution. By truncating the longer 125HR interferograms to the same length as those collected from the mFTS, similar-resolution spectra are obtained. This likely eliminates most discrepancies between the different types of measurements, except for some residual instrumental imperfections such as instrument misalignment or ghosts. Truncation also reduces the effects of ME variations due to the smaller MOPD. Truncation has been performed in past studies comparing retrieved X_{gas} from different-resolution spectrometers (Gisi et al., 2012; Hedelius et al., 2016; Petri et al., 2012). This test provides little new information if truncation changed all retrieved DMFs in a uniform manner. However, past studies showed truncation does not necessarily affect all results the same way, which makes this test imperative in diagnosing potential causes of differences. It helps in determining which biases likely arise from instrumental issues and which arise from other issues such as errors in the forward model (e.g., from temperature biases at different locations).

The results of the truncation test are shown Fig. 3.9, and changes are most easily seen from the unscaled (open) points. The sign of the change for X_{CO_2} is inconsistent for
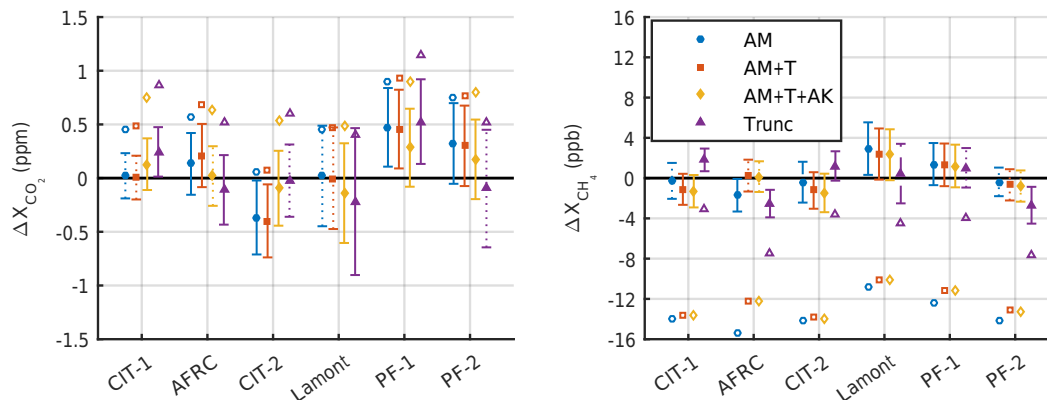
Figure 3.9: Medians and standard deviations of the TCCON data compared to the mFTS product after various adjustments. Line style represents the significance of the difference of the group median from the median of all data by the Kruskal–Wallis test ($p < 0.05$ –, $p < 0.2$ - -, otherwise . . .). Legend entries indicate what adjustments were applied to the data to make measurements from the different instrument types more comparable. Open symbols did not have a scaling factor applied to center about zero. AM is airmass adjustment, T is temperature error adjustment, and AK is averaging kernel adjustment.

Table 3.3: Mean differences pre- and post-adjustment for ± 2 h of local noon.

X_{CO_2} (ppm)	AM	AM+T	AM+T+ AK	Trunc
$\frac{1}{n} \sum |Md|$	0.17	0.18	0.11	0.14
$\frac{1}{n} \sum |\sigma|$	0.34	0.34	0.34	0.42
X_{CH_4} (ppb)				
$\frac{1}{n} \sum |Md|$	1.1	1.1	1.2	1.7
$\frac{1}{n} \sum |\sigma|$	1.9	1.8	1.8	1.8

the different sites. Previous studies also noted changes that were negative (Petri et al., 2012), positive (Gisi et al., 2012), or both (but with a preference towards negative; Hedelius et al. (2016)) when using lower-resolution spectra. For lower-resolution spectra X_{CH_4} increases, in agreement with previous studies (Hedelius et al., 2016; Petri et al., 2012).

3.4.6 Biases to overall median

The medians and standard deviations for data before and after considering differences in AKs, and surface temperature are shown in Fig. 3.9. Though we have attempted to reduce artificial diurnal variation between the different instruments with the AM correction, there may still be some residual dependence with SZA. To reduce this

dependence, which is larger at higher SZAs, only data within ±2 h of local noon are used. We use the Kruskal–Wallis one-way analysis of variance test, which assumes ordinal but not necessarily normally distributed data (Kruskal and Wallis, 1952), and compare data from each site to the median of data from all sites. The null hypothesis of this test is the medians do not significantly differ. Line styles indicate the degree of significance by the Kruskal–Wallis tests.

Pooled differences are listed in Table 3.3 for different adjustments. These are represented by the averages of the group median differences, the overall median, and the average standard deviations. Park Falls TCCON data prior to realignment of the spectrometer are omitted. The sum of the median differences decreases for X_{CO_2} after adjustments. However, this is not true of X_{CH_4}, which increases in variability after adjustment. Despite this overall increase for X_{CH_4}, these adjustments better reflect the intercomparability of the sites rather than the intercomparability of measurements from differing instruments. From Table 3.3, we estimate the average biases of all sites compared to the median to be 0.03 % X_{CO_2} and 0.08 % X_{CH_4}.

3.4.7 Confidence intervals of the pairwise differences

We use the Critchlow–Fligner method to estimate simultaneous CI for the differences between all pairs of sites (Hollander et al., 2014). The Critchlow–Fligner test is nonparametric so it is less sensitive to outliers and few assumptions are needed about the distribution of the underlying population of data. We use $\alpha = 0.05$ to obtain 95 % confidence intervals of the differences between sites. Results are presented in Fig. 3.10 in order of decreasing median difference and separated by gas and adjustments. At the bottom are the ordering of the sites.

This comparison suggests for X_{CO_2} is lowest for Lamont and highest for Park Falls-1 in both cases. There is a difference between the two different weeks at Caltech for unknown reasons. The largest difference within a 95 % CI is 0.6 ppm between Park Falls and Lamont; this difference is 1.0 ppm for the truncation test. However, most mid-range values are ∼ 0.2 to 0.3 ppm.

For X_{CH_4}, there was more of a change in site order between the two cases. For the truncation comparison the differences are even greater than AM+T+AK comparison as indicated in Table 3.3. The largest difference within a 95 % CI is 4 ppb between Lamont and Caltech. For the truncation test the largest difference is between Armstrong and Caltech and is greater than 5 ppb. Mid-range values are 2–3 ppb.
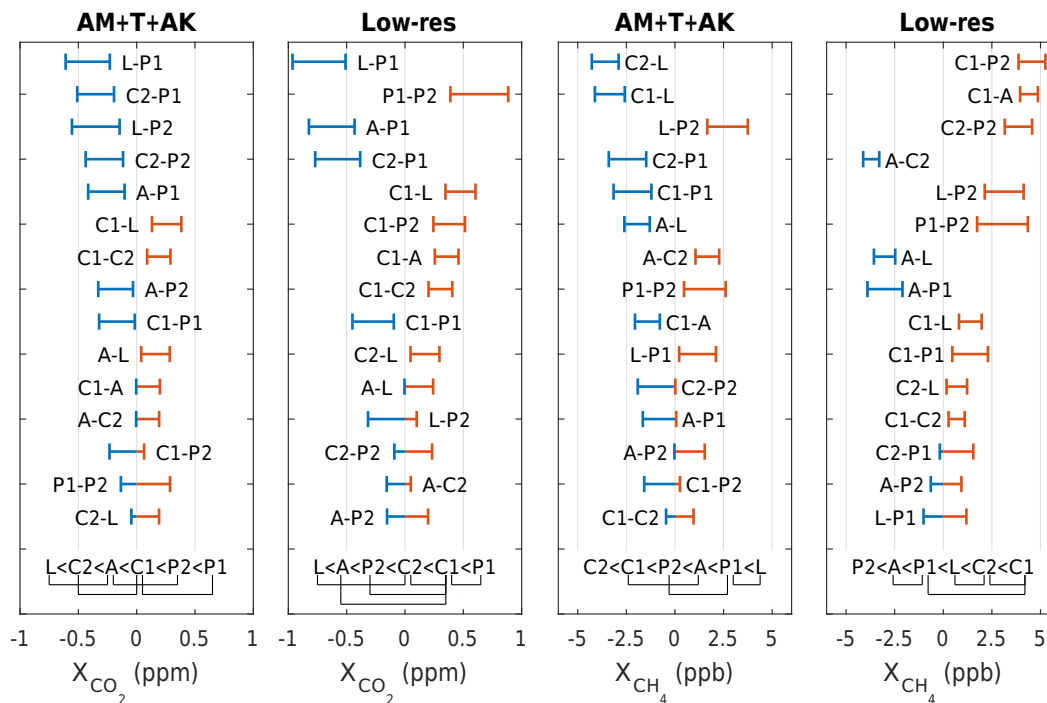
Figure 3.10: Pairwise 95 % CI of differences between sites. Differences for data within ±2 h local noon. Comparisons are ranked in order of decreasing mean difference. For each species, plots are shown for (1) corrections for airmass, differences in temperature sensitivity errors defining temperature errors layer by layer, and a reduction of the smoothing error from different averaging kernels; (2) differences by comparing results from 125HR spectra with lowered resolutions. At the bottom are the site orderings. Lines between indicate when the pairwise difference is first more than 0.

3.5 Conclusions

We estimate the range of statistically significant site-to-site bias amongst the sites as < 0.3 ppm for X_{CO_2} and < 3 ppb for X_{CH_4}. These were determined by comparing TCCON data with simultaneously collected data from co-located portable spectrometers, which we have assumed to be internally precise over the duration of the campaign. This assumption is supported by standard deviations of only 0.15 ppm for X_{CO_2} and 1 ppb for X_{CH_4} for the 10 min averaged differences between the two mFTS instruments over the campaign. Five reasons X_{gas} could differ among instruments were considered: (1) differences in averaging kernels, (2) differences in spurious airmass dependence from spectroscopy errors, (3) the a priori profile (e.g., temperature profile), (4) error in the measured surface pressure, and (5) instrument misalignments. Of these, the last four can cause site-to-site biases in the TCCON, and empirical adjustments to make the mFTS and TCCON datasets more compara-

ble were made to the first three. When the 125HR interferograms were truncated so the spectra would be the same resolution as the mFTSs, differences from the first three inherently go away.

As the spectroscopy is improved, the data should have smaller AM-dependent artifacts, though for now an empirical correction is used for the TCCON (Wunch et al., 2011a). Updates to the retrieval algorithm to include line mixing may also make the AM dependence more predictable (Hartmann et al., 2009). The corrections based on T errors described in Sect. 3.4.2 are for the differences in sensitivity to T error between the mFTS and TCCON instruments and not for the different T errors at each TCCON site. Large temperature errors of $+10\,\mathrm{K}$ from the surface through $850\,\mathrm{hPa}$ could cause errors of $0.08\,\%$ in X_{CO_2} and $0.11\,\%$ in X_{CH_4} at an airmass of 1.5. Biases due to a non-ideal ILS will be reduced in future versions of the GGG retrieval algorithm. Biases in surface pressure data can cause site biases but are expected be less than $0.01\,\%$ in the current data revisions because surface pressure data were standardized to the same traveling standard. We recommend regular ($\sim$ annual, depending on the pressure sensor accuracy) comparisons of meteorological pressure measured by on-site barometers with a universal standard for those making similar column measurements.

Remaining differences are most likely from a combination of other errors mentioned by Wunch et al. (2015), such as instrumental misalignment and Doppler shifting of solar lines with respect to telluric lines. Some of these uncertainties will be reduced in the next version of GGG. Other remaining differences may be due in part to noise. Sufficiently large sample sizes should have helped reduce bias from noise, and the 15 min running standard deviations for TCCON were $0.11\,\%$ X_{CO_2} and $0.13\,\%$ X_{CH_4}. Apparent differences between the weeks at Caltech suggest we are near the precision limit of our current methodology. Though we reduced the contributions of ΔX_{gas} from different instruments, there may remain additional contributions because of differences in resolution (Petri et al., 2012).

United States TCCON site-to-site biases measured herein are within the $2\sigma X_{CO_2}$ and X_{CH_4} uncertainties stated by Wunch et al. (2010). We suggest repeating this study comparing results from traveling spectrometers with those from the stationary TCCON sites, especially when aircraft and air-core data are not available to check for bias. Ideally repeat campaigns will include multiple traveling mFTS instruments. Others may even consider taking three mFTS instruments, so if there is a change from one it would be noticeable by comparing with the other two. When collocated, three

or more EM27/SUN instruments can easily be operated by just one or two people. Multiple instruments also provide backup in case problems arise with one and can increase the signal to noise ratio. As a backup strategy, one traveling mFTS can be taken in the field and compared with an mFTS instrument left in a fixed location before and after the campaign. This second strategy is acceptable when there are no instrumental issues, or if it is known when and how issues affect X_{gas} measurements. This type of campaign can be repeated every few years, or with different sites (e.g., Sha et al. (2016)), or with different gases that can be measured with an extended-band InGaAs detector with spectral filters (Hase et al., 2016). Similar studies should, however, also consider the current precision limits of these comparisons on various timescales. We hope others will improve on our methodology to estimate inter-site biases using portable spectrometers. A sufficient number of aircraft profiles may also aide in determining intercomparability. The NASA Atmospheric Tomography Mission (ATom), for example, will conduct global flights summer 2016 through spring 2018 and will include profile measurements of CO_2, CH_4, CO, and N_2O over many of the TCCON sites (`https://espo.nasa.gov/home/atom`). Data from ATom can be used to reevaluate TCCON uncertainties in the next version of GGG.

Data availability

TCCON data are currently hosted on the CDIAC and will also be available on the Caltech library data archive by the end of the year (Iraci et al., 2014; Wennberg et al., 2014c,d,b). Mobile FTS data are available upon request to the authors.

Competing interests

The authors declare that they have no conflict of interest.

Edited by: J. Notholt

Reviewed by: F. Hase and one anonymous referee

Chapter 4

EMISSIONS AND TOPOGRAPHIC EFFECTS ON COLUMN CO_2 (X_{CO_2}) VARIATIONS, WITH A FOCUS ON THE SOUTHERN CALIFORNIA MEGACITY

Keypoints

- In the SoCAB, 20–36% of spatial variance in X_{CO_2} is explained by topography on scales $< \sim 10$ km.

- In Pasadena, X_{CO_2} is enhanced by $2.3 \pm 1.2\,(1\sigma)$ ppm above background levels, at 1300 (UTC-8) with seasonal variation.

- The SoCAB X_{CO_2} enhancement is in agreement for three different observation sets (TCCON, GOSAT, and OCO-2).

Abstract

Within the California South Coast Air Basin (SoCAB), X_{CO_2} varies significantly due to atmospheric dynamics and the non-uniform distribution of sources. X_{CO_2} measurements within the basin have seasonal variation compared to the "background" due primarily to dynamics, or the origins of air masses coming into the basin. We observe basin–background differences that are in close agreement for 3 observing systems: TCCON 2.3 ± 1.2 ppm, OCO-2 2.4 ± 1.5 ppm, and GOSAT 2.4 ± 1.6 ppm (errors are 1σ). We further observe persistent significant differences (~ 0.9 ppm) in X_{CO_2} between two TCCON sites located only 9 km apart within the SoCAB. We estimate 20% ($\pm 1\sigma$ CI: 0%, 58%) of the variance is explained by a difference in elevation using a full physics and emissions model, and 36% ($\pm 1\sigma$ CI: 10%, 101%) using a simple, fixed mixed layer model. This effect arises in the presence of a sharp gradient in CO_2 (or another species) between the mixed layer (ML) and free

troposphere. Column differences between nearby locations arise when the change in elevation is greater than the change in ML height. This affects the fraction of atmosphere that is in the ML above each site. We show that such topographic effects produce significant variation in X_{CO_2} across the SoCAB as well.

4.1 Introduction

Carbon dioxide (CO_2) is the single most important human influenced (anthropogenic) greenhouse gas (GHG) (Myhre et al., 2013). Atmospheric CO_2 concentrations have increased from 278 ± 2 ppm in 1750 (Etheridge et al., 1996) to more than 400 ppm today (`https://www.esrl.noaa.gov/gmd/ccgg/trends/global.html`). The change in radiative forcing (RF) over the industrial era for all well-mixed anthropogenic greenhouse gases (WMGHGs) is 2.83 ± 0.29 Wm^{-2}; and the change in CO_2 alone accounts for 1.82 ± 0.19 Wm^{-2} (Myhre et al., 2013). Changes in radiative forcing due to CO_2 increases have been directly observed (Feldman et al., 2015).

A significant fraction of anthropogenic CO_2 emissions are a result of activities within urban areas. Central estimates of CO_2 emissions related with urban final energy use are 76 % globally and 86 % of the total emissions in North America (Seto and Dhakal, 2014). Because some CO_2 emissions related with urban use are from outside urban areas (e.g. due to imported electricity), primary or direct CO_2 emissions from urban areas are lower (30–56 %, central estimate 43 %). These fractions are somewhat disproportionate as urban areas house 54 % of the world's population (United Nations, 2014), and cover only ~ 0.5 % of ice-free terrestrial land (Schneider et al., 2009).

Large urban agglomerations, or megacities, are particularly large anthropogenic emitters, with the 50 largest cities globally emitting more CO_2 equivalent than any country besides the United States and China (Hoornweg et al., 2010). One of these megacities is the greater Los Angeles (LA) area which fills much of the South Coast Air Basin (SoCAB) in California (CA). The SoCAB has ~ 17 million inhabitants sprawled over 4 counties (Los Angeles, Orange, San Bernardino, and Riverside) and more than 160 cities. SoCAB emissions have been estimated to be on order of 167 Tg CO_2 yr^{-1} (Wunch et al., 2016a) which is ~ 3.2 % of fossil fuel and cement production CO_2 emissions from the United States or approximately 0.4 % of the total global anthropogenic CO_2 emissions.

The SoCAB is a favorable test bed location for quantifying CO_2 emissions by

remote sensing because of the unique wealth of available data. Los Angeles was chosen as one of two cities (besides Paris) in a pilot program to study megacity emissions (Duren and Miller, 2012); Sao Paulo, Brazil has since been chosen as a third city (`https://megacities.jpl.nasa.gov/portal/`). There have been several previous studies that have analyzed CO_2 activity within the SoCAB. Affek et al. (2007) used isotopic measurements of CO_2 from flask samples to analyze the seasonality and sources of air in Pasadena (~ 14 km NE of downtown LA). Newman, et al. [2008, 2013, 2016] have studied CO_2 mixing ratios and isotopic composition since 1972 (primarily in Pasadena), and have used both isotopologues and air composition to partition sources of CO_2. Djuricin et al. (2010) used isotope analysis on air samples collected ~ 58 km S of LA to apportion anthropogenic and biogenic CO_2 sources. Brioude et al. (2013) used aircraft measurements of CO_2 with the Weather Research and Forecasting Model (WRF) to estimate basin fluxes. Wunch et al. (2009) studied diurnal patterns of column averaged CO_2 observed by ground-based remote sensing at a TCCON (Total Carbon Column Observing Network) site. Kort et al. (2012) studied the average column enhancement in the SoCAB using satellite observations. Feng et al. (2016) used a high resolution (1.3 km) WRF model to study CO_2 patterns across the basin. Finally, Verhulst et al. (2016) described patterns of CO_2 variation observed using the SoCAB megacity tower network.

In addition to the atmospheric measurements of CO_2 just described, there are several detailed bottom up inventories that cover the SoCAB. Under California's Health and Safety Code (H&SC) 39607.4, the California Air Resources Board (CARB) is responsible to report California's GHG inventory. CARB combines various datasets on reported petroleum product use throughout the state to create GHG emission estimates. Other CO_2 emission products that cover the SoCAB are available, including the Hestia-LA Project™ by Arizona State University. The Hestia project quantifies fossil fuel CO_2 (FFCO$_2$) emitting activity at the building and street level (Gurney et al., 2012), and is the higher spatial-resolution successor to the Vulcan product for cities where it is available. A map of Hestia-LA v. 1.0 emissions is shown in Fig. 4.1, along with maps of nightlights and topography.

The SoCAB is roughly 140 km $\times 50$ km and is surrounded by mountains on three sides and the Pacific Ocean on the fourth. Prevailing midday winds at the surface are on-shore caused by the sea breeze and heated-slope mountain-valley flows, with return winds aloft (Shultz and Warner, 1981). Typical wind speeds are maximum
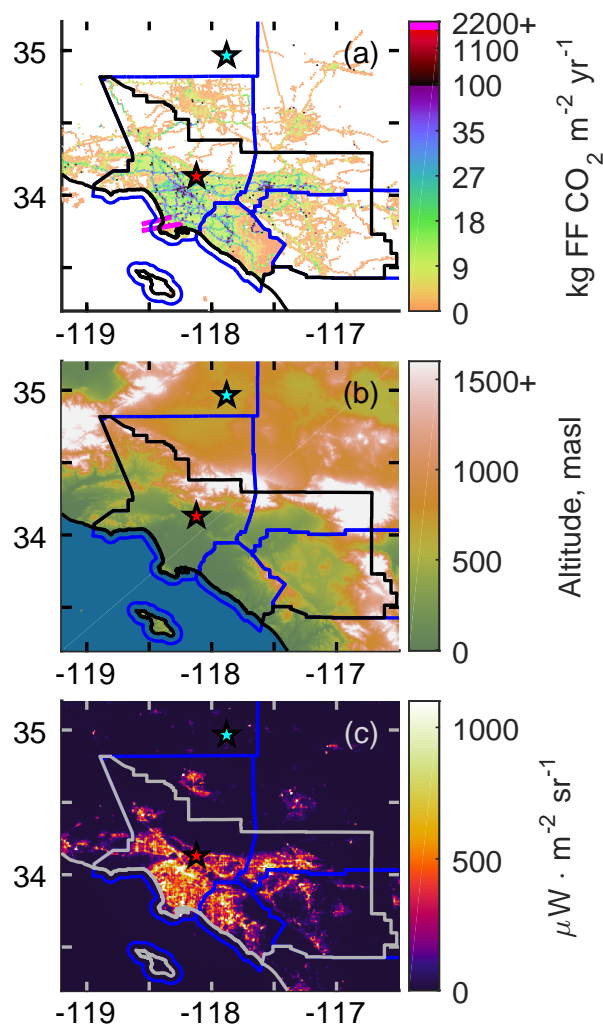
Figure 4.1: Maps of the SoCAB. The SoCAB boundary is shown in black (or gray). County boundaries are in blue. Red and cyan stars are for the Caltech and AFRC TCCON sites respectively. (a) Annually averaged gridded Hestia version 1.0, 2012 emissions. The two magenta lines are shown to draw the eye from the ocean to the two boxes with largest $FFCO_2$ emissions ($2200+ \, \text{kg} \, \text{m}^{-2} \, \text{yr}^{-1}$), otherwise the boxes are too small to distinguish from surroundings. (b) Terrain of the area from the ASTER GDEM. (c) Nightlights intensities from January 2015 as measured by the Suomi NPP satellite.

$\sim$5–10 m s^{-1}, which leads to polluted air accumulating in the north and eastern parts of the basin. Local pollution enhancements primarily stay in the mixed layer (ML), which is the layer of the atmosphere near the surface that responds to surface forcings on the timescale of about an hour or less (for a discussion of lidar ML measurements in Pasadena, see Ware et al. (2016)). Pollution continues to accumulate until the

ML height increases enough, and the sea-breeze front travels far enough for aged air to be pushed out over the mountains or vented through mountain passes. These effects cause CO_2 gradients within the basin, large diurnal changes of the column averaged dry-air mole fraction (DMF) CO_2 (X_{CO_2}) inland (2–8 ppm, (Wunch et al., 2009)), and consistent mid-day X_{CO_2} enhancements compared to the nearby rural desert region ($3.2 \pm 1.5\,(1\sigma)$ ppm, (Kort et al., 2012)). All of the enhancement in X_{CO_2} is expected to occur because of a CO_2 enhanced ML and is attributed almost completely to anthropogenic emissions (Kort et al., 2013; Newman et al., 2013).

Column-averaged DMFs (e.g. X_{CO_2}) have been suggested to be important tools for Measurement, Reporting, and Verifying (MRV) of emissions from urban areas (Kort et al., 2012; McKain et al., 2012; Hase et al., 2015; Wunch et al., 2016a). X_{CO_2} is measured long-term with remote sensing instruments (e.g. by satellites or ground-based solar viewing spectrometers). It is defined as (Wunch et al., 2011a)

$$X_{CO_2} = \frac{\text{column}_{CO_2}}{\text{column}_{\text{dry air}}}. \tag{4.1}$$

Because X_{CO_2} is dominated by the free troposphere, column measurements are less sensitive to local CO_2 concentrations than in situ measurements, but more sensitive to regional levels. Remote sensing of X_{CO_2} from space-borne instruments allows for observations where there are no ground-based X_{CO_2} measurements.

MRV by column DMFs can be used to evaluate progress towards emission goals. Generally emission goals are stated as percent decreases, so only relative (rather than absolute) changes in emissions over the observation period are needed. California, for example, has a goal to cut emissions to 1990 levels by 2020 and to 80 % below 1990 levels by 2050 (Pavley and Nunez, 2006). The city of Los Angeles has a goal to cut emissions to 35 % below 1990 levels by 2030 (Villaraigosa, 2007). In this study, we are interested in assessing the potential for using X_{CO_2} for MRV in a city with well-studied emissions. In particular, we would like to understand contributions to X_{CO_2} variations over small areas (a few km), and across the basin.

Non-emissions related changes (e.g. from relative ML fractions) over small scales may be misinterpreted as a flux, which could bias results. This is important to recognize because X_{CO_2} can vary significantly in the SoCAB. As an example, assume 2 sites 9 km apart have a consistent 0.9 ppm difference in X_{CO_2}, and a surface pressure of about 980 hPa. This is approximately what the mean difference is between Caltech and JPL. This is a $\sim 0.28\,\text{mol m}^{-2}$ difference, or assuming an equal gradient along the full path between each sites $\sim 35\,\mu\text{mol m}^{-2}\,\text{m}^{-1}$. With

a horizontal wind speed of $5\,\mathrm{m\,s^{-1}}$ and no vertical mixing, this simple difference would require a $170\,\mu\mathrm{mol}\,CO_2\,\mathrm{m^{-2}\,s^{-1}}$ uptake or emission flux depending on wind direction—about 9× the Hestia-LA flux at the Pasadena site (Feng et al., 2016) or about 7× the largest diel gross ecosystem exchange from a temperate forest (Wehr et al., 2016).

If all of the difference is attributed to a surface flux in the example above, the result is unreasonably large. We explore other reasons for inner-basin X_{CO_2} variance. In particular, we consider the effect of non-uniform weighting of the ML (e.g. by local topography changes) on X_{CO_2} variations within the region due to a strong gradient between the ML and free troposphere. Here, the strong gradient is from emissions, but variation due to topography could also occur in an area with high uptake, such as a productive forest. We evaluate whether X_{CO_2} variability can be explained by different factors using models that include the underlying emissions and simulation of the atmospheric transport. We also determine how X_{CO_2} within the basin compares to nearby background levels.

In Sect. 4.2 we describe the datasets and the models. In Sect. 4.3 we examine how the X_{CO_2} enhancement within the basin has varied with time. In Sect. 4.4 we describe reasons for X_{CO_2} variations within the SoCAB. We conclude in Sect. 4.5 with our main findings.

4.2   Datasets

We use 3 observational datasets (Sect. 4.2.1–4.2.3) as well as 3 simulated X_{CO_2} products (Sect. 4.2.4–4.2.5). These are described in more detail below.

4.2.1   TCCON

Ground based measurements of X_{CO_2} were made at three TCCON sites (Wunch et al., 2011a). The California Institute of Technology (Caltech) site in Pasadena, California (34.136° N, 118.127° W, 240 m a.s.l.) is located within the SoCAB. The Caltech site has been operational since September 2012 (Wennberg et al., 2014c). TCCON measurements at the Jet Propulsion Laboratory (JPL), were concurrent with Caltech TCCON measurements from January–June 2013 (Wennberg et al., 2014a). This site is also within the SoCAB (34.202° N, 118.175° W, 390 m a.s.l.) and less than 9 km from Caltech. In July 2013, the former JPL instrument was moved outside the SoCAB 95 km away to Armstrong Flight Research Center (AFRC) (34.960° N, 117.881° W, 700 m a.s.l.). This instrument has remained at AFRC since July 2013 (Iraci et al., 2014). Retrievals from the measurements at all three sites use the

GGG2014 algorithm (Wunch et al., 2015).

4.2.2   The Orbiting Carbon Observatory-2 (OCO-2), ACOS version 7r

The OCO-2 satellite launched in 2014 (Eldering et al., 2017). Data from routine measurements are available from September 2014 onward. OCO-2 X_{CO_2} measurements are tied to TCCON measurements (Wunch et al., 2016b), which are in turn tied to the World Meteorological Organization (WMO) standards (Wunch et al., 2010). The OCO-2 observations are tied to the TCCON by scaling observations at all sites across the globe rather than just the nearest ground site, thus OCO-2 provides a separate and distinct set of X_{CO_2} from the TCCON that agrees on average globally. For this study we used data from the NASA Atmospheric CO_2 Observations from Space (ACOS) version 7r algorithm (Crisp et al., 2012; O'Dell et al., 2012). OCO-2 measures X_{CO_2} globally at a resolution of about $1.3\,km \times 2.25\,km$, across 8 longitudinal pixels. It is in a sun-synchronous orbit and has an equatorial crossing time of around 1 pm local solar time. Worden et al. (2016) found typical land measurement precision (1σ) and accuracy to be 0.75 ppm and 0.65 ppm with the caveat that the precision estimate includes effects of synoptic variability. We describe the filtering of OCO-2 data and 'background' selection in 4.A.

4.2.3   GOSAT-ACOS version 7.3

The Greenhouse gases Observing Satellite (GOSAT) was developed by the Japan Aerospace Exploration Agency (JAXA) and measures thermal and near IR spectra from which X_{CO_2} and X_{CH_4} can be retrieved (Kuze et al., 2016). GOSAT footprints are ~ $10.5\,km$ in diameter (Kuze et al., 2009). The ACOS algorithm used for X_{CO_2} retrievals from OCO-2 has also been used to retrieve X_{CO_2} from GOSAT measurements. As of 2016, the latest version is 7.3 and uses the V201 radiance spectra (Kuze et al., 2016). Data from April 2009 through May 2016 were used in this study.

4.2.4   WRF Model with Hestia-LA

Hestia-LA estimates $FFCO_2$ emissions at the scale of buildings and street segments for the five counties associated with the SoCAB region (Gurney et al., 2012). The version 1.0 data product generated estimates for the 2010–2012 time period, and was used in this study. (Version 2.0 is now available upon request to kevin.gurney@asu.edu. Version 2.0 covers the 2010–2015 time period). Hestia-LA is resolved temporally to the hourly scale, accounting for diurnal, weekly, and
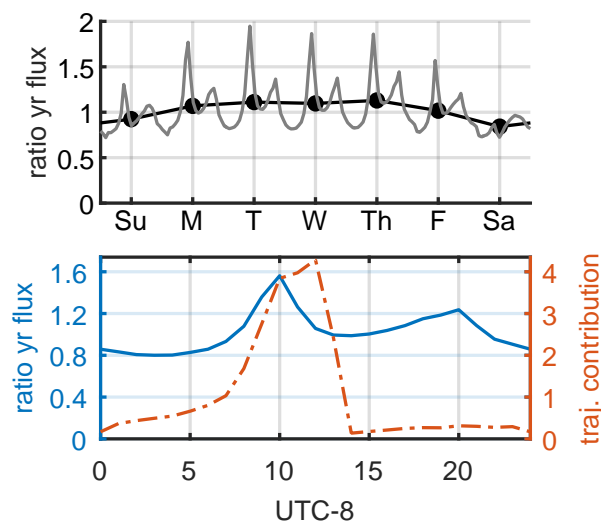
Figure 4.2: Time variation of Hestia-LA v1.0 fossil fuel emissions over the time period of this study (Jan–Apr 2015). Top: Average daily or hourly emissions compared to yearly average. Dots are daily averages centered on local noon. Higher emissions are shown for weekdays compared to weekends. Bottom: Average diurnal profile of emissions compared to yearly average. On the right axis is the normalized temporal contribution of air parcels passing through the ML in the SoCAB to measurements at 1300 (UTC-8).

monthly differences. The average weekday to weekend emission ratio is ~ 1.23 (Fig. 4.2) for the Hestia-LA product and dates used in this study. The version of Hestia used in this simulation does not include CO_2 emissions from non-fossil fuel sectors, which are estimated to be 19 % of California's total CO_2 emissions (Hanemann et al., 2008).

Hestia-LA was coupled with a 50 layer, $1.3 \, \mathrm{km} \times 1.3 \, \mathrm{km}$ WRF simulation described in more detail by Feng et al. (2016). The function of the WRF model is to simulate the atmospheric transport. This simulation was run for the January–April 2015 time period using unscaled emissions from 2012 that were shifted by a few days to maintain the correct day of week. This WRF model has an extent of 228×228 grid boxes over and around the SoCAB. For the March–April time period, we also explored simulations that have uniform emissions across the full WRF domain (see Fig. 1a by Feng et al. (2016)). This model provided two simulated X_{CO_2} fields, 1) from Hestia FF emissions and 2) from uniform emissions.

To compare the WRF results with measured data, we use the WRF grid box with a center point nearest the measurement site. The center coordinates for the Caltech box are 34.134°N, 118.123°W, 212 m a.s.l. The center coordinates for the JPL box
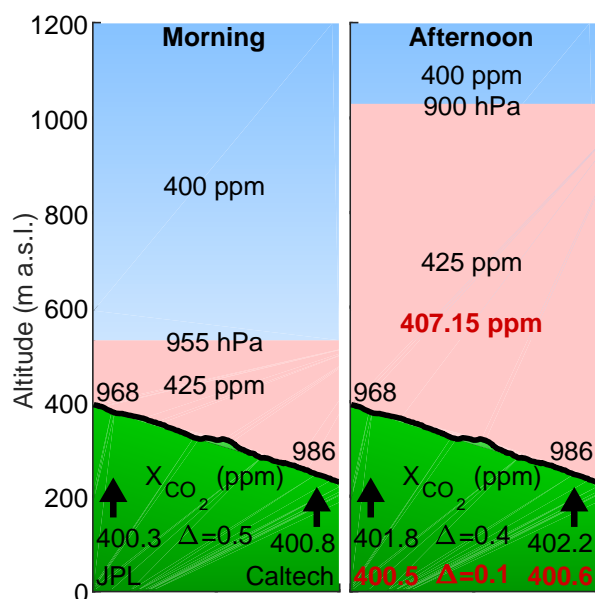
Figure 4.3: A cartoon visualization of the simple 'toy' model which has 2 above ground layers (the ML, and everything above the ML). The average ML height is flat with pressure in the model. The text labels show various pressures and average CO_2 mixing ratios. At the bottom are column abundances and their differences at the Caltech and JPL sites. Values in red for the afternoon are for the case when excess CO_2 is mixed into a deeper layer.

are 34.199°N, 118.172°W, 376 m a.s.l. The center coordinates for the AFRC box are 34.960°N, 117.879°W, 688 m a.s.l.

4.2.5   Simple CO_2 model

In addition to the full physics WRF simulations, we consider a simple 'toy' model to estimate X_{CO_2} gradients due to topography. It was constructed for only one purpose, namely to answer, "How much of a difference in X_{CO_2} is there between Caltech and JPL if at any moment in time the CO_2 mixing ratio is uniform throughout the ML, and the ML height (a.s.l.) is the same at both locations?" It does not provide a full description of the atmosphere, and a more detailed description is in the Supporting Information (Sect. 4.C). This model provides a third and final source of simulated X_{CO_2}.

In this model, we assume CO_2 is uniform both horizontally and vertically in the ML. The ML height is set to vary diurnally with a Gaussian shape each day. We also include an independent diurnal change in the ML CO_2 mixing ratio driven primarily
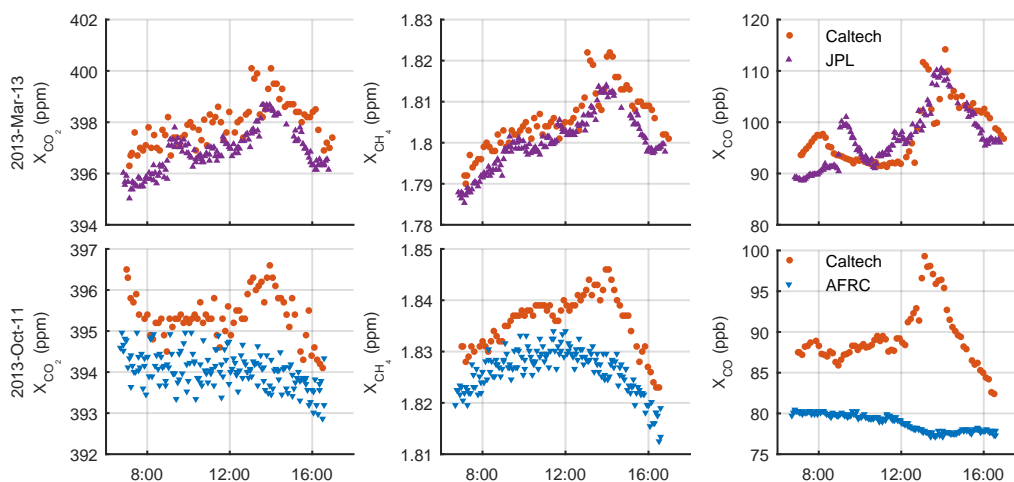
Figure 4.4: Example diurnal profiles of TCCON observations. Variations in column DMFs of different gases at the Caltech site are correlated. DMFs tend to be largest at Caltech. Caltech and JPL variations are similar. AFRC variations throughout the day are smaller and primarily from synoptic scale variability. In Fig. 4.5 are differences between sites.

from dilution by free tropospheric air and uptake by the biosphere (Newman et al., 2013) that varies with time of year. The range of the model ML CO_2 enhancement values above that in the free troposphere are in line with those seen at urban LA sites (Verhulst et al., 2016). Free tropospheric CO_2 levels are obtained using the TCCON a priori profiles. The model was run over the years 2011–2015.

In this model, the difference in X_{CO_2} between Caltech and JPL is due solely to differences in the terrain height. The total column abundances over higher altitude terrain contain a smaller fraction of the ML relative to the entire column, and thus we expect X_{CO_2} to decrease with increasing surface altitude. A basic cartoon of the model relating Caltech and JPL X_{CO_2} at different times of the day is shown in Fig. 4.3.

4.3 Temporal variations and persistent enhancements

4.3.1 Diurnal variation

Wunch et al. (2009) noted significant diurnal variations in X_{CO_2}, X_{CH_4}, and X_{CO} measured at the JPL TCCON site. Though we focus on X_{CO_2}, we include other gases for reference. The diurnal variations for all these gases are highly correlated due to the advection within the basin. In Fig. 4.4 are example diurnal profiles,

which show larger diurnal variations and larger DMFs at Caltech than at other sites. Chen et al. (2016) have also made column DMF observations around Pasadena using EM27/SUN spectrometers and noted similar features in the diurnal profiles. The average diurnal difference between sites is shown in Fig. 4.5. We assume, as did Wunch et al. (2009), that the differences in X_{CO_2} between sites are caused by enhancements near the surface, and so the differences have been divided by the surface averaging kernels of the measurements. For Fig. 4.5 these data were filtered as described in Appendix 4.B to show only 'typical' differences. These datasets do not necessarily cover the same time periods.

There are several possible mechanisms that drive these diurnal patterns. JPL is an area with more vegetation than Caltech and so some of the higher X_{CO_2} difference in the mornings compared to afternoons is likely due to respiration from the biosphere at night (Djuricin et al., 2010; Newman et al., 2013). The difference in X_{CO_2} compared with the AFRC site can be attributed to a growth of the ML until midday, after which the ML height decreases and the difference returns to morning levels. The X_{CH_4} difference in Fig. 4.5 between Caltech and JPL is similar to the Caltech-AFRC difference in the morning. This feature could be from air with high methane loading being advected from the California San Joaquin Valley, where there is high agricultural activity, to the AFRC site. Typically X_{CO_2}, X_{CH_4}, and X_{CO} are enhanced at Caltech relative to AFRC and JPL. Enhancements compared to AFRC can be attributed to polluted air being trapped in the basin. An increase in the ML height above Caltech may cause the difference compared to AFRC to 1) increase if polluted air flows horizontally to fill the rising ML, 2) decrease if the ML increases enough for polluted air to flow out of the basin over the mountains, or 3) stay the same if the polluted air is simply mixed vertically into a deeper ML.

Interestingly, differences between Caltech and JPL are at certain times of the day about as large as the differences between Caltech and AFRC, despite the JPL site also being within the basin and its proximity to Caltech. Over their full time-series, the enhancement compared to JPL is about one-third of that compared with AFRC. The enhancement relative to AFRC can be ascribed to the proximity of sources and to polluted air being trapped within the basin. However, this enhancement compared to AFRC can vary depending on the origins of the air masses which changes throughout the year (Verhulst et al., 2016). This can also affect the intra-basin enhancements—ML air masses less enhanced in CO_2 will lead to smaller horizontal gradients in X_{CO_2}. We examine the Caltech−AFRC difference in the next section. We explore
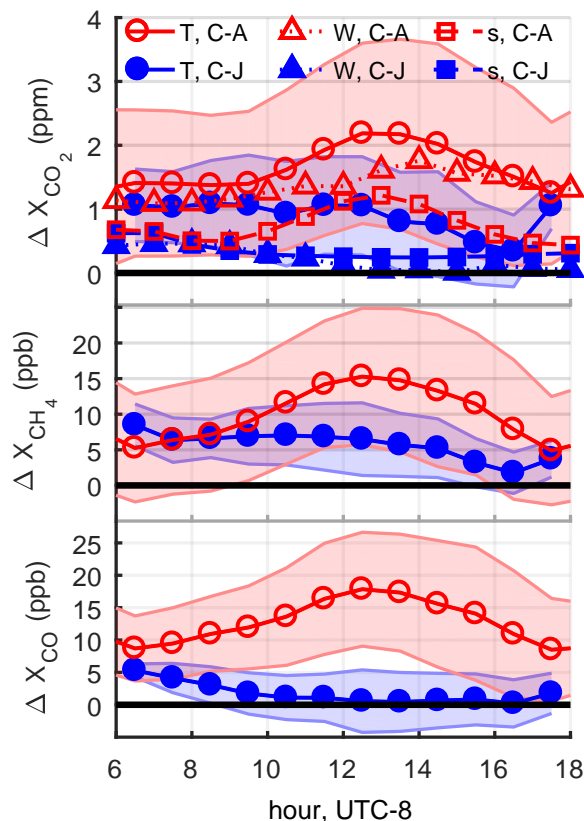
Figure 4.5: Diurnal differences in X_{gas} between sites from measured and modeled data over their respective time series. TCCON observations were filtered as described in Appendix 4.B to give 'typical' diurnal profiles. T=TCCON, W=WRF+Hestia-LA, s=simple model (Fig. 4.3), C-J=Caltech-JPL difference, C-A=Caltech-AFRC difference. Error bars (1σ) are shown for the TCCON differences, but are omitted from model values for clarity. Top panel: X_{CO_2} differences. TCCON $\sigma_{C-J} = 0.7$ ppm, $\sigma_{C-A} = 1.3$ ppm. WRF $\sigma_{C-J} = 0.5$ ppm, $\sigma_{C-A} = 1.0$ ppm. Simple model $\sigma_{C-J} = 0.1$ ppm, $\sigma_{C-A} = 0.2$ ppm. Center panel: X_{CH_4} differences. TCCON $\sigma_{C-J} = 3.8$ ppb, $\sigma_{C-A} = 8.7$ ppb. Bottom panel: X_{CO} differences. TCCON $\sigma_{C-J} = 3.4$ ppb, $\sigma_{C-A} = 7.8$ ppb.

reasons for the differences between Caltech and JPL in Sect. 4.4.

4.3.2 Full time-series

Here we focus on quantifying the X_{CO_2} enhancement in the SoCAB relative to background. We use observations at approximately 1300 (UTC-8) when the ML height is generally stable and well-developed, and the error due to the ML height determination in the WRF model is at a minimum (Feng et al., 2016). This is also the approximate time OCO-2 makes observations within the SoCAB on some days.
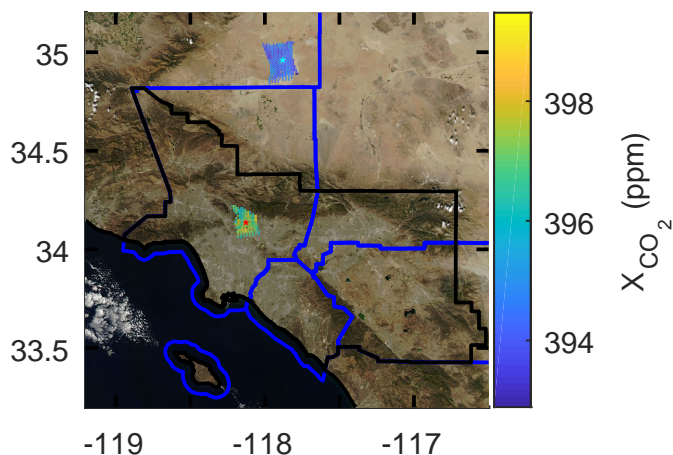
Figure 4.6: An example of target mode data from 19 Sept (Caltech) and 21 Sept (AFRC) 2014 overlaid on the MODIS image from 21 Sept 2014. These data were averaged into 0.01×0.01°bins.

An example of OCO-2 target data of the Caltech and AFRC sites is shown in Fig. 4.6.

Data from different sites and datasets were first averaged into 1 week time bins, before calculating differences. Because we assume most of the difference between locations inside and outside the basin are near the surface, we divide the TCCON and OCO-2 datasets by their surface averaging kernels from measurements within the basin. For OCO-2 non-target mode SoCAB data, any point within 60 km is used for comparison. For times when OCO-2 targeted the Caltech site and obtained many nearby observations, we only use data within 5 km of Caltech. This approach yields a similar number of observations for target and non-target overpasses; if all target observations were used the basin average enhancement is larger.

The Caltech-AFRC and Caltech-JPL differences with time in the TCCON X_{CO_2} are shown in Fig. 4.7. In general, X_{CO_2} measured at Caltech is greater than at JPL or AFRC. In late spring 2014, and winters 2015, 2016 there are lower enhancements of X_{CO_2} than at other times of year observed in the TCCON data. As noted in previous studies, the air trajectories to Caltech vary with season (Newman et al., 2016; Verhulst et al., 2016) and this likely contributes to the variability with more efficient ventilation of the basin during times of lower enhancements. The X_{gas} variability is weaker in the X_{CO} and X_{CH_4} data. The WRF data match in 2015, but the model time period is too short to observe the annual variability. The changes
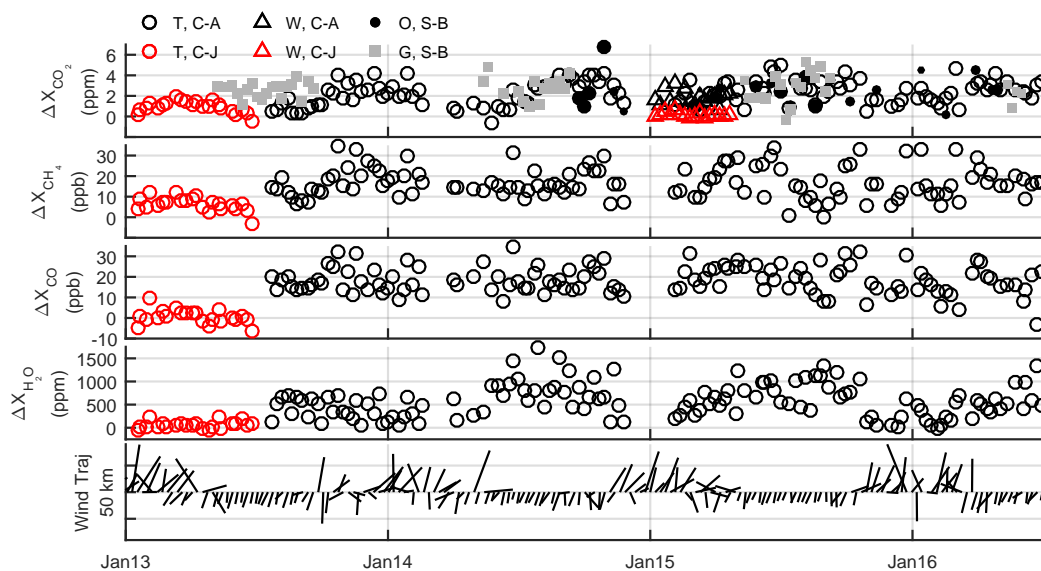
Figure 4.7: Timeseries of differences between data at different locations. T=TCCON, W=WRF, O=OCO-2, G=GOSAT, C=Caltech, A=AFRC, J=JPL, S=SoCAB, B=background. OCO-2 and GOSAT points are sized according to distance from Caltech, with points further away represented by smaller dots. Wind vectors in the bottom panel point to the direction the wind at 500 m a.s.l. originated from at 50 km from Caltech.

in X_{CH_4}, X_{CO}, X_{H_2O}, and wind trajectories indicate part of the X_{CO_2} fluctuations are due to atmospheric transport. Some of the X_{CO_2} variability is likely due to the biosphere of the SoCAB. Because of landscaping, there is significantly more vegetation within the SoCAB than at AFRC, and artificial irrigation may affect CO_2 seasonality (Newman et al., 2016). Newman et al. (2013) calculated that, at the surface, 50 % of excess CO_2 in Pasadena at night is from soil and plant respiration, which is presumably balanced throughout the year by uptake during the daytime. Because there are co-incident observations for Caltech and JPL for only ~6 months, this limits our understanding of the intra- SoCAB difference. The Caltech−JPL difference has a profile that peaks in spring, with lower enhancements in the early and mid-year. This behavior could arise from air masses originating from the desert in winter, and higher ML heights in summer which could decrease the ML to free troposphere gradients and hence the spatial X_{CO_2} differences.

If observations are concentrated at one location, they may not match basin-wide variations both in magnitude and in variation. Thus, in Fig. 4.8 we plot correction coefficients for variations in X_{CO_2} between single grid points and the average X_{CO_2}

for the SoCAB as a whole using the WRF simulations. These variations are for 1300 (UTC-8), and X_{CO_2} at the AFRC site has been subtracted as background. Locations towards the center of the basin and towards the southeast are most correlated with the basin as a whole. However, the largest X_{CO_2} enhancements are observed more towards the west; the western part of the basin is also where the majority of oil and gas exploration occurs. Typical X_{CO_2} values are 3× as large as the basin average just north of the Palos Verdes Peninsula ($\sim 33.9\,°$N, $118.2\,°$W) where GOSAT frequently made observations during 2009–2010. Towards the central and eastern ends of the basin, the magnitude of the ratio $X_{CO_2,local}$:$X_{CO_2,SoCAB}$ depends on the terrain, with larger ratios (or scaling factors) where the surface altitude is lower. To track small changes in X_{CO_2} enhancements that are related to changes in emissions requires the enhancements to be larger than the measurement sounding uncertainty and to correlate with the region emissions as a whole.

4.3.3 Persistent enhancements

GOSAT-ACOS v2.9 level 2 X_{CO_2} data within the basin have a robust $3.2 \pm 1.5\,(1\sigma)$ ppm ($n = 34$), enhancement compared to the X_{CO_2} observed over the desert from June 2009 to August 2010 (Kort et al., 2012). Results were similar for other studies using GOSAT observations ($2.75 \pm 2.86\,(1\sigma)$ ppm, $n = 8$) (Janardanan et al., 2016). Kort et al. (2012) estimated a 0.7 ppm change in X_{CO_2} (22 % of emissions) could be detected using GOSAT observations on a yearly time-scale. We repeat the analysis using the GOSAT-ACOS v7.3 data, and average weekly rather than in 10-day blocks. Over the same time we note a similar enhancement of $2.9 \pm 2.0\,(1\sigma)$ ppm. When we also include similar latitudinal ocean observations as background with a 21-day adjustment to better match the AFRC TCCON data, the enhancement is $2.3 \pm 1.8\,(1\sigma)$ ppm. Over the full June 2009–May 2016 time period the SoCAB enhancement determined by GOSAT observations is $2.4 \pm 1.6\,(1\sigma)$ ppm ($n = 118$). Enhancements observed by the OCO-2 satellite are similar at $2.4 \pm 1.5\,(1\sigma)$ ppm ($n = 26$).

Average differences from weekly averaged TCCON data are shown in Table 4.1. We emphasize that the Caltech−JPL X_{CO_2} difference is a significant fraction (~40%) of the Caltech−AFRC difference. It should also be noted that site-to-site biases on order of 0.1–0.2 ppm may exist among TCCON sites which could biases these enhancements (Hedelius et al., 2017). The CARB reported CO emissions of $0.91\,\mathrm{Gg\,CO\,yr^{-1}}$ for 2012 (`https://www.arb.ca.gov/app/emsinv/2013/emssumcat.php`), and $160\,\mathrm{Gg\,CO_2\,yr^{-1}}$ after scaling state emissions by 0.42 for

Table 4.1: TCCON X_{gas} differences.

Caltech−AFRC[a]	Difference	1σ
X_{CO_2} (ppm)	2.3	1.2
X_{CH_4} (ppb)	17	8
X_{CO} (ppb)	19	7
Caltech−JPL[b]	Difference	1σ
X_{CO_2} (ppm)	0.9	0.6
X_{CH_4} (ppb)	6	3
X_{CO} (ppb)	0.6	3.5

Differences in X_{gas} observed using weekly averaged TCCON data at 1300 (UTC-8) ± 1 hr. [a] From August 2013–June 2016 ($n = 128$). [b] From January 2013–June 2013 ($n = 22$).

the population only in the SoCAB (`https://www.arb.ca.gov/cc/inventory/data/data.htm`). The inventory estimated $CO:CO_2$ emission ratio is 9.0 (ppb ppm^{-1}). Observed ratios are 8.3 and 0.7 (ppb ppm^{-1}) for the Caltech-AFRC and Caltech-JPL differences, respectively. The Caltech-AFRC is in agreement with the inventory ratio, and the ratio of 11 (ppb ppm^{-1}) from Wunch et al. (2009). The CO enhancements for Caltech-JPL are lower than expected for reasons not fully understood.

4.4 Spatial SoCAB variations

In this section we seek to answer: what causes X_{CO_2} variability on the scale of a few km in the SoCAB as noted from Sect. 4.3? This increased variation can also be seen in OCO-2 data, with a median standard deviation of 1.04 (90% CI: 0.60, 1.71) ppm for points within 9 km, compared with 0.68 (90% CI: 0.48, 1.70) ppm for the desert. We focus on emissions, dynamics, and topography to explain this variability. For example, the enhancement at Caltech relative to the nearby JPL site may be due to a combination of emission source locations and dynamics, we consider these effects separately in Sect. 4.4.1 and 4.4.2. Caltech is closer to downtown Los Angeles and polluted plumes of air may not reach JPL before being advected eastward. In Sect. 4.4.3 we consider the impact of topography on X_{gas} in areas where the in situ DMF in the ML differs significantly from the rest of the column. A discussion of average surface CO_2 and the relationship with general wind patterns and topography is available from Feng et al. (2016) (Sect. 4 therein).
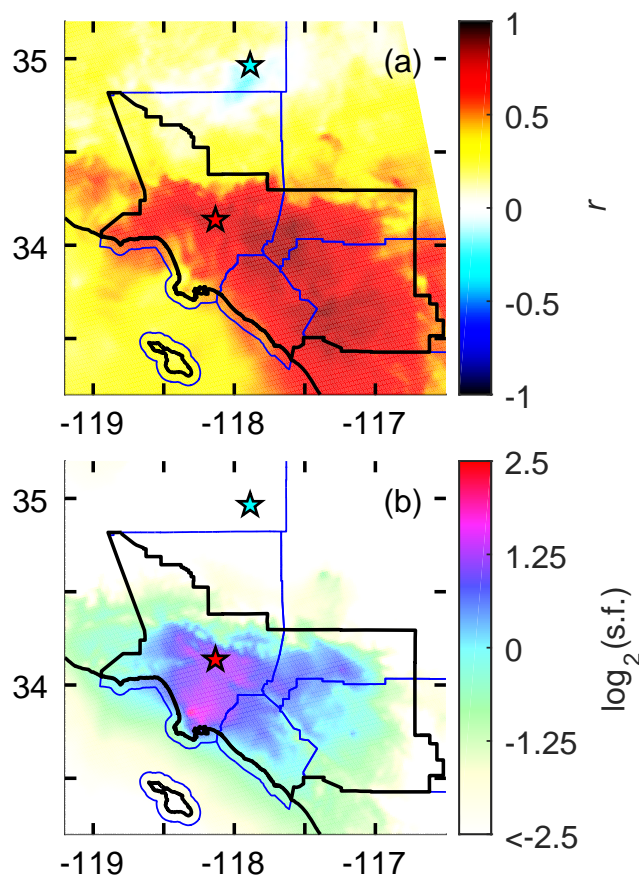
Figure 4.8: Comparisons between individual pixels and basin averaged fossil fuel X_{CO_2} from the simulated WRF data at 1300 (UTC-8). Shown are averages across all days. (a) Correlation coefficients between pixels and the basin average tend to be closer to 1 towards the east central part of the basin. (b) Scaling factors of basin compared to individual points. Points near the Palos Verde Peninsula are 3.5× as large as the SoCAB on average. Points near Caltech are 2.3× as large as the SoCAB average.

4.4.1   Local emissions and X_{CO_2} variance

The relationship between nearby Hestia FF emissions and simulated X_{CO_2} from the WRF dataset is analyzed. For each grid box in the WRF model output we calculate Pearson's r correlation coefficient between the simulated X_{CO_2} product generated by advecting Hestia emissions and the raw Hestia v1.0 emissions themselves for the set of spatially close points. The radii defining the small area of spatially close points are varied from 1.3 km to 30 km. We compute the average value of r at 1300 (UTC-8). We use r as an indicator of correlation because 1) it is unaffected by scaling factors—for example, it would not change if all emissions were doubled—and 2) is
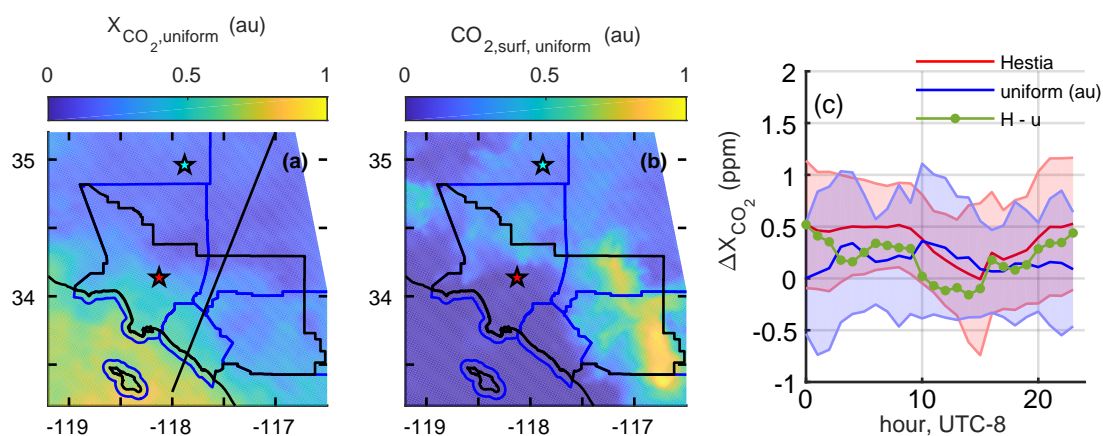
Figure 4.9: Maps of 1300 (UTC-8) average uniform emission products. au=arbitrary units (a) simulated X_{CO_2} for the uniform emission product. The higher ocean values are due to contributions above the ML, and a wind vector is shown in SI Fig. 4D.1 for the black line shown. (b) simulated CO_2 at the surface. (c) Differences in simulated X_{CO_2} between the Caltech and JPL sites. The diurnal profiles differ between simulations using Hestia versus uniform emissions. Error bars are 1σ.

unaffected by a constant offset, eliminating the need for a background value. If point source emissions were constant at all times and there were no wind and diffusion (i.e., no transfer of CO_2 between boxes), it would be expected that the surface flux into each box would explain all variance among boxes and $r(X_{CO_2}, FF) = 1$. In the data, we note only a weak r. The largest values (~ 0.18) are for areas with a radius $< 4\,\mathrm{km}$ and minimum FF emission gradients of at least $1\,\mathrm{g\,CO_2\,m^{-2}\,hr^{-1}}$. This suggests that the size of emission sources in each box by itself is only a weak predictor of X_{CO_2} variance.

4.4.2 Dynamical influences on X_{CO_2} variability

To estimate the impact of dynamics on the variation of X_{CO_2} within the basin, we analyze simulations performed with geographically uniform fluxes over the full WRF domain driven by the same dynamics as the simulations using Hestia-LA v1.0. We compare with the advected Hestia-LA v1.0 product, which is taken as 'truth' and denoted X_{CO_2}. If polluted air accumulates in the ML in the same locations due to meteorology without regards to the locations of emission sources, we would expect $r(X_{CO_2}, X_{CO_2,\mathrm{uniform}}) = 1$.

We observe no significant correlation between these products on scales of 1.3 km to 30 km across the basin (r values, Md: -0.045, 90% CI: $-0.250, 0.161$). There was

also no significant correlation for the points north of, and within 9 km of Caltech (Md: -0.009, 90% CI: -0.766, 0.712). In Fig. 4.9 are maps of the average X_{CO_2} and surface CO_2 for the uniform emissions case. (For the uniform emissions case we use arbitrary units which should not matter so long as there is no numerical diffusion in the model.) Over the ocean, X_{CO_2} is enhanced due to high CO_2 above the ML from return winds aloft (see SI Fig. 4D.1). Because emissions were uniform over the entire domain, this air with enhanced CO_2 from the desert region also contributes to the larger X_{CO_2} values seen over the ocean. If the surface CO_2 is taken as a first order approximation of how X_{CO_2} would behave without emissions from the desert, we see that enhanced CO_2 is seen in the eastern parts of the SoCAB. However, the finer features that relate with topography in Fig. 4.10 are not seen in Fig. 4.9.

Dynamics alone cannot explain a significant fraction of the difference observed between the Caltech and JPL sites. An extension of this test we did not try would be to include uniform emissions only within the geographical SoCAB boundaries and see how they relate when compared with the Hestia run. The distribution of emission sources needs to be considered concurrently with dynamics to explain X_{CO_2} variations in the SoCAB.

4.4.3 Terrain effects

To the extent that the same excess CO_2 is simply mixed into a deeper ML, column measurements are insensitive to ML height (Yang et al., 2007). For areas with ML DMFs that are enhanced compared to free tropospheric levels, this causes in situ DMFs within the ML to drop and become closer to free tropospheric levels as the ML height increases (McKain et al., 2012; Newman et al., 2013). However, if the fractional change in ML height is different between sites the column difference will also change. This is considered in the 'toy' model (Fig. 4.3). Note that Fig. 4.3 also provides a numerical example of this concept. Going from morning to afternoon requires a horizontal flow of CO_2 from Caltech to JPL. If the surface were at a uniform altitude the Δ between Caltech and JPL would be zero.

Differences in the ML height above ground level explain part of the variation in X_{CO_2} between Caltech and JPL. Part of the remaining discrepancy is because $\langle CO_2 \rangle_{ML}$ (where bracket notation indicates the average here) is not the same at both locations. This model further assumes that the ML height is at the same pressure height p_{ML} at both locations. This assumption is better inland than closer to the coast—for example Ware et al. (2016) noted a sharp transition in ML height between the
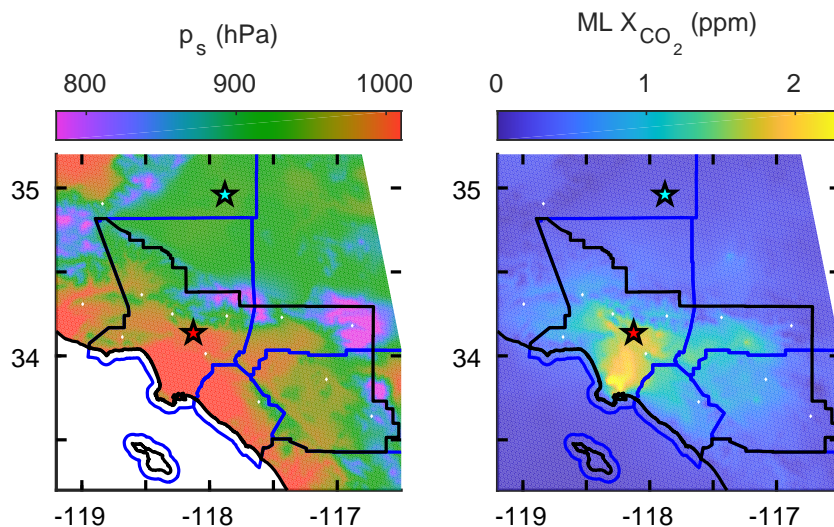
Figure 4.10: Averages from the WRF simulation at 1300 (UTC-8). (a) Average surface pressure and (b) the contribution of ML CO_2 to the total column. Over areas $\sim 0.1°$ many features in the surface pressure map are reflected in the ML X_{CO_2}. This could arise from different fractional contributions of the ML to the total column (see Fig. 4.3). Small white diamonds are shown to highlight some areas where this can be seen more clearly.

shallow marine layer (about 2–3 km onto land) and the convective regime further inland. Though the ML may fluctuate by a few hundred meters over a distance of several kilometers due to updrafts (Nielsen-Gammon et al., 2008), these are averaged out with downdrafts over an hour or so. Over smaller areas, average variations in the ML height pressure are smoother than changes in surface pressure as noted by streamlines over topographic features (Perry and Snyder, 2017). Maps of the average surface pressure p_s and ML X_{CO_2} are shown in Fig. 4.10. Over small areas $\sim 0.1°$ many features are reflected in the average ML X_{CO_2} at 1300 (UTC-8).

X_{CO_2} (c) can be calculated by considering the weighting of the ML and rest of the column separately:

$$c = \frac{p_s - p_{ML}}{p_s} \langle CO_2 \rangle_{ML} + \frac{p_{ML}}{p_s} \langle CO_2 \rangle_{aboveML}, \tag{4.2}$$

where $\langle CO_2 \rangle_{aboveML}$ is the average CO_2 DMF from the top of the ML to the top of the atmosphere. Equation 4.2 can be rewritten as:

$$c = \langle CO_2 \rangle_{ML} + \frac{p_{ML}}{p_s} \left(\langle CO_2 \rangle_{aboveML} - \langle CO_2 \rangle_{ML} \right). \tag{4.3}$$

If the above assumptions were perfect, then all variation in X_{gas} between locations would be linearly related with p_s^{-1}. If $\langle CO_2 \rangle_{ML} > \langle CO_2 \rangle_{aboveML}$ then the correlation is negative.
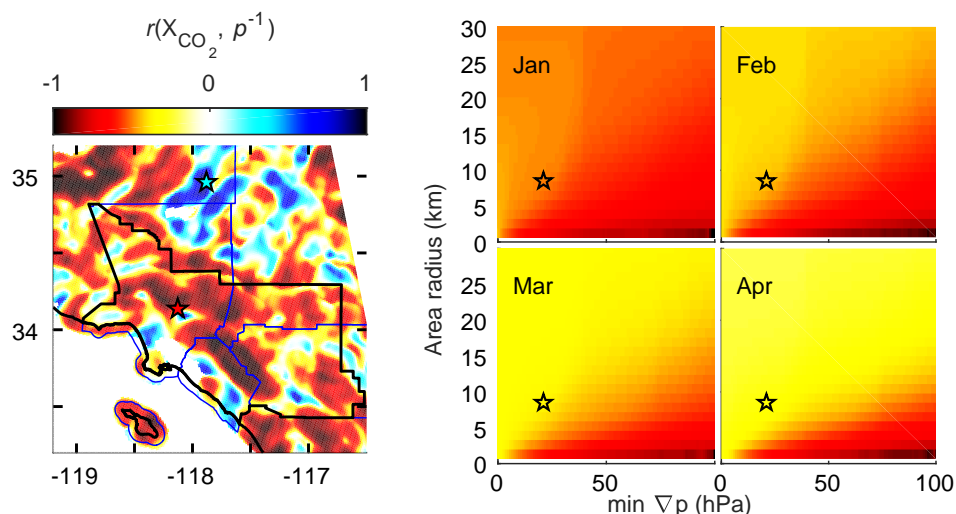
Figure 4.11: Correlation coefficients relating X_{CO_2} and p_s^{-1}. Large negative correlations (red) indicate that increases in X_{CO_2} are highly correlated with lower surface heights. Left panel: Shown spatially for areas of radii 9.1 km (~7 WRF boxes). Data are from 9 March 2015, 1300 (UTC-8). Correlations are stronger over steeper terrain. Right panel: Correlation as functions of area radii and minimum pressure differences (rather than spatially). Shown are averages over the entire SoCAB for data from 1300 (UTC-8). The star marks the distance and ∇p between Caltech and JPL. Starting in the bottom right corners (large p gradient, small radius) the correlation is strong. Going up (larger radii) the correlation weakens. Going right to left (smaller minimum p gradient) the correlation also weakens.

We evaluate this relationship using r over small areas with the simulated FF X_{CO_2} from the WRF model. We choose 1300 (UTC-8) as the analysis time because it is local midday when the ML is more stable, and it corresponds to the approximate time of OCO-2 and GOSAT measurements. Figure 4.11 includes a map of $r(X_{CO_2}, p_s^{-1})$ for areas of radii 9 km for 9 March 2015 and $\nabla p > 7$ hPa. In general, we note a strong negative relationship in areas within the SoCAB where the terrain changes rapidly. For example, $r < -0.5$ towards south side of the San Gabriel Mountains ($\sim 34.2°$ N) and around the Santa Ana Mountains at 33.7° N and 117.5° W. The relationship is weaker towards the peak of the San Gabriel range. Towards the base of the San Gabriel range on the northern side, we note a positive relationship in places. The increase in X_{CO_2} with the surface altitude may be from basin outflow, where further distances from the basin coincide with a decrease in altitude. We also note strong negative relationships towards the southern end of the California Central Valley (35° N and 119° W). The correlation coefficient r is highly variable across the Mojave desert surrounding the AFRC site.

We analyze the mean r in the SoCAB for different small area radii and different minimum pressure gradients for four different months (Fig. 4.11). On average r is negative, with stronger correlations for smaller areas as well as over areas with larger pressure gradients. Across the full basin for 9 km areas the median is −0.37 (90% CI: −0.52, −0.15). The correlation becomes weaker in April as the temperature increases and the ML becomes less stable. For points north of (where terrain is steeper), and within 9 km of Caltech, the median for January to April is $r = -0.45$ ($\pm 1\sigma$ CI: −0.76, −0.04). The median coefficient of determination (R^2) is thus 20 % ($\pm 1\sigma$ CI: 0 %, 58 %), suggesting about 20 % of the variance in X_{CO_2} between Caltech and JPL can be explained by changes in topography.

The toy model (Fig. 4.3) provides another measure for how much of the X_{CO_2} difference can be explained by differences in surface altitude. Based on the current parameterization of the simple model, the median ratio between model:measured values is 36 % ($\pm 1\sigma$ CI: 10%, 101%). A site-to-site TCCON bias of up to ± 0.2 ppm would make the median value 29–46 % (Hedelius et al., 2017). Thus, approximately 36 % of the X_{CO_2} difference between Caltech and JPL can be attributed to differences in altitude using this simulation.

4.5 Conclusions

Observations of X_{CO_2} within the SoCAB are enhanced compared to the nearby Mojave Desert. This typical enhancement is due to the proximity of anthropogenic sources of CO_2 combined with the basin topography which can lead to the trapping of polluted air. Enhancements of X_{CO_2} within the SoCAB are $2.3 \pm 1.2\,(1\sigma)$ ppm based on the TCCON observations. OCO-2 v7r enhancements are similar ($2.4 \pm 1.5\,(1\sigma)$ ppm). These are smaller than the $3.2 \pm 1.5\,(1\sigma)$ ppm derived from GOSAT observations by Kort et al. (2012), but is more in line with the $2.75 \pm 2.86\,(1\sigma)$ ppm results of Janardanan et al. (2016). We also observed lower enhancements with GOSAT-ACOS v7.3 data ($2.4 \pm 1.6\,(1\sigma)$ ppm) over a longer time period with a different seasonal sampling weighting. There is also seasonality in the TCCON data but it is not apparent in the GOSAT observations, which may be because air in Pasadena is more strongly influenced by seasonal wind patterns. All of the basin enhancements from different observation sets are within 1σ agreement.

There is significant X_{CO_2} variation within the SoCAB, even in locations less than 10 km apart. Between the Caltech and JPL TCCON sites, the difference is $0.9 \pm 0.6\,(1\sigma)$ ppm, which is a significant fraction (~40 %) of the Caltech−AFRC

difference. Both dynamics, and the locations of sources need to be considered simultaneously to account for these variations. Topography also appears to play a significant role in some locations in the basin. Using the difference in X_{CO_2} between Caltech and JPL, we estimate 20% ($\pm 1\sigma$ CI: 0%, 58%) (from the WRF analysis, Sect. 4.3) to 36% ($\pm 1\sigma$ CI: 10%, 101%) (from our simple climatology model) of the difference is explained by changes in topography alone. Though other factors such as emissions and dynamics together explain more than half of the difference, topography changes in the presence of a sharp gradient between the mixed layer and free troposphere contribute significantly to the difference.

The importance of topography in driving variation in X_{CO_2} has implications beyond the urban area studied here. Such influence is undoubtedly important in forested and agricultural regions as well. Though previous papers have included comments on column measurements having reduced sensitivity to the ML height, this sensitivity is not zero. Thus, correctly parameterizing the ML is important in models using column measurements. This is especially important for studies of fluxes within small areas using column measurements (e.g. Chen et al. (2016)), as errors in the ML height can lead to significant errors in the retrieved fluxes.

4.A   OCO-2 Data, filtering, and background

Included in the OCO-2 dataset are two types of data quality filters—warn levels (WLs) and a binary X_{CO_2} quality flag. WLs are derived using the Data Ordering Genetic Optimization (DOGO) algorithm (Mandrake and Doran, 2015a). Generally, WLs increase as the data quality becomes less reliable. WLs are based on specific retrieval parameters such as surface roughness and the retrieved aerosol optical depth (Mandrake and Doran, 2015b). DOGO also assigns lone outliers to higher WLs (Mandrake and Doran, 2015a). For our analysis we are primarily concerned with lone outliers on scales less than $\sim 10\,\text{km}$, which are not always flagged by higher WLs or the binary flag. When included in an inversion, these types of outliers can significantly change flux estimates.

We create a custom filter based on small area analysis. Though this paper focuses on determining reasons for X_{CO_2} variations over areas of similar size, the values that are removed by this filter are significantly different from other values in the small area, even though some true variance is expected. Our custom filter is based on analyzing areas of radius $< 8\,\text{km}$. We check for low and high outliers. Data are flagged if 1) the furthest points are $\geq 0.7\,\text{ppm}$ to the next nearest point or 2) the

furthest points are ≥ 0.4 ppm away with a z-score ≥ 2.58 (corresponding to a 99 % range). This filter removes an additional 1.3 % of data at WL = 0 and 3.8 % of data at WL ≤ 14. Low outliers are 10–100 % more frequent than high outliers. The ratio of high to low outliers is closer to one at lower WLs.

For our analysis we also require 'background' measurements of X_{CO_2}. Kort et al. (2012) used satellite observations made over the nearby rural desert when calculating the SoCAB X_{CO_2} enhancement using observations collected by the GOSAT. This choice was made because the desert is geographically close to the basin which minimizes sensitivity to global or zonal observational bias. We use the TCCON observations at AFRC as background. We also considered ocean observations at similar latitude out to 179° W, but these OCO-2 observations were shifted in time and biased low in comparison with the AFRC TCCON data. While this bias may reflect real X_{CO_2} gradients due to atmospheric dynamics, it may also result from bias between the OCO-2 data taken over land (in nadir and glint modes) versus data taken over the ocean in glint mode only. The comparability of the different modes is being evaluated (Wunch et al., 2016b).

4.B TCCON Data filtering

For Fig. 4.5 we filtered the binned TCCON data based on what were considered atypical events following methodology similar to Wunch et al. (2009). Days at Caltech with changes in X_{CO_2} > 6.5 ppm, X_{CH_4} > 40 ppb or X_{CO} > 30 ppb were flagged as bad which eliminated 53 of the original 1101 days with measurements from 1 Jan 2013 onward. Atypical CO:CO$_2$ ratios > 20 ppb:ppm were flagged, which was 34 more days. We also filtered for Santa Ana wind events, characterized by unusually low variations throughout a day. Days with changes of X_{CO_2} < 0.8 ppm or X_{CH_4} < 5 ppb or X_{CO} < 2.5 ppb were eliminated which was an additional 111 days. In total 18 % of the total days were flagged by all filters. Of the 158 days with measurements at JPL, 37 were filtered by the Caltech flags. JPL data were flagged similarly to Caltech, except low outlier flag limits were set at 75 % because we expect average enhancements to be less at JPL. This eliminated 20 more days for a total of 101 comparison days between Caltech and JPL.

AFRC is considered a 'background' site and there are 514 comparison days with Caltech that are not filtered by the Caltech flags (of 640 days through June 2016). Days with changes of X_{CO_2} > 2.0 ppm or X_{CH_4} > 23 ppb or X_{CO} > 15 ppb were eliminated, which was an additional 42 days, for a total of 472 comparison days

between Caltech and AFRC.

4.C   Detailed description of simple model (Sect. 4.2.5).

This simple model was constructed with one purpose, namely to answer: How much of a difference in X_{CO_2} is there between Caltech and JPL if the ML is perfectly well-mixed with a top at the same pressure height at both locations? It does not represent the full true state of the atmosphere. It was constructed using five inputs including:

1. A function for the ML height.

2. Average in situ ML enhancements of CO_2.

3. Profiles of CO_2 for the remainder of the column above the ML.

4. 'Background' values of ML enhancements if there were no enhancements from local emissions.

5. Surface pressures at the different sites.

This is only meant to be a climatology model, showing what the average behavior could look like. It is not meant for direct single day comparisons with measurements.

We also include the AFRC site in the model, but for the purpose of evaluating the model performance rather than extracting results. AFRC is treated differently from Caltech and JPL in that the simulated X_{CO_2} is simply the integrated a priori column. The Caltech-AFRC difference is discussed in Sect. 4.C.6.

4.C.1   Mixed layer height

For the ML height we make a simple assumption of a Gaussian shape with a peak at 1300 (UTC-8). Again, we note the true atmosphere is more complex (see Ware et al., 2016); our assumption is made simply to get a picture of how the atmosphere may behave on average with high and low values averaging out to get the mean estimate. The peak and base of the daily ML estimates were set to have annual sinusoidal variations. Sinusoidal variation values were set by fitting ECMWF model data from 2010–2014. The maximum daily peaks seemed too large and were scaled down by a factor of 2 to better match the values reported by Ware et al. (2016) and Newman et al. (2013). These variations were (in km):
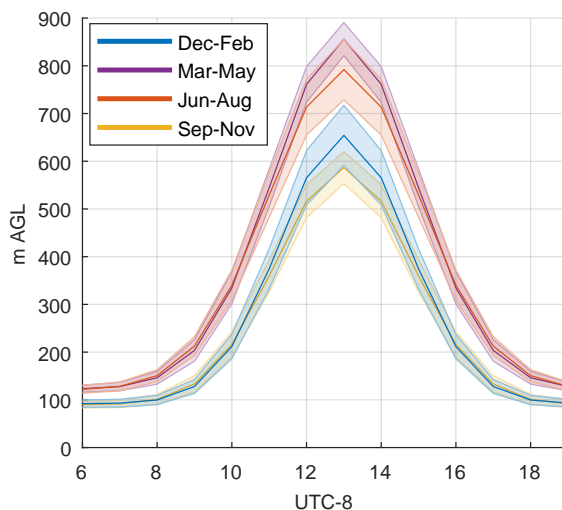
Figure 4C.1: Mixed layer heights for different seasons in the model. Center lines are means and shaded areas are 1σ across the full season.

$$\text{max ML height} = 0.5\,(0.333\sin((yr + 0.848) \times 2\pi) + 1.443) \qquad (4C.1)$$

$$\text{min ML height} = 0.0239\sin((yr + 0.887) \times 2\pi) + 0.106, \qquad (4C.2)$$

where yr is the fraction of the year passed since Jan 1. Further, the width of the daily peaks depend on the length of the day, and have 1σ values that are $\frac{1}{3.4}$ the length of the solar day (between morning and evening SZA=88°).

Seasonal averages are shown in Fig. 4C.1. There is general agreement here with the results of Ware et al., (2016). We find the final results of this model are not particularly sensitive to errors in ML height. This is illustrated in Fig. 4C.2, where once the ML height reaches the altitude at JPL a change from 200 to 1100 m a.g.l. only causes about a 0.05 ppm change in ΔX_{CO_2}.

4.C.2   ML CO_2 enhancement

The true average ML CO_2 enhancement is a complex function of biosphere activity, fossil fuel emissions, dilution from an increased ML volume, and vertical extent of mixing. We do not attempt to account for all of these individually. Instead, we make approximations in our model here based on the average diurnal behavior noted by Newman et al. (2013) and McKain et al. (2012). We create a lookup table, with estimates of diurnal profiles for each month with some added noise. These profiles have draw-down during the daytime, as shown in Fig. 4C.3. We added
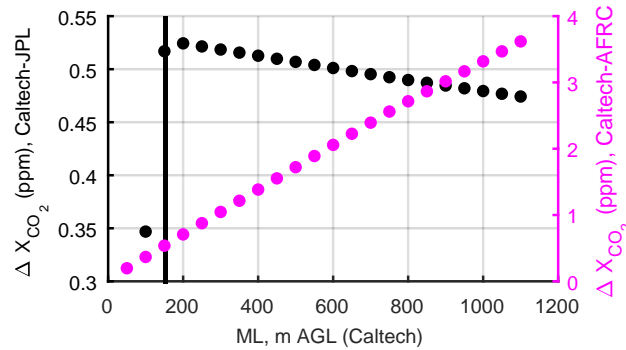
Figure 4C.2: X_{CO_2} differences for different mixed layer heights (above Caltech). The black line indicates the difference in altitude between the 2 sites. Data are from 1 June 2013 with a fixed 30 ppm CO_2 surface enhancement. Note the difference in scale compared to Caltech−AFRC.
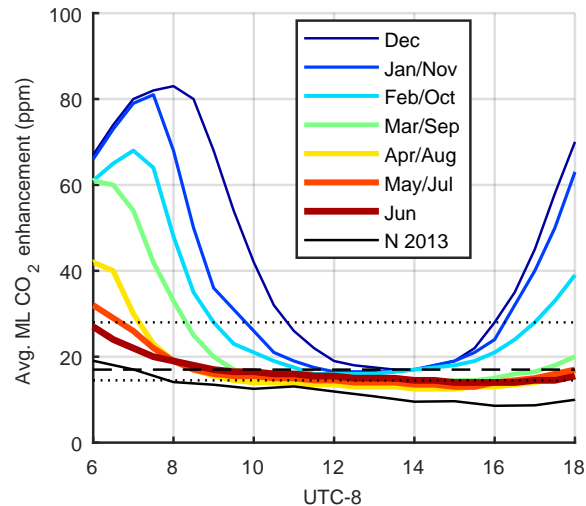

Figure 4C.3: Parameterized average mixed layer CO_2 enhancements at Caltech. The black line is from Newman et al., (2013) using data from May–June 2010. Dashed lines indicate the 25th, 50th, and 75th percentiles.

additional fossil fuel emissions to the ML enhancement as compared to Newman et al. (2013) because during May–June 2010 when they made their measurements meteorology conditions were atypical which resulted in lower pollution levels than normal (Hersey et al., 2013). Other months have larger enhancements from less biospheric uptake and a shallower ML.

Despite the generalization of the surface CO_2 behavior at Caltech, the median of 17 ppm is within the 50% confidence interval of the full and mid-day medians noted by Verhulst et al. (2016) at both the USC and FUL sites. Any median value in the
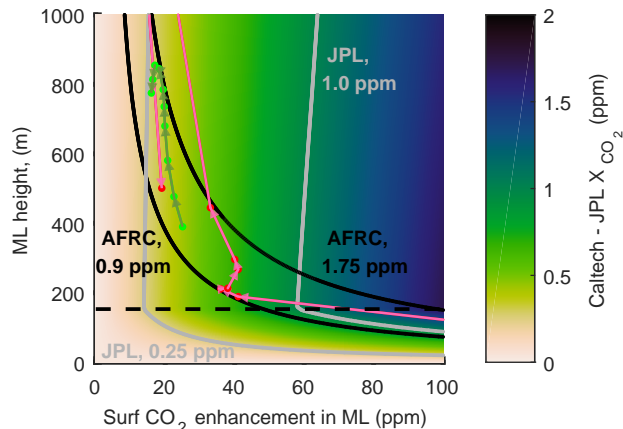
Figure 4C.4: Depiction of what the Caltech-JPL X_{CO_2} differences would be for various ML heights and CO_2 enhancements using 20 May as a test day. Gray and black isopleths are for fixed differences that would be seen for Caltech-JPL and Caltech-AFRC respectively. The green dots are for values observed by Newman et al., (2013). Pink arrows are from constraining values based on the average behavior of the Caltech-JPL and Caltech-AFRC differences (where the isopleths cross for each pair of hourly averaged points).

10–20 ppm range would match this criteria.

Figure 4C.4 can be thought of as a lookup table for what the difference in X_{CO_2} between Caltech and JPL would be for different ML heights and surface CO_2 enhancements. Note that for ML heights that are 200 m or higher, there is much greater sensitivity for the range of surface CO_2 values (left and right) than there is for ML height (up and down).

4.C.3 CO_2 profiles

Profiles for the remainder of the column are from TCCON a priori mixing ratio profiles. These are the base estimate profiles used in the GGG algorithm when fitting spectra. They are generated based on the secular CO_2 increase with annual variation that depends on latitude. Upper parts of the profiles are adjusted for shifts in the tropopause height. In conjunction with the mixing ratios, profiles are generated that include the pressure at different atmospheric levels based on NCEP/NCAR reanalysis data.

For the AFRC site, the column abundances are calculated by integrating the a priori columns.

4.C.4 'Background' CO_2 values

'Background' CO_2 levels are estimated from a pressure weighted average between 5–9 km in the a priori mixing ratios of CO_2. They are an estimate of how much CO_2 would be seen at the surface without local emissions.

4.C.5 Site surface pressure

Site surface pressures are derived by interpolating to the site altitude (240 m for Caltech, 390 m for JPL) using the a priori pressure profiles.

4.C.6 AFRC and model evaluation

The modeled-measured mismatch for ΔX_{CO_2} between Caltech and AFRC was about 1.77. Because the 'toy' model underestimates the observed difference between Caltech and AFRC (Fig. 4.5), it suggests our model needs more CO_2 over Caltech. If this was due to an underestimated enhancement of CO_2 in the ML it would cause an underestimation of the Caltech-JPL difference by about 45%. If it was due to an underestimated ML, or a residual layer with enhanced CO_2 above the ML, it would cause a slight overestimation of ~0.1%.

We do not take further action here to correct for the model-measured mismatch. The scale factor of 1.77× seems unreasonably large to scale either the surface enhancement or the ML height in the model. Our model only has two layers, and does not include a residual layer disconnected from the surface and observed by Ware et al. (2016). It seems likely that at least part of the reason for the under-predicted ΔX_{CO_2} is from a residual layer, so we do not attempt to further correct for the measured-model mismatch.

4.D WRF wind vector field

In Fig. 4D.1 is a depiction of the average latitudinal and vertical wind directions. The prevailing surface wind is inland, but winds aloft return to the ocean. Returning winds are enhanced in CO_2 in the uniform emissions scenario. This leads to enhanced X_{CO_2} over the ocean.
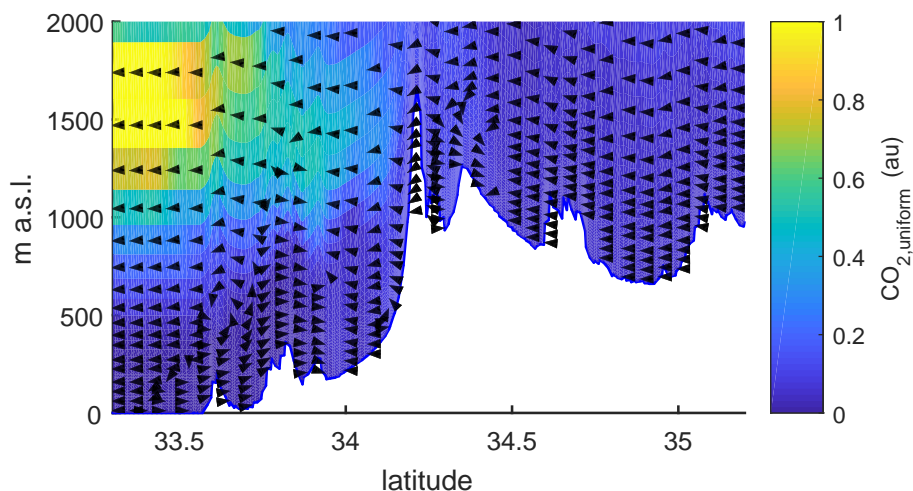
Figure 4D.1: Average wind vector field for the cut shown in Fig. 4.9 in the main text.

Edited by: A. Steiner

Reviewed by: Two anonymous referees

Chapter 5

PARALLEL PROJECTS AND FUTURE OUTLOOK

5.1 Introduction

Several side-projects were pursued in parallel while estimating the fluxes of trace gases, particularly CO_2, from the SoCAB. One of these projects, on AOD retrieval and characterization in the SoCAB, was described in Chapter **??**. Other projects pursued are described briefly here. These projects included flux estimates from smaller regions, and flux estimates of different gases using tracer-tracer correlations. A paragraph is devoted to each in Section 5.2. This work has opened up new avenues for research. Further research directions are discussed in Sect. 5.3.

5.2 Parallel Work

The portable solar viewing Fourier transform spectrometers (SV-FTS) discussed in Chapter 2 have opened up opportunities for focused, short term (1–2 month) campaigns. These campaigns can involve using measurements from several of these portable SV-FTS to estimate fluxes from point sources such as forests, dairies, and entire urban areas. To our knowledge campaigns have been carried out for Berlin (Hase et al., 2015), Chino California dairies (Chen et al., 2016; Viatte et al., 2016), Paris, Tokyo, the Colorado front range (Kille et al., 2017), Boston, Fairbanks Alaska, and the California Bay Area. Future studies are planned for Munich Germany and a revisit to the Boston area.

One of the simplest ways to create an inversion to calculate fluxes is by using an upwind-downwind differential measurement (Chen et al., 2016). In this study a uniform flux was assumed over an area with a high concentration of dairy farms in Chino California. Four SV-FTS instruments were deployed to surround the dairies. Upwind measurements were subtracted from concurrent downwind measurements which eliminated common airmass dependent biases. The wind speed and direction was assumed to be constant over the full domain, as was the mixing layer height (in m a.g.l.). These estimates were sensitive to the parameterizations, but were consistent with past estimates.

This same dataset from Chino was also implemented with a Weather Research and Forecasting model in Large-Eddy Simulation mode (Viatte et al., 2016). This addi-

tional study was conducted to make use of data from days with less consistent winds instead, and to conduct a Bayesian inversion to estimate the source distribution. This study included a large range of methane fluxes, with smaller central values than seen in previous studies. It was concluded that these smaller values were in line with a decrease in the head of cattle.

In addition to using transport models to estimate fluxes, tracer-tracer analysis can also be used given a prior emissions inventory of one of the gases. Tracer-tracer correlations were examined with aerosols in Chapter **??**. Ethane and methane anomalies are well correlated in the SoCAB, and their relationship was used to estimate ethane emissions (Wunch et al., 2016a). Ethane emissions to the SoCAB atmosphere increased from 2013 to 2016, as did the the C_2H_6:CH_4 ratio in natural gas. By comparing the ratio in natural gas to that in the atmosphere, Wunch et al. (2016a) estimated that over half of the excess atmospheric methane in the SoCAB is attributable to losses from natural gas infrastructure.

5.3 Next steps - ideas for future research

This work may spur off various future projects related to measurement error analysis, flux inversions using column measurements, and tracer-tracer relationships among atmospheric constituents. In Chapter 2 I discussed various sources of error that could affect EM27/SUN retrievals. It was unclear, however, which errors most strongly affect the retrievals on a long-term (year+) time scale and how to implement a standard instrument monitoring protocol. Thus, there is a need to determine how to monitor accuracy of these instruments long-term, and what this accuracy is. The TCCON accomplishes this using aircraft and balloon-borne in situ measurements. In Chapter 2 I also recommended monitoring the ILS on about a monthly time-scale, however the current method is time and labor intensive (Frey et al., 2015). There is a need to develop a passive or automated method to monitor the ILS using, for example, an HCl gas cell in the solar beam.

Past work estimating emissions using SV-FTS instruments has required placing multiple instruments around a source, both upwind and downwind, or to actively move a instrument throughout a day to get measurement enhancements over background (Chen et al., 2016; Viatte et al., 2016; Kille et al., 2017). However, if wind conditions are variable and airmass dependent biases are minimal, then a single instrument at a fixed location could be used to measure both 'upwind' and 'downwind' of a source. For example, Lindenmaier et al. (2014) used a single site to verify emissions using

a combination of a dynamical model and different tracers to distinguish air mass origins. Lagrangian back-trajectory methods could be used to determine the history of air masses. Other methods may also be developed to determine 'background' levels. A study attempting to use a single SV-FTS for quantifying fluxes may consider using data from a campaign with multiple instruments, and show how much information is lost by only using data from one appropriately placed spectrometer.

A more challenging, though potentially more direct, method to estimate differences between upwind and downwind measurements could be to use differences from raw spectra rather than retrieved data. This method would be challenging and would require an accounting of the difference in ILS among instruments, and may also require accounting for changes with transmittance as a function of airmass. From the Beer-Lambert law $C \propto A$, where C is the abundance or atmospheric concentration, $A = \ln(T)$ is absorbance, and T is transmittance. The ratio X_{gas} could be calculated by

$$\frac{C_2}{C_1} = \frac{A_2}{A_1}. \tag{5.1}$$

To get the absolute difference, as estimate could be made of C_1, which will likely contribute to an error of less than 5% of the difference. Alternatively the difference, ΔC could be calculated by retrieving ΔX_{gas} directly from ratioed transmission spectra $\frac{T_2}{T_1}$. Ratioed transmission spectra should be equivalent to having had the absorbance due to unchanging layers of the atmosphere subtracted out, and thus the a priori profile would need to be updated in the retrieval. A major drawback of this method is the requirement for an accurate knowledge of the continuum level before taking spectral ratios—this would take significant creatively to determine. The continuum level is usually something included in the state vector, and is typically not required a priori.

Flux estimates made using column measurements on local and regional scales have primarily focused on emissions. There is a dearth of studies on how column measurements may be used to measure uptake from forests or agricultural locations on the scale of ~5–50 km. Instruments could be stationed to surround high vegetation areas and observe fluxes at different seasons. An extension of such a campaign could also include placing instruments at different altitudes over an area of ~10 km and include surface or tower in situ CO_2 measurements and mixed layer height measurements by lidar. This way the hypothesis of variable X_{CO_2} from differences in terrain predicted in Chapter 4 could be tested.

Given the increasing number of inversions at smaller (<100 km) scales, it would be

informative to run more sensitivity tests and come up with standard optimized proce-
dures. For example, different studies using Lagrangian particle dispersion methods
use different numbers of particles. There is often little discussion on whether more
particles would be beneficial, or if fewer could be used to still achieve similar results
with increased computational efficiency. It is also unclear how the distribution of
particles (layer weighting, layer density, end-point positioning, etc.) affects results.
Sensitivity studies could also include different options for determining background
values, different a priori spatiotemporal flux distributions, and different underlying
Eulerian models. This type of project could also include developing and distributing
software for inversion estimates using a variety of datasets.

Column tracer-tracer analysis, such as those discussed in Chapter **??** and by Wunch
et al. (2016a), has involved only comparing two tracers at a time. Additional insight
could be gained by multidimensional analysis, such as McLean fits (McLean, 2014),
or some form of principal component analysis. For example, positive matrix factor-
ization has been applied to aerosol mass spectra to determine principal components
(PC) of aerosol in Los Angeles (Craven et al., 2013), and similar methods could
possibly be applied to sets of spectra or atmospheric aerosol and gas retrievals. In-
sight could also come from examining empirical orthogonal functions (EOF) after
setting a fixed primary PC (PC1).

Chapter **??** ended with suggestions to model aerosol light extinction under different
humidities. There has already been past work that has examined aerosol hygroscop-
icity (Hersey et al., 2013) and aerosol optical properties during CalNex (Thompson
et al., 2012). These past studies could inform model work. Results may be used
in conjunction with PC analysis to partition how much AOD is from atmospheric
water, how much is from directly emitted particles, and how much is attributable to
other sources and processes (e.g. aging).

BIBLIOGRAPHY

Affek, H. P., Xu, X., and Eiler, J. M.: Seasonal and diurnal variations of 13C18O16O in air: Initial observations from Pasadena, CA, Geochimica et Cosmochimica Acta, 71, 5033–5043, doi:10.1016/j.gca.2007.08.014, 2007.

Baker, D. F., Law, R. M., Gurney, K. R., Rayner, P., Peylin, P., Denning, A. S., Bousquet, P., Bruhwiler, L., Chen, Y. H., Ciais, P., Fung, I. Y., Heimann, M., John, J., Maki, T., Maksyutov, S., Masarie, K., Prather, M., Pak, B., Taguchi, S., and Zhu, Z.: TransCom 3 inversion intercomparison: Impact of transport model errors on the interannual variability of regional CO2 fluxes, 1988-2003, Global Biogeochemical Cycles, 20, 1988–2003, doi:10.1029/2004GB002439, 2006.

Bennett, J. M. and Ashley, E. J.: Infrared Reflectance and Emittance of Silver and Gold Evaporated in Ultrahigh Vacuum, Applied Optics, 4, 221, doi:10.1364/AO.4.000221, 1965.

Brioude, J., Angevine, W. M., Ahmadov, R., Kim, S. W., Evan, S., McKeen, S. A., Hsie, E. Y., Frost, G. J., Neuman, J. A., Pollack, I. B., Peischl, J., Ryerson, T. B., Holloway, J., Brown, S. S., Nowak, J. B., Roberts, J. M., Wofsy, S. C., Santoni, G. W., Oda, T., and Trainer, M.: Top-down estimate of surface flux in the Los Angeles Basin using a mesoscale inverse modeling technique: Assessing anthropogenic emissions of CO, NOx and CO2 and their impacts, Atmospheric Chemistry and Physics, 13, 3661–3677, doi:10.5194/acp-13-3661-2013, 2013.

Chen, J., Samra, J., Gottlieb, E., Budney, J., Daube, C., Daube, B., Hase, F., Gerbig, C., Chance, K., and Wofsy, S.: Boston Column Network: Compact Solar-Tracking Spectrometers and Differential Column Measurements, in: American Geophysical Union Fall Meeting, San Francisco, California, December 15–19, doi:10.13140/RG.2.1.2284.1361, 2014.

Chen, J., Viatte, C., Hedelius, J., Jones, T., Parker, H., Franklin, J., Gottlieb, E., Wennberg, P., Dubey, M., and Wofsy, S.: Differential Column Measurements Using Compact Solar-Tracking Spectrometers, Atmospheric Chemistry and Physics, 16, 8479–8498, doi:10.5194/acp-2015-1058, 2016.

Collins, M., Knutti, R., Arblaster, J., Dufresne, J.-L., Fichefet, T., Friedlingstein, P., Gao, X., Gutowski, W. J., Johns, T., Krinner, G., Shongwe, M.,

Tebaldi, C., Weaver, A. J., and Wehner, M.: Long-term Climate Change: Projections, Commitments and Irreversibility, Climate Change 2013: The Physical Science Basis. Contribution of Working Group I to the Fifth Assessment Report of the Intergovernmental Panel on Climate Change, pp. 1029–1136, doi:10.1017/CBO9781107415324.024, 2013.

Connor, B. J., Boesch, H., Toon, G., Sen, B., Miller, C., and Crisp, D.: Orbiting Carbon Observatory: Inverse method and prospective error analysis, Journal of Geophysical Research: Atmospheres, 113, D05 305, doi:10.1029/2006JD008336, 2008.

Craven, J. S., Metcalf, A. R., Bahreini, R., Middlebrook, A., Hayes, P. L., Duong, H. T., Sorooshian, A., Jimenez, J. L., Flagan, R. C., and Seinfeld, J. H.: Los Angeles Basin airborne organic aerosol characterization during CalNex, Journal of Geophysical Research Atmospheres, 118, 11 453–11 467, doi:10.1002/jgrd.50853, 2013.

Crisp, D., Fisher, B. M., O'Dell, C., Frankenberg, C., Basilio, R., Bösch, H., Brown, L. R., Castano, R., Connor, B., Deutscher, N. M., Eldering, A., Griffith, D., Gunson, M., Kuze, A., Mandrake, L., McDuffie, J., Messerschmidt, J., Miller, C. E., Morino, I., Natraj, V., Notholt, J., O'Brien, D. M., Oyafuso, F., Polonsky, I., Robinson, J., Salawitch, R., Sherlock, V., Smyth, M., Suto, H., Taylor, T. E., Thompson, D. R., Wennberg, P. O., Wunch, D., and Yung, Y. L.: The ACOS CO 2 retrieval algorithm - Part II: Global XCO2 data characterization, Atmospheric Measurement Techniques, 5, 687–707, doi:10.5194/amt-5-687-2012, 2012.

Deutscher, N. M., Griffith, D. W. T., Bryant, G. W., Wennberg, P. O., Toon, G. C., Washenfelder, R. A., Keppel-Aleks, G., Wunch, D., Yavin, Y., Allen, N. T., Blavier, J. F., Jiménez, R., Daube, B. C., Bright, A. V., Matross, D. M., Wofsy, S. C., and Park, S.: Total column CO2 measurements at Darwin, Australia - Site description and calibration against in situ aircraft profiles, Atmospheric Measurement Techniques, 3, 947–958, doi:10.5194/amt-3-947-2010, 2010.

Didan, K.: MOD13C2 MODIS/Terra Vegetation Indices Monthly L3 Global 0.05 Deg CMG V006, NASA EOSDIS Land Processes DAAC, doi:10.5067/MODIS/MOD13C2.006, 2015.

Dils, B., Buchwitz, M., Reuter, M., Schneising, O., Boesch, H., Parker, R., Guerlet, S., Aben, I., Blumenstock, T., Burrows, J. P., Butz, A., Deutscher, N. M., Franken-

berg, C., Hase, F., Hasekamp, O. P., Heymann, J., De Mazière, M., Notholt, J., Sussmann, R., Warneke, T., Griffith, D., Sherlock, V., and Wunch, D.: The greenhouse gas climate change initiative (GHG-CCI): Comparative validation of GHG-CCI SCIAMACHY/ENVISAT and TANSO-FTS/GOSAT CO2 and CH4 retrieval algorithm products with measurements from the TCCON, Atmospheric Measurement Techniques, 7, 1723–1744, doi:10.5194/amt-7-1723-2014, 2014.

Djuricin, S., Pataki, D. E., and Xu, X.: A comparison of tracer methods for quantifying CO2 sources in an urban region, Journal of Geophysical Research: Atmospheres, 115, 1–13, doi:10.1029/2009JD012236, 2010.

Dohe, S., Sherlock, V., Hase, F., Gisi, M., Robinson, J., Sepúlveda, E., Schneider, M., and Blumenstock, T.: A method to correct sampling ghosts in historic near-infrared Fourier transform spectrometer (FTS) measurements, Atmospheric Measurement Techniques, 6, 1981–1992, doi:10.5194/amt-6-1981-2013, URL `http://www.atmos-meas-tech.net/6/1981/2013/`, 2013.

Duren, R. M. and Miller, C. E.: Measuring the carbon emissions of megacities, Nature Climate Change, 2, 560–562, doi:10.1038/nclimate1629, URL `http://www.nature.com/doifinder/10.1038/nclimate1629`, 2012.

Eldering, A., O'Dell, C. W., Wennberg, P. O., Crisp, D., Gunson, M. R., Viatte, C., Avis, C., Braverman, A., Castano, R., Chang, A., Chapsky, L., Cheng, C., Connor, B., Dang, L., Doran, G., Fisher, B., Frankenberg, C., Fu, D., Granat, R., Hobbs, J., Lee, R. A. M., Mandrake, L., McDuffie, J., Miller, C. E., Myers, V., Natraj, V., O&apos;Brien, D., Osterman, G. B., Oyafuso, F., Payne, V. H., Pollock, H. R., Polonsky, I., Roehl, C. M., Rosenberg, R., Schwandner, F., Smyth, M., Tang, V., Taylor, T. E., To, C., Wunch, D., and Yoshimizu, J.: The Orbiting Carbon Observatory-2: first 18 months of science data products, Atmospheric Measurement Techniques, 10, 549–563, doi:10.5194/amt-10-549-2017, URL `http://www.atmos-meas-tech-discuss.net/amt-2016-247/` `http://www.atmos-meas-tech.net/10/549/2017/`, 2017.

Etheridge, D., Steele, L., Langenfelds, R., Rancey, R., Barnola, J.-M., and Morgan, V.: Natural and anthropogenic changes in atmospheric CO2 over the last 1000 years from air in Antarctic ice and firn, Journal of Geophysical Research, 101, 4115–4128, doi:10.1029/95jd03410, URL `http://onlinelibrary.wiley.com/doi/10.1029/95JD03410/full`, 1996.

Feist, D. G., Arnold, S. G., Hase, F., and Ponge, D.: Rugged optical mirrors for Fourier transform spectrometers operated in harsh environments, Atmospheric Measurement Techniques, 9, 2381–2391, doi:10.5194/amt-9-2381-2016, URL `http://www.atmos-meas-tech.net/9/2381/2016/`, 2016.

Feldman, D. R., Collins, W. D., Gero, P. J., Torn, M. S., Mlawer, E. J., and Shippert, T. R.: Observational determination of surface radiative forcing by CO_2 from 2000 to 2010, Nature, 519, 339–343, doi:10.1038/nature14240, URL `http://www.nature.com/doifinder/10.1038/nature14240`, 2015.

Feng, S., Lauvaux, T., Newman, S., Rao, P., Ahmadov, R., Deng, A., Díaz-Isaac, L. I., Duren, R. M., Fischer, M. L., Gerbig, C., Gurney, K. R., Huang, J., Jeong, S., Li, Z., Miller, C. E., O'Keeffe, D., Patarasuk, R., Sander, S. P., Song, Y., Wong, K. W., and Yung, Y. L.: LA Megacity: a High-Resolution Land-Atmosphere Modelling System for Urban CO_2 Emissions, Atmospheric Chemistry and Physics, 16, 9019–9045, doi:10.5194/acp-2016-143, URL `http://www.atmos-chem-phys-discuss.net/acp-2016-143/`, 2016.

Frey, M., Hase, F., Blumenstock, T., Groß, J., Kiel, M., Mengistu Tsidu, G., Schäfer, K., Sha, M. K., and Orphal, J.: Calibration and instrumental line shape characterization of a set of portable FTIR spectrometers for detecting greenhouse gas emissions, Atmospheric Measurement Techniques, 8, 3047–3057, doi:10.5194/amt-8-3047-2015, URL `http://www.atmos-meas-tech.net/8/3047/2015/`, 2015.

Geibel, M. C., Messerschmidt, J., Gerbig, C., Blumenstock, T., Chen, H., Hase, F., Kolle, O., Lavric, J. V., Notholt, J., Palm, M., Rettinger, M., Schmidt, M., Sussmann, R., Warneke, T., and Feist, D. G.: Calibration of column-averaged CH_4 over European TCCON FTS sites with airborne in-situ measurements, Atmospheric Chemistry and Physics, 12, 8763–8775, doi:10.5194/acp-12-8763-2012, 2012.

Gisi, M.: EM27/SUN, in: Annual Joint NDACC-IRWG & TCCON Meeting, Bad Sulza, Germany, May 12–14, URL `http://www.acom.ucar.edu/irwg/IRWG_2014_presentations/Wednesday_PM/Gisi_Bruker_EN27.pdf`, 2014.

Gisi, M., Hase, F., Dohe, S., Blumenstock, T., Simon, A., and Keens, A.: XCO2-measurements with a tabletop FTS using solar absorption spectroscopy, Atmo-

spheric Measurement Techniques, 5, 2969–2980, doi:10.5194/amt-5-2969-2012, URL http://www.atmos-meas-tech.net/5/2969/2012/, 2012.

Griffith, D. and Macatangay, R.: Xgas sensitivity to ILS, in: Annual Joint NDACC-IRWG & TCCON Meeting, Wollongong, Australia, 2–7 June, Wollongong, Australia, 2010.

Gurney, K. R., Razlivanow, I., Song, Y., Zhou, Y., Bedrich, B., and Abdul-massih, M.: Quantification of Fossil Fuel CO2 Emissions on the Building/Street Scale for a Large U.S. City, Environmental Science & Technology, 46, 12 194–12 202, doi:10.1021/es3011282, 2012.

Hale, G. E.: The Astrophysical Observatory of the California Institute of Technology, The Astrophysical Journal, 82, 111–139, doi:10.1086/143663, 1935.

Hanemann, M., de la Rue du Can, S., Wenzel, T., and Price, L.: Improving the Carbon Dioxide Emission Estimates from the Combustion of Fossil Fuels in California and Spatial Disaggregated Estimate of Energy-related Carbon Dioxide for California, URL http://www.arb.ca.gov/research/apr/past/05-310.pdf, 2008.

Hartmann, J.-M., Tran, H., and Toon, G.: Influence of line mixing on the retrievals of atmospheric CO2 from spectra in the 1.6 and 2.1 μm regions, Atmospheric Chemistry and Physics Discussions, 9, 7303–7312, doi:10.5194/acp-9-7303-2009, URL http://www.atmos-chem-phys-discuss.net/9/4873/2009/, 2009.

Hase, F.: Improved instrumental line shape monitoring for the ground-based, high-resolution FTIR spectrometers of the Network for the Detection of Atmospheric Composition Change, Atmospheric Measurement Techniques, 5, 603–610, doi:10.5194/amt-5-603-2012, 2012.

Hase, F., Blumenstock, T., and Paton-Walsh, C.: Analysis of the instrumental line shape of high-resolution fourier transform IR spectrometers with gas cell measurements and new retrieval software., Applied optics, 38, 3417–3422, doi:10.1364/AO.38.003417, 1999.

Hase, F., Hannigan, J., Coffey, M. T., Goldman, A., Hopfner, M., Jones, N. B., Risland, C. P., and Wood, S. W.: Intercomparison of retrieval codes used for the analysis of high-resolution, ground-based FTIR measurements, Journal of Quantitative

Spectroscopy and Radiative Transfer, 87, 25–52, doi:10.1016/j.jqsrt.2003.12.008, 2004.

Hase, F., Drouin, B. J., Roehl, C. M., Toon, G. C., Wennberg, P. O., Wunch, D., Blumenstock, T., Desmet, F., Feist, D. G., Heikkinen, P., De Mazière, M., Rettinger, M., Robinson, J., Schneider, M., Sherlock, V., Sussmann, R., Té, Y., Warneke, T., and Weinzierl, C.: Calibration of sealed HCl cells used for TCCON instrumental line shape monitoring, Atmospheric Measurement Techniques, 6, 3527–3537, doi:10.5194/amt-6-3527-2013, 2013.

Hase, F., Frey, M., Blumenstock, T., Groß, J., Kiel, M., Kohlhepp, R., Mengistu Tsidu, G., Schäfer, K., Sha, M. K., and Orphal, J.: Application of portable FTIR spectrometers for detecting greenhouse gas emissions of the major city Berlin, Atmospheric Measurement Techniques, 8, 3059–3068, doi:10.5194/amt-8-3059-2015, URL http://www.atmos-meas-tech.net/8/3059/2015/, 2015.

Hase, F., Frey, M., Kiel, M., Blumenstock, T., Harig, R., Keens, A., and Orphal, J.: Addition of a channel for XCO observations to a portable FTIR spectrometer for greenhouse gas measurements, Atmospheric Measurement Techniques, 9, 2303–2313, doi:10.5194/amt-9-2303-2016, URL http://www.atmos-meas-tech-discuss.net/amt-2015-403/ http://www.atmos-meas-tech.net/9/2303/2016/, 2016.

Hedelius, J. K., Viatte, C., Wunch, D., Roehl, C., Toon, G. C., Chen, J., Jones, T., Wofsy, S. C., Franklin, J. E., Parker, H., Dubey, M. K., and Wennberg, P. O.: Assessment of errors and biases in retrievals of XCO2, XCH4, XCO, and XN2O from a 0.5 cm-1 resolution solar viewing spectrometer, Atmospheric Measurement Techniques, 9, 3527–3546, doi:10.5194/amt-9-3527-2016, URL http://www.atmos-meas-tech.net/9/3527/2016/amt-9-3527-2016.html, 2016.

Hedelius, J. K., Parker, H., Wunch, D., Roehl, C. M., Viatte, C., Newman, S., Toon, G. C., Podolske, J. R., Hillyard, P. W., Iraci, L. T., Dubey, M. K., and Wennberg, P. O.: Intercomparability of XCO2 and XCH4 from the United States TCCON sites, Atmospheric Measurement Techniques, 10, 1481–1493, doi:10.5194/amt-10-1481-2017, URL http://www.atmos-meas-tech-discuss.net/amt-2016-279/http://www.atmos-meas-tech.net/10/1481/2017/, 2017.

Hersey, S. P., Craven, J. S., Metcalf, A. R., Lin, J., Lathem, T., Suski, K. J., Cahill, J. F., Duong, H. T., Sorooshian, A., Jonsson, H. H., Shiraiwa, M., Zuend, A., Nenes, A., Prather, K. A., Flagan, R. C., and Seinfeld, J. H.: Composition and hygroscopicity of the Los Angeles Aerosol: CalNex, Journal of Geophysical Research: Atmospheres, 118, 3016–3036, doi:10.1002/jgrd.50307, URL `http://doi.wiley.com/10.1002/jgrd.50307`, 2013.

Hollander, M., A. Wolfe, D., and Chicken, E.: Nonparametric Statistical Methods, John Wiley & Sons, Inc., Hoboken, NJ, USA, third edn., doi:10.1002/9781119196037, URL `http://doi.wiley.com/10.1002/9781119196037`, 2014.

Hoornweg, D., Sugar, L., Freire, M., Anderson, C., Perinaz, B., Trejos, C. L., Dave, R., Lee, M., Joshi-Ghani, A., and Allaoua, Z.: Cities and Climate Change: An Urgent Agenda, World Bank, Washington DC, URL `http://siteresources.worldbank.org/INTUWM/Resources/340232-1205330656272/CitiesandClimateChange.pdf`, 2010.

Iraci, L., Podolske, J., Hillyard, P., Roehl, C., Wennberg, P. O., Blavier, J.-F., Landeros, J., Allen, N., Wunch, D., Zavaleta, J., Quigley, E., Osterman, G., Albertson, R., Dunwoody, K., and Boyden., H.: TCCON data from Armstrong Flight Research Center, Edwards, CA, USA, Release GGG2014R1., doi:10.14291/tccon.ggg2014.edwards01.R1/1255068, URL `http://dx.doi.org/10.14291/tccon.ggg2014.edwards01.R1/1255068`, 2014.

Irion, F. W., Gunson, M. R., Toon, G. C., Chang, A. Y., Eldering, A., Mahieu, E., Manney, G. L., Michelsen, H. a., Moyer, E. J., Newchurch, M. J., Osterman, G. B., Rinsland, C. P., Salawitch, R. J., Sen, B., Yung, Y. L., and Zander, R.: Atmospheric Trace Molecule Spectroscopy (ATMOS) Experiment Version 3 data retrievals., Applied optics, 41, 6968–6979, doi:10.1364/AO.41.006968, 2002.

Janardanan, R., Maksyutov, S., Oda, T., Saito, M., Kaiser, J. W., Ganshin, A., Stohl, A., Matsunaga, T., Yoshida, Y., and Yokota, T.: Comparing GOSAT observations of localized CO 2 enhancements by large emitters with inventory-based estimates, Geophysical Research Letters, 43, 3486–3493, doi:10.1002/2016GL067843, URL `http://doi.wiley.com/10.1002/2016GL067843`, 2016.

Kalnay, E., Kanamitsu, M., Kistler, R., Collins, W., Deaven, D., Gandin, L., Iredell, S., Saha, S., White, G., Woollen, J., Zhu, Y., Chelliah,

M., Ebisuzaki, W., Higgins, W., Janowiak, J., Mo, K., Ropelewski, C., Wang, J., Leetmaa, A., Reynolds, R., Jenne, R., and Joseph, D.: The NCEP/NCAR 40-Year Reanalysis Project, Bulletin of the American Meteorological Society, 77, 437–471, doi:http://dx.doi.org/10.1175/1520-0477(1996)077<0437:TNYRP>2.0.CO;2, URL `http://dx.doi.org/10.1175/1520-0477(1996)077<0437:TNYRP>2.0.CO;2`, 1996.

Keeling, C. D.: Rewards and Penalties of Monitoring the Earth, Annual Review of Energy and the Environment, 23, 25–82, doi:10.1146/annurev.energy.23.1.25, URL `http://www.annualreviews.org/doi/abs/10.1146/annurev.energy.23.1.25`, 1998.

Keppel-Aleks, G., Toon, G. C., Wennberg, P. O., and Deutscher, N. M.: Reducing the impact of source brightness fluctuations on spectra obtained by Fourier-transform spectrometry., Applied optics, 46, 4774–4779, doi:10.1364/AO.46.004774, URL `http://www.ncbi.nlm.nih.gov/pubmed/17609726`, 2007.

Kiel, M., Wunch, D., Wennberg, P. O., Toon, G. C., Hase, F., and Blumenstock, T.: Improved retrieval of gas abundances from near-infrared solar FTIR spectra measured at the Karlsruhe TCCON station, Atmospheric Measurement Techniques, 9, 669–682, doi:10.5194/amt-9-669-2016, 2016.

Kille, N., Baidar, S., Handley, P., Ortega, I., Sinreich, R., Cooper, O. R., Hase, F., Hannigan, J. W., Pfister, G., and Volkamer, R.: The CU mobile Solar Occultation Flux instrument: structure functions and emission rates of NH3, NO2 and C2H6, Atmospheric Measurement Techniques, 10, 373–392, doi:10.5194/amt-10-373-2017, URL `http://www.atmos-meas-tech.net/10/373/2017/`, 2017.

Klappenbach, F., Bertleff, M., Kostinek, J., Hase, F., Blumenstock, T., Agusti-Panareda, A., Razinger, M., and Butz, A.: Accurate mobile remote sensing of XCO2 and XCH4 latitudinal transects from aboard a research vessel, Atmospheric Measurement Techniques, 8, 5023–5038, doi:10.5194/amt-8-5023-2015, URL `http://www.atmos-meas-tech.net/8/5023/2015/`, 2015.

Kort, E. A., Frankenberg, C., Miller, C. E., and Oda, T.: Space-based observations of megacity carbon dioxide, Geophysical Research Letters, 39, 1–5, doi:10.1029/2012GL052738, 2012.

Kort, E. A., Angevine, W. M., Duren, R., and Miller, C. E.: Surface observations for monitoring urban fossil fuel CO2 emissions: Minimum site location requirements

for the Los Angeles megacity, Journal of Geophysical Research: Atmospheres, 118, 1–8, doi:10.1002/jgrd.50135, 2013.

Kulawik, S., Wunch, D., O'Dell, C., Frankenberg, C., Reuter, M., Oda, T., Chevallier, F., Sherlock, V., Buchwitz, M., Osterman, G., Miller, C. E., Wennberg, P. O., Griffith, D., Morino, I., Dubey, M. K., Deutscher, N. M., Notholt, J., Hase, F., Warneke, T., Sussmann, R., Robinson, J., Strong, K., Schneider, M., De Mazière, M., Shiomi, K., Feist, D. G., Iraci, L. T., and Wolf, J.: Consistent evaluation of ACOS-GOSAT, BESD-SCIAMACHY, CarbonTracker, and MACC through comparisons to TCCON, Atmospheric Measurement Techniques, 9, 683–709, doi:10.5194/amt-9-683-2016, URL `http://www.atmos-meas-tech-discuss.net/8/6217/2015/` `http://www.atmos-meas-tech.net/9/683/2016/`, 2016.

Kuze, A., Suto, H., Nakajima, M., and Hamazaki, T.: Thermal and near infrared sensor for carbon observation Fourier-transform spectrometer on the Greenhouse Gases Observing Satellite for greenhouse gases monitoring., Applied optics, 48, 6716–6733, doi:10.1364/AO.48.006716, 2009.

Kuze, A., Suto, H., Shiomi, K., Kawakami, S., Tanaka, M., Ueda, Y., Deguchi, A., Yoshida, J., Yamamoto, Y., Kataoka, F., Taylor, T. E., and Buijs, H.: Update on GOSAT TANSO-FTS performance, operations, and data products after more than six years in space, Atmospheric Measurement Techniques, 9, 2445–2461, doi:doi:10.5194/amt-9-2445-2016, URL `http://www.atmos-meas-tech.net/9/2445/2016/`, 2016.

Learner, R. C. M., Thorne, A. P., and Brault, J. W.: Ghosts and artifacts in Fourier-transform spectrometry, Applied Optics, 35, 2947–2954, doi:10.1364/AO.35.002947, 1996.

Lin, J. C. and Wen, D.: A method to quantitatively apportion pollutants at high spatial and temporal resolution: the Stochastic Lagrangian Apportionment Method (SLAM), Environmental science & technology, 49, 351–360, doi:10.1021/es505603v, 2015.

Lindenmaier, R., Dubey, M. K., Henderson, B. G., Butterfield, Z. T., Herman, J. R., Rahn, T., and Lee, S.-h.: Multiscale observations of CO2, 13CO2, and pollutants at Four Corners for emission verification and attribution., Proceedings

of the National Academy of Sciences of the United States of America, 111, 8386–8391, doi:10.1073/pnas.1321883111, URL http://www.pnas.org/content/111/23/8386.full, 2014.

Mandrake, L. and Doran, G.: Warn Levels: Ordering Data for Custom Filtration, in: 11th International Workshop on Greenhouse Gas Measurements from Space, Pasadena, California 16-18 June, URL https://drive.google.com/file/d/0BxA3HC2mAmDha1FfN2pfQ2JtcXc/view, 2015a.

Mandrake, L. and Doran, G.: DOGO Warn Levels: You've got them, Let's use them, in: OCO-2 Science Team Meeting, Pasadena, California, November, Pasadena, CA, URL http://ml.jpl.nasa.gov/papers/mandrake/mandrake%5C_2015%5C_WL.pdf, 2015b.

McKain, K., Wofsy, S. C., Nehrkorn, T., Eluszkiewicz, J., Ehleringer, J. R., and Stephens, B. B.: Assessment of ground-based atmospheric observations for verification of greenhouse gas emissions from an urban region, Proceedings of the National Academy of Sciences, 109, 8423–8428, doi:10.1073/pnas.1116645109, 2012.

McLean, N. M.: Straight line regression through data with correlated uncertainties in two or more dimensions, with an application to kinetic isotope fractionation, Geochimica et Cosmochimica Acta, 124, 237–249, doi:10.1016/j.gca.2013.08.035, URL http://linkinghub.elsevier.com/retrieve/pii/S0016703713004870, 2014.

Messerschmidt, J., Macatangay, R., Notholt, J., Petri, C., Warneke, T., and Weinzierl, C.: Side by side measurements of CO2 by ground-based Fourier transform spectrometry (FTS), Tellus, Series B: Chemical and Physical Meteorology, 62, 749–758, doi:10.1111/j.1600-0889.2010.00491.x, 2010.

Messerschmidt, J., Geibel, M. C., Blumenstock, T., Chen, H., Deutscher, N. M., Engel, A., Feist, D. G., Gerbig, C., Gisi, M., Hase, F., Katrynski, K., Kolle, O., Lavric, J. V., Notholt, J., Palm, M., Ramonet, M., Rettinger, M., Schmidt, M., Sussmann, R., Toon, G. C., Truong, F., Warneke, T., Wennberg, P. O., Wunch, D., and Xueref-Remy, I.: Calibration of TCCON column-averaged CO2: The first aircraft campaign over European TCCON sites, Atmospheric Chemistry and Physics, 11, 10 765–10 777, doi:10.5194/acp-11-10765-2011, 2011.

Myhre, G., Shindell, D., Bréon, F.-M., Collins, W., Fuglestvedt, J., Huang, J., Koch, D., Lamarque, J.-F., Lee, D., Mendoza, B., Nakajima, T., Robock, a., Stephens, G., Takemura, T., and Zhan, H.: 2013: Anthropogenic and Natural Radiative Forcing, Climate Change 2013: The Physical Science Basis. Contribution of Working Group I to the Fifth Assessment Report of the Intergovernmental Panel on Climate Change, pp. 659–740, doi:10.1017/ CBO9781107415324.018, 2013.

Newman, S., Jeong, S., Fischer, M. L., Xu, X., Haman, C. L., Lefer, B., Alvarez, S., Rappenglueck, B., Kort, E. A., Andrews, A. E., Peischl, J., Gurney, K. R., Miller, C. E., and Yung, Y. L.: Diurnal tracking of anthropogenic CO2 emissions in the Los Angeles basin megacity during spring 2010, Atmospheric Chemistry and Physics, 13, 4359–4372, doi:10.5194/acp-13-4359-2013, 2013.

Newman, S., Xu, X., Gurney, K. R., Hsu, Y. K., Li, K. F., Jiang, X., Keeling, R., Feng, S., O'Keefe, D., Patarasuk, R., Wong, K. W., Rao, P., Fischer, M. L., and Yung, Y. L.: Toward consistency between trends in bottom-up CO2 emissions and top-down atmospheric measurements in the Los Angeles megacity, Atmospheric Chemistry and Physics, 16, 3843–3863, doi:10.5194/acp-16-3843-2016, 2016.

Nguyen, H., Osterman, G., Wunch, D., O'Dell, C., Mandrake, L., Wennberg, P., Fisher, B., and Castano, R.: A method for colocating satellite XCO2 data to ground-based data and its application to ACOS-GOSAT and TCCON, Atmospheric Measurement Techniques, 7, 2631–2644, doi:10.5194/amt-7-2631-2014, URL http://www.atmos-meas-tech.net/7/2631/2014/, 2014.

Nielsen-Gammon, J. W., Powell, C. L., Mahoney, M. J., Angevine, W. M., Senff, C., White, A., Berkowitz, C., Doran, C., and Knupp, K.: Multisensor estimation of mixing heights over a coastal city, Journal of Applied Meteorology and Climatology, 47, 27–43, doi:10.1175/2007JAMC1503.1, 2008.

O'Dell, C. W., Connor, B., Bösch, H., O'Brien, D., Frankenberg, C., Castano, R., Christi, M., Crisp, D., Eldering, A., Fisher, B., Gunson, M., McDuffie, J., Miller, C. E., Natraj, V., Oyafuso, F., Polonsky, I., Smyth, M., Taylor, T., Toon, G. C., Wennberg, P. O., and Wunch, D.: The ACOS CO2 retrieval algorithm-Part 1: Description and validation against synthetic observations, Atmospheric Measurement Techniques, 5, 99–121, doi:10.5194/amt-5-99-2012, 2012.

Pachauri, R. K., Allen, M. R., Barros, V. R., Broome, J., Cramer, W., and Christ, R.: Climate Change 2014 Synthesis Report, URL `http://www.ipcc.ch/pdf/assessment-report/ar5/syr/SYR_AR5_FINAL_full.pdf`, 2014.

Parker, H. A., Hedelius, J., Viatte, C., Wunch, D., Wennberg, P. O., Chen, J., Wofsy, S., Jones, T., Franklin, J., Dubey, M. K., Roehl, C. M., Podolske, J. R., Hillyard, P. W., and Iraci, L. T.: Compact Solar Spectrometer Column CO2, and CH4 Observations: Performance Evaluation at Multiple North American TCCON Sites, in: American Geophysical Union Fall Meeting, San Francisco, California, 14-18 December, 2015.

Pavley, F. and Nunez, F.: California Assembly Bill No. 32-Global Warming Solutions Act of 2006, URL `http://www.arb.ca.gov/cc/docs/ab32text.pdf`, 2006.

Perry, S. G. and Snyder, W. H.: Laboratory simulations of the atmospheric mixed-layer in flow over complex topography, Physics of Fluids, 29, 020 702, doi:10.1063/1.4974505, URL `http://aip.scitation.org/doi/10.1063/1.4974505`, 2017.

Petri, C., Warneke, T., Jones, N., Ridder, T., Messerschmidt, J., Weinzierl, T., Geibel, M., and Notholt, J.: Remote sensing of CO2 and CH4 using solar absorption spectrometry with a low resolution spectrometer, Atmospheric Measurement Techniques, 5, 1627–1635, doi:10.5194/amt-5-1627-2012, 2012.

Pougatchev, N. S., Connor, B., and Rinsland, C. P.: Infrared measurements of the ozone vertical distribution above Kitt Peak, Journal of Geophysical Research, 100, 16 689–16 697, doi:10.1029/95JD01296, 1995.

Rodgers, C. D.: Inverse Methods for Atmospheric Sounding - Theory and Practice, vol. 2 of *Series on Atmospheric Oceanic and Planetary Physics*, World Scientific Publishing Co. Pte. Ltd., doi:10.1142/9789812813718, URL `http://ebooks.worldscinet.com/ISBN/9789812813718/9789812813718.html`, 2000.

Rodgers, C. D. and Connor, B. J.: Intercomparison of remote sounding instruments, Journal of Geophysical Research, 108, 4116, doi:10.1029/2002JD002299, URL `http://doi.wiley.com/10.1029/2002JD002299`, 2003.

Saad, K. M., Wunch, D., Toon, G. C., Bernath, P., Boone, C., Connor, B., Deutscher, N. M., Griffith, D. W. T., Kivi, R., Notholt, J., Roehl, C., Schneider, M., Sherlock, V., and Wennberg, P. O.: Derivation of tropospheric

methane from TCCON CH 4 and HF total column observations, Atmos. Meas. Tech, 7, 2907–2918, doi:10.5194/amt-7-2907-2014, URL `www.atmos-meas-tech.net/7/2907/2014/`, 2014.

Schneider, A., Friedl, M. A., and Potere, D.: A new map of global urban extent from MODIS satellite data, Environmental Research Letters, 4, 1–11, doi:10.1088/1748-9326/4/4/044003, URL `http://stacks.iop.org/1748-9326/4/i=4/a=044003?key=crossref.6bde1987a5db9cd29ac85e4c73503481`, 2009.

Seto, K. C. and Dhakal, S.: Human Settlements, Infrastructure, and Spatial Planning, Climate change 2014: Mitigation of climate change. Contribution of Working Group III to the Fifth Assessment Report of the Intergovernmental Panel on Climate Change, pp. 923–1000, doi:10.1017/CBO9781107415416.018, 2014.

Sha, M. K., De Mazière, M., Metzger, J.-M., Cammas, J.-P., Frey, M., Kiel, M., and Hase, F.: The use of the portable EM27/SUN FTIR spectrometer as a travel standard for the TCCON, in: Annual Joint NDACC-IRWG & TCCON Meeting, Jeju, South Korea, 1–2 June, Jeju, South Korea, 2016.

Shiomi, K., Kuze, A., Kawakami, S., Kataoka, F., Hedelius, J., Viatte, C., Wennberg, P., Wunch, D., Roehl, C., Leifer, I., Tanaka, T., Iraci, L., Bruegge, C., and Schwander, F.: GOSAT CO2 and CH4 validation activity with a portable FTS at Pasadena, Chino, and Railroad Valley, in: American Geophysical Union Fall Meeting, San Francisco, California, December 14–18, 2015.

Shultz, P. and Warner, T. T.: Characteristics of Summertime Circulations and Pollutant Ventilation in the Los Angeles Basin.pdf, Journal of Applied Meteorology, 21, 672–682, doi:10.1175/1520-0450(1982)021<0672:COSCAP>2.0.CO;2, 1981.

Thompson, A. and Chen, H.: Beamcon III, a linearity measurement instrument for optical detectors, Journal of Research of the National Institute of Standards and Technology, 99, 751–755, doi:10.6028/jres.099.067, 1994.

Thompson, J. E., Hayes, P. L., Jimenez, J. L., Adachi, K., Zhang, X., Liu, J., Weber, R. J., and Buseck, P. R.: Aerosol optical properties at Pasadena, CA during CalNex 2010, Atmospheric Environment, 55, 190–200, doi:10.1016/j.atmosenv.2012.03.011, URL `http://linkinghub.elsevier.com/retrieve/pii/S1352231012002439`, 2012.

Toon, G. C.: The JPL MkIV interferometer, Optics and Photonics News, 2, 19, doi:10.1364/OPN.2.10.000019, URL http://www.opticsinfobase.org/abstract.cfm?URI=OPN-2-10-19, 1991.

Toon, G. C., Blavier, J.-F., Wennberg, P. O., and Roehl, C.: ILS Modeling, in: Annual Joint NDACC-IRWG & TCCON Meeting, Jeju, South Korea, 1–2 June, Jeju, South Korea, 2016a.

Toon, G. C., Wunch, D., Wennberg, P. O., and Arnold, S.: Post-Facto Temperature Correction, in: Annual Joint NDACC-IRWG & TCCON Meeting, Jeju, South Korea, 1–2 June, Jeju, South Korea, 2016b.

United Nations: World Urbanization Prospects: The 2014 Revision, Highlights, United Nations, New York, doi:10.4054/DemRes.2005.12.9, 2014.

Velazco, V. A., Griffith, D. W. T., Deutscher, N. M., and Morino, I.: NIES-FTS Container Retrieval Report, in: TCCON Teleconference, 13 September, 2016.

Verhulst, K. R., Karion, A., Kim, J., Salameh, P. K., Keeling, R. F., Newman, S., Miller, J., Sloop, C., Pongetti, T., Rao, P., Wong, C., Hopkins, F. M., Yadav, V., Weiss, R. F., Duren, R., and Miller, C. E.: Carbon Dioxide and Methane Measurements from the Los Angeles Megacity Carbon Project: 1. Calibration, Urban Enhancements, and Uncertainty Estimates, Atmospheric Chemistry and Physics Discussions, pp. 1–61, doi:10.5194/acp-2016-850, URL http://www.atmos-chem-phys-discuss.net/acp-2016-850/, 2016.

Viatte, C., Lauvaux, T., Hedelius, J. K., Parker, H., Chen, J., Jones, T., Franklin, J. E., Deng, A. J., Gaudet, B., Verhulst, K., Duren, R., Wunch, D., Roehl, C., Dubey, M. K., Wofsy, S., and Wennberg, P. O.: Methane emissions from dairies in the Los Angeles Basin, Atmospheric Chemistry and Physics Discussions, pp. 1–47, doi:10.5194/acp-2016-281, URL http://www.atmos-chem-phys-discuss.net/acp-2016-281/, 2016.

Villaraigosa, A. R.: Green LA: An action plan to lead the nation in fighting global warming, 2007.

Ware, J., Kort, E. A., DeCola, P., and Duren, R.: Aerosol lidar observations of atmospheric mixing in Los Angeles: Climatology and implications for greenhouse gas observations, Journal of Geophysical Research: Atmospheres, 121, 9862–9878, doi:10.1002/2016JD024953, 2016.

Washenfelder, R. A., Toon, G. C., Blavier, J. F., Yang, Z., Allen, N. T., Wennberg, P. O., Vay, S. A., Matross, D. M., and Daube, B. C.: Carbon dioxide column abundances at the Wisconsin Tall Tower site, Journal of Geophysical Research: Atmospheres, 111, D22 305, doi:10.1029/2006JD007154, 2006.

Wehr, R., Munger, J. W., McManus, J. B., Nelson, D. D., Zahniser, M. S., Davidson, E. a., Wofsy, S. C., and Saleska, S. R.: Seasonality of temperate forest photosynthesis and daytime respiration, Nature, 534, 680–3, doi:10.1038/nature17966, URL http://www.ncbi.nlm.nih.gov/pubmed/27357794, 2016.

Wennberg, P. O., Roehl, C., Blavier, J.-F., Wunch, D., Landeros, J., and Allen, N.: TCCON data from Jet Propulsion Laboratory, Pasadena, California, USA, Release GGG2014R1., doi:10.14291/tccon.ggg2014.jpl02.R1/1330096, URL http://dx.doi.org/10.14291/tccon.ggg2014.jpl02.R1/1330096, 2014a.

Wennberg, P. O., Roehl, C., Wunch, D., Toon, G. C., Blavier, J.-F., Washenfelder, R., Keppel-Aleks, G., Allen, N., and Ayers., J.: TCCON data from Park Falls, Wisconsin, USA, Release GGG2014R0., doi:10.14291/tccon.ggg2014.parkfalls01.R0/1149161, URL http://dx.doi.org/10.14291/tccon.ggg2014.parkfalls01.R0/1149161, 2014b.

Wennberg, P. O., Wunch, D., Roehl, C., Blavier, J.-F., Toon, G. C., and Allen, N.: TCCON data from California Institute of Technology, Pasadena, California, USA, Release GGG2014R1., doi:10.14291/tccon.ggg2014.pasadena01.R1/1182415, URL http://dx.doi.org/10.14291/tccon.ggg2014.pasadena01.R1/1182415, 2014c.

Wennberg, P. O., Wunch, D., Roehl, C., Blavier, J.-F., Toon, G. C., Allen, N., Dowell, P., Teske, K., Martin, C., and Martin, J.: TCCON data from Lamont, Oklahoma, USA, Release GGG2014R1., doi:10.14291/tccon.ggg2014.lamont01.R1/1255070, URL http://dx.doi.org/10.14291/tccon.ggg2014.lamont01.R1/1255070, 2014d.

Worden, J., Doran, G., Kulawik, S., Eldering, A., Crisp, D., Frankenberg, C., O'Dell, C., and Bowman, K.: Evaluation And Attribution Of OCO-2 XCO2 Uncertainties, Atmospheric Measurement Techniques Discussions, pp. 1–28, doi:10.5194/amt-2016-175, URL http://www.atmos-meas-tech-discuss.net/amt-2016-175/, 2016.

Wunch, D., Taylor, J. R., Fu, D., Bernath, P., Drummond, J. R., Midwinter, C., and Walker, K. A.: Simultaneous ground-based observations of O3, HCl, N2O, and CH4 over Toronto, Canada by three Fourier transform spectrometers with different resolutions, Atmospheric Chemistry and Physics, 7, 1275–1292, doi:10.5194/acp-7-1275-2007, 2007.

Wunch, D., Wennberg, P. O., Toon, G. C., Keppel-Aleks, G., and Yavin, Y. G.: Emissions of greenhouse gases from a North American megacity, Geophysical Research Letters, 36, L15 810, doi:10.1029/2009GL039825, URL `http://doi.wiley.com/10.1029/2009GL039825`, 2009.

Wunch, D., Toon, G. C., Wennberg, P. O., Wofsy, S. C., Stephens, B. B., Fischer, M. L., Uchino, O., Abshire, J. B., Bernath, P., Biraud, S. C., Blavier, J.-F. L., Boone, C., Bowman, K. P., Browell, E. V., Campos, T., Connor, B. J., Daube, B. C., Deutscher, N. M., Diao, M., Elkins, J. W., Gerbig, C., Gottlieb, E., Griffith, D. W. T., Hurst, D. F., Jiménez, R., Keppel-Aleks, G., Kort, E. A., Macatangay, R., Machida, T., Matsueda, H., Moore, F., Morino, I., Park, S., Robinson, J., Roehl, C. M., Sawa, Y., Sherlock, V., Sweeney, C., Tanaka, T., and Zondlo, M. A.: Calibration of the Total Carbon Column Observing Network using aircraft profile data, Atmospheric Measurement Techniques, 3, 1351–1362, doi:10.5194/amt-3-1351-2010, URL `http://www.atmos-meas-tech.net/3/1351/2010/`, 2010.

Wunch, D., Toon, G. C., Blavier, J.-F. L., Washenfelder, R. A., Notholt, J., Connor, B. J., Griffith, D. W. T., Sherlock, V., and Wennberg, P. O.: The Total Carbon Column Observing Network, Philosophical Transactions of the Royal Society A, 369, 2087–2112, doi:10.1098/rsta.2010.0240, URL `http://www.ncbi.nlm.nih.gov/pubmed/21502178`, 2011a.

Wunch, D., Wennberg, P. O., Toon, G. C., Connor, B. J., Fisher, B., Osterman, G. B., Frankenberg, C., Mandrake, L., O'Dell, C., Ahonen, P., Biraud, S. C., Castano, R., Cressie, N., Crisp, D., Deutscher, N. M., Eldering, A., Fisher, M. L., Griffith, D. W. T., Gunson, M., Heikkinen, P., Keppel-Aleks, G., Kyrö, E., Lindenmaier, R., Macatangay, R., Mendonca, J., Messerschmidt, J., Miller, C. E., Morino, I., Notholt, J., Oyafuso, F. A., Rettinger, M., Robinson, J., Roehl, C. M., Salawitch, R. J., Sherlock, V., Strong, K., Sussmann, R., Tanaka, T., Thompson, D. R., Uchino, O., Warneke, T., and Wofsy, S. C.: A method for evaluating bias in global measurements of CO2 total columns from space, Atmospheric Chemistry

and Physics, 11, 12 317–12 337, doi:10.5194/acp-11-12317-2011, URL `http://www.atmos-chem-phys.net/11/12317/2011/`, 2011b.

Wunch, D., Toon, G. C., Sherlock, V., Deutscher, N. M., Liu, C., Feist, D. G., and Wennberg, P. O.: The Total Carbon Column Observing Network's GGG2014 Data Version, p. 43, doi:10.14291/tccon.ggg2014.documentation.R0/1221662, URL `http://dx.doi.org/10.14291/tccon.ggg2014.documentation.R0/1221662`, 2015.

Wunch, D., Toon, G. C., Hedelius, J., Vizenor, N., Roehl, C. M., Saad, K. M., Blavier, J.-F. L., Blake, D. R., and Wennberg, P. O.: Quantifying the loss of processed natural gas within California's South Coast Air Basin using long-term measurements of ethane and methane, Atmospheric Chemistry and Physics, 16, 14 091–14 105, doi:10.5194/acp-16-14091-2016, URL `http://www.atmos-chem-phys.net/16/14091/2016/`, 2016a.

Wunch, D., Wennberg, P. O., Osterman, G., Fisher, B., Naylor, B., Roehl, C. M., O'Dell, C., Mandrake, L., Viatte, C., Griffith, D. W., Deutscher, N. M., Velazco, V. A., Notholt, J., Warneke, T., Petri, C., De Maziere, M., Sha, M. K., Sussmann, R., Rettinger, M., Pollard, D., Robinson, J., Morino, I., Uchino, O., Hase, F., Blumenstock, T., Kiel, M., Feist, D. G., Arnold, S. G., Strong, K., Mendonca, J., Kivi, R., Heikkinen, P., Iraci, L., Podolske, J., Hillyard, P. W., Kawakami, S., Dubey, M. K., Parker, H. A., Sepulveda, E., Rodriguez, O. E. G., Te, Y., Jeseck, P., Gunson, M. R., Crisp, D., and Eldering, A.: Comparisons of the Orbiting Carbon Observatory-2 (OCO-2) XCO2 measurements with TCCON, Atmospheric Measurement Techniques Discussions, pp. 1–45, doi:10.5194/amt-2016-227, URL `http://www.atmos-meas-tech-discuss.net/amt-2016-227/`, 2016b.

Yang, Z., Washenfelder, R. a., Keppel-Aleks, G., Krakauer, N. Y., Randerson, J. T., Tans, P. P., Sweeney, C., and Wennberg, P. O.: New constraints on Northern Hemisphere growing season net flux, Geophysical Research Letters, 34, L12 807, doi:10.1029/2007GL029742, URL `http://www.agu.org/pubs/crossref/2007/2007GL029742.shtml`, 2007.